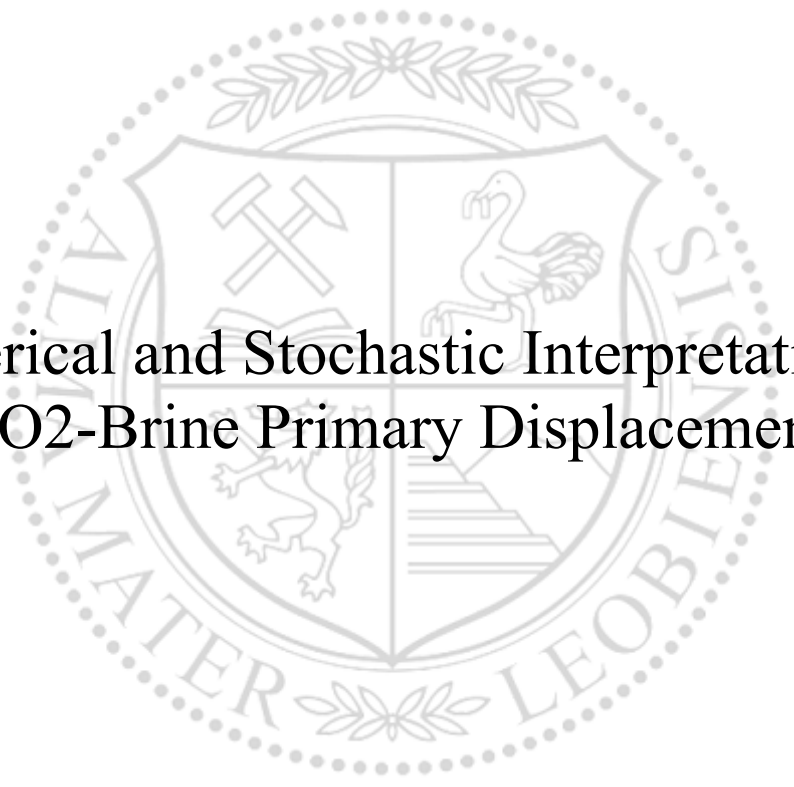Chair of Reservoir Engineering

Doctoral Thesis

Numerical and Stochastic Interpretation of CO2-Brine Primary Displacement

Dipl.-Ing. Omidreza Amrollahinasab Mahdiabad

December 2023

AFFIDAVIT

I declare on oath that I wrote this thesis independently, did not use other than the specified sources and aids, and did not otherwise use any unauthorized aids.

I declare that I have read, understood, and complied with the guidelines of the senate of the Montanuniversität Leoben for "Good Scientific Practice".

Furthermore, I declare that the electronic and printed version of the submitted thesis are identical, both, formally and with regard to content.

Date 21.12.2023

Signature Author
Omidreza Amrollahinasab Mahdiabad

Omidreza Amrollahinasab Mahdiabad
PhD Thesis 2023
Department Geoenergy

Numerical and Stochastic Interpretation of CO$_2$-Brine Primary Displacement

Supervisor: Univ.-Prof. Dipl.-Phys. Dr.rer.nat. Holger Ott
Mentor: Dr. Steffen Berg

Chair of Reservoir Engineering

Dedicated to all those who have supported me along this academic journey,

your belief in me has made all the difference.

Acknowledgments

Abstract

The burning of fossil fuels leads to an increasing concentration of carbon dioxide (CO2) in the atmosphere and consequently to global climate change. Despite the shift towards renewable energy, the dominant role of fossil fuels in global energy consumption necessitates solutions like Carbon Capture and Storage (CCS). CCS involves capturing CO_2 from large emission sources and storing it deep underground, where CO_2 displaces native fluids, such as brine. The efficiency of this displacement process is influenced by various geological and physical factors. Understanding and optimizing these factors is crucial. This work provides a comprehensive investigation of CO_2 brine displacement in porous rock, using both experimental and numerical methods. The experimental data are analyzed more rigorously than in previous studies, leading to a robust stochastic description of the two-phase flow in heterogeneous porous media. Additionally, numerical experiments were conducted to investigate the displacement stability, providing a new and unexpected scaling for viscous instabilities. Thus, this work provides a comprehensive and solid basis for risk analysis of CO_2 plume migration in CCS processes. The migration of the CO_2 plume and the efficiency of CO_2 displacement are primarily determined by multiphase flow parameters, namely relative permeability, and capillary pressure saturation functions, which are usually derived experimentally. In the frame of this work, the underlying numerical data analysis was developed based on the solid foundation of a combined stochastic interpretation of complementary experimental data sets. In the developed approach, data from different experimental methods (Special Core Analysis - SCAL) are analyzed simultaneously, and their uncertainty is rigorously determined by state-of-the-art stochastic methods. The resulting uncertainty intervals of the saturation functions refer to the intrinsic uncertainty of SCAL experiments, however, not to variations in rock properties. By interpreting and combining experiments derived from various methods and on various samples, the analyses provide a certain access to the heterogeneity of the rock formation.

To underscore the impact of rock heterogeneity on CO_2 migration, the approach was lifted to a larger length scale at which rock heterogeneity cannot be ignored anymore. Traditional SCAL methodologies typically do not account for heterogeneity, leading to discrepancies in measurements and field observations in terms of multiphase-flow saturation functions. Heterogeneity is vital for understanding the dynamics of plume migration and is explored in depth in this thesis. The thesis introduces an upscaling workflow that combines SCAL

interpretations with continuum-scale experiments, emphasizing the need for rigorous upscaling procedures for CO_2 storage in heterogeneous formations, such as carbonates.

Plume migration in heterogeneous formations is particularly affected when the mobility of the displacing fluid is higher than that of the displaced fluid. In this situation, viscous instabilities are to be expected, which can enhance fluid bypassing (sweep efficiency) in heterogeneous rock, depending on the characteristic length scale of the perturbation versus the finger width of the unstable front. This research challenges and extends existing theories on viscous fingering and its relation to interfacial tension and formation permeability. It further elucidates the findings from Darcy-scale numerical simulations that reveal finger wavelengths ranging from tens to a hundred meters under. Such a scale contrasts sharply with traditional predictions based on the Saffman & Taylor model, which significantly underpredicts the wavelengths. This insight is crucial for accurately predicting plume migration in CCS projects, as it accounts for the substantial deviation from expected behavior based on conventional models. The findings offer a novel perspective on the complexities of viscous-unstable displacement, challenging existing theories and providing a more accurate framework for understanding and predicting CO_2 plume migration in CCS scenarios.

This thesis substantially advances our understanding of CO_2 plume migration, addressing critical aspects of CO_2-brine displacement, uncertainties in ideal homogeneous and stabilized systems, and the effects of laboratory-scale heterogeneity and viscous instability. By rigorously investigating the scaling of finger wavelengths and their implications, this work reveals the significant impact of viscous-unstable displacement on plume migration, reshaping our approach to CCS modeling and implementation. The research's holistic examination, spanning from traditional measurements to advanced numerical methodologies, elevates the field's understanding of geological CO_2 storage, paving the way for more informed and effective carbon sequestration strategies and the associated risk assessment.

Zusammenfassung

Die Verbrennung fossiler Brennstoffe führt zu einer zunehmenden Konzentration von Kohlendioxid (CO2) in der Atmosphäre und ist damit ein entscheidender Faktor für den globalen Klimawandel. Trotz der Hinwendung zu erneuerbaren Energien erfordert die dominante Rolle fossiler Brennstoffe im weltweiten Energieverbrauch Lösungen wie Carbon Capture and Storage (CCS). CCS beinhaltet die Abscheidung von CO_2 aus großen Emissionsquellen und dessen Speicherung in Reservoirs tief unter der Erde, wo CO_2 natürliche Fluide wie Sole verdrängt. Die Effizienz dieses Verdrängungsprozesses wird von verschiedenen geologischen und physikalischen Faktoren beeinflusst, was es entscheidend macht, diese zu verstehen, zu quantifizieren und zu optimieren. Diese Arbeit bietet eine umfassende Untersuchung der CO2-Wasser-Verdrängung in porösem Gestein, wobei sowohl experimentelle als auch numerische Methoden zum Einsatz kommen. Die experimentellen Daten werden rigoroser analysiert als bisher dargestellt, was zu einer robusten stochastischen Beschreibung der Zweiphasenströmung in heterogenen porösen Medien führt. Darüber hinaus wurden numerische Experimente zur Untersuchung der Verdrängungsstabilität durchgeführt, die eine neue und unerwartete Skalierung für viskose Instabilitäten liefern. Die Arbeit bietet somit eine umfassende und solide Grundlage für eine Risikoanalyse der CO2-Migration für CCS Projekte. Die CO_2 Migration und die Effizienz der CO_2-Verdrängung werden hauptsächlich durch Mehrphasenströmungsparameter bestimmt, nämlich der relativen Fluidphasen Permeabilität und der Kapillardruck-Sättigungsfunktionen, die üblicherweise experimentell abgeleitet werden. Im Rahmen dieser Arbeit wurde die zugrundeliegende numerische Datenanalyse basierend auf der soliden Grundlage einer kombinierten stochastischen Interpretation komplementärer experimenteller Datensätze entwickelt. In dem entwickelten Ansatz werden Daten aus verschiedenen experimentellen Methoden (Spezialkernanalyse - SCAL) gleichzeitig analysiert, und ihre Unsicherheit wird rigoros durch state-of-the-art stochastische Methoden bestimmt. Die resultierenden Unsicherheitsintervalle dieser Sättigungsfunktionen beziehen sich auf die intrinsische Unsicherheit von SCAL-Experimenten, jedoch nicht auf Variationen in Gesteinseigenschaften. Durch die Interpretation und Kombination von Experimenten, die mit verschiedenen Methoden und an verschiedenen Proben durchgeführt wurden, bieten die Analysen einen gewissen Zugang zur Heterogenität der Gesteinsformation.

Um die Auswirkungen der Gesteinsheterogenität auf die CO_2-Migration zu unterstreichen, wurde der Ansatz auf eine größere Längenskala gehoben, auf der die Gesteinsheterogenität nicht mehr ignoriert werden kann. Traditionelle SCAL-Methodologien berücksichtigen in der Regel keine Heterogenität, was zu Diskrepanzen in Messungen und Feldbeobachtungen in Bezug auf Mehrphasenfluss-Sättigungsfunktionen führt. Heterogenität ist entscheidend für das Verständnis der Dynamik der CO_2 Migration und wird in dieser Dissertation ausführlich erforscht. Die Dissertation führt einen Upscaling-Workflow ein, der SCAL-Interpretationen mit großskaligen Experimenten kombiniert, und betont die Notwendigkeit rigoroser Upscaling-Verfahren zur Beschreibung der CO_2-Speicherung in heterogenen Formationen wie Karbonaten.

Die CO_2 Migration in heterogenen Formationen wird besonders beeinflusst, wenn die Mobilität der verdrängenden Flüssigkeit höher ist als die der verdrängten Flüssigkeit. In dieser Situation sind viskose Instabilitäten zu erwarten, die große Bereiche des Reservoirs umgehen können (Sweep-Effizienz) und somit die Speicherkapazität erheblich reduzieren. Dieser Effekt hängt von der charakteristischen Längenskala der Störung (Heterogenität) im Vergleich zur Fingerbreiten der instabilen Front ab. Diese Arbeit stellt bestehende Theorien über viskose Instabilitäten und deren Beziehung zur Grenzflächenspannung und Permeabilität der Formation in Frage und erweitert sie. Die Ergebnisse aus numerischen Simulationen zeigen Fingerwellenlängen im Bereich von Zehnern bis zu hundert Metern, im starken Kontrast zu traditionellen Vorhersagen basierend auf dem Saffman & Taylor-Modell, das die Wellenlängen erheblich unterschätzt. Diese Einsicht ist entscheidend für die genaue Vorhersage der Plume-Migration in CCS-Projekten, da sie die erhebliche Abweichung vom erwarteten Verhalten basierend auf konventionellen Modellen berücksichtigt. Die Erkenntnisse bieten eine neue Perspektive auf die Komplexitäten der viskosen-unstabilen Verdrängung und fordern bestehende Theorien heraus, indem sie einen genaueren Rahmen für das Verständnis und die Vorhersage der CO_2-Plume-Migration in CCS-Szenarien bieten.

Diese Dissertation erweitert unser Verständnis der CO_2-Plume-Migration erheblich, indem sie kritische Aspekte der CO_2-Sole-Verdrängung, Unsicherheiten in ideal homogenen und stabilisierten Systemen und die Auswirkungen von Labormaßstab-Heterogenität und viskoser Instabilität ausarbeitet. Durch die rigorose Untersuchung der Skalierung von Fingerwellenlängen und deren Implikationen enthüllt diese Arbeit den signifikanten Einfluss der viskosen-unstabilen Verdrängung auf die Plume-Migration und verändert unseren Ansatz zur CCS-Modellierung und -Implementierung. Die ganzheitliche Untersuchung, von traditionellen Messungen bis zu fortgeschrittenen numerischen Methodologien, erhöht das Verständnis des Feldes für die geologische CO_2-Speicherung und ebnet den Weg für effektivere Kohlenstoffabscheidungsstrategien und die damit verbundene Risikobewertung.

Table of Contents

Chapter 1

Introduction

Sustainable Energy and Impact of Fossil Fuels: The modern world's sustainable energy management and the need to mitigate environmental impacts, particularly from fossil fuels, is a pressing concern. Fossil fuels have been the cornerstone of the global energy system for over a century, shaping economic development and facilitating technological advancements. The widespread availability of coal, oil, and natural gas has underpinned considerable progress in human well-being and industrialization, contributing to the rapid urbanization and economic growth witnessed in the 20th and early 21st centuries (Smil, 2018). With their high energy content and relative ease of extraction and transportation, fossil fuels have become the linchpins of energy policy, reliably fueling the engines of growth across nations (BP, 2020).

The combustion of fossil fuels, however, releases significant amounts of carbon dioxide (CO_2) into the atmosphere, exacerbating the greenhouse effect and driving global climate change, a topic at the heart of international discourse. Despite their notable benefits, the burning of fossil fuels has a consequential downside – their environmental footprint. The combustion process releases a plethora of greenhouse gases, with carbon dioxide (CO_2) being the most significant in terms of volume and impact on global warming (EPA, 2021). As these emissions accumulate in the atmosphere, they trap heat and contribute to the greenhouse effect, leading to rising global temperatures and climate change. This trend has been corroborated by multiple scientific analyses and reports, including the Intergovernmental Panel on Climate Change (IPCC), which has reinforced the urgent need for drastic reductions in greenhouse gas emissions to limit the global temperature increase to 1.5 degrees Celsius above pre-industrial levels (Figure 1), thus mitigating the most severe consequences of climate change (Calvin et al., 2023; IPCC, 2018).
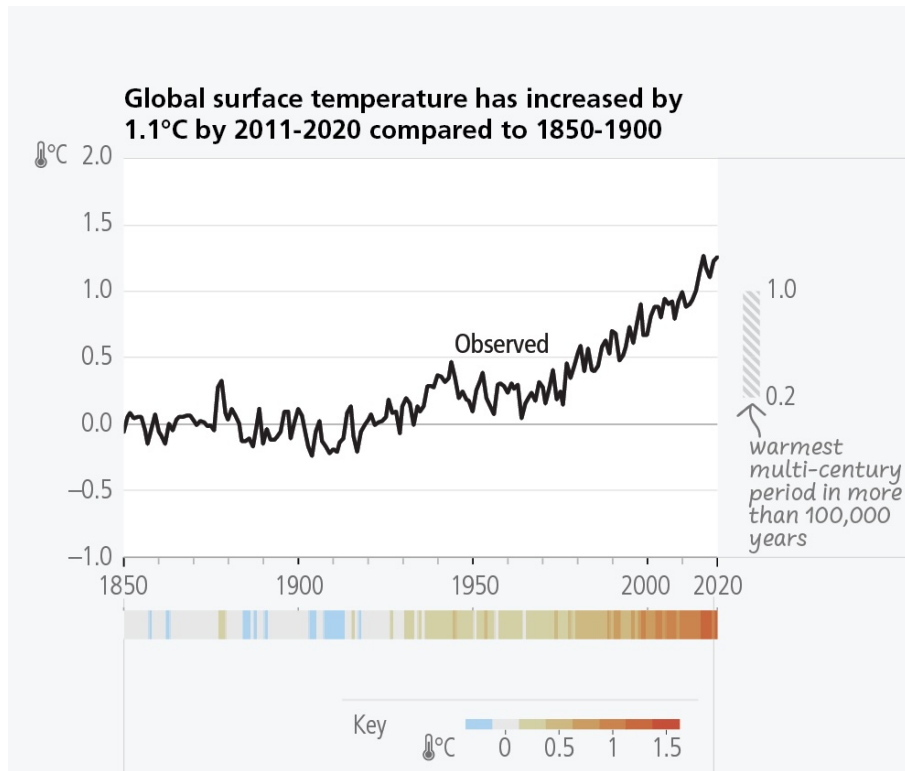
Figure 1: Global temperature change in recent years from IPCC (Calvin et al., 2023)

Challenges in Transitioning to Renewable Energy: Despite ongoing efforts to shift towards renewables, fossil fuels persistently dominate global energy consumption. International efforts, such as the Paris Agreement, have aimed at galvanizing global action towards a low-carbon economy. However, progress has been inconsistent and, in many regions, insufficient (UNFCCC, 2015). This is reflected in the global energy consumption patterns, where despite increasing investment in renewables, fossil fuels continue to supply the vast majority of the world's energy demand (IEA, 2021). Consequently, the global energy system remains heavily skewed towards non-renewable resources, which not only poses risks due to finite supplies but also propels the climate crisis.

Critics of the current energy paradigm argue for a more aggressive shift towards sustainable practices and emphasize the need for a broader adoption of renewable energy technologies (Jacobson et al., 2015). These technologies are becoming increasingly cost-effective and have shown promising scalability to meet a significant fraction of energy needs, outlining a roadmap to phase out fossil fuels (IRENA, 2021). Nevertheless, the transition is complex and inherently systemic, necessitating not only technological but also socio-political and economic transformation (Geels et al., 2015).

The lingering reliance on fossil fuels is influenced by various factors including technological advancements, existing infrastructure, financial commitments, and the overall inertia in restructuring the energy sector. This reliance manifests in significant geopolitical and market

dynamics, as energy security considerations often drive national policies and international relations (Yergin, 2012). Moreover, the built environment, including power plants, refineries, and transportation networks, represents sunk investments that cannot be easily or rapidly altered without both financial and societal costs (Davis et al., 2018). Moving away from an established energy system towards a low-carbon future involves multi-dimensional challenges, ranging from technological innovation to societal acceptance and legislative change (World Energy Council, 2019).

Future Energy Scenarios and Fossil Fuel Projections: Currently, fossil fuels, including coal, oil, and gas, account for over 80% of the world's primary energy supply (IEA, 2022). This dependence presents two significant concerns. First, fossil fuel reserves are depleting, with estimates predicting exhaustion within 139 years for coal, 57 years for oil, and 49 years for natural gas at the current consumption rates (Energy Institute, 2023). Furthermore, considering the growing rate of global energy consumption, these estimates may become even more pessimistic. Second, the combustion of these fossil fuels is primarily responsible for the surge in atmospheric CO_2 concentrations. Approximately 65% of current anthropogenic CO_2 emissions are attributed to fossil fuel use (IPCC, 2022; Smil, 2018). The consensus is that such emissions levels are unsustainable and that reducing greenhouse gas emissions is crucial for sustainable primary energy production.

Projections from energy industries and public organizations, like Shell's energy scenario (Figure 2), predict two main trends: a rise in overall energy demand until 2050 and a peak in fossil fuel demand around 2035, followed by a decline. However, even by 2050, fossil fuels will still constitute a significant portion (about 50%) of the energy mix. This persistence of fossil fuels in energy forecasts underscores the inertia in the energy market, influenced more by existing infrastructures and investments than by the pace of alternative energy technology development.

EJ/year
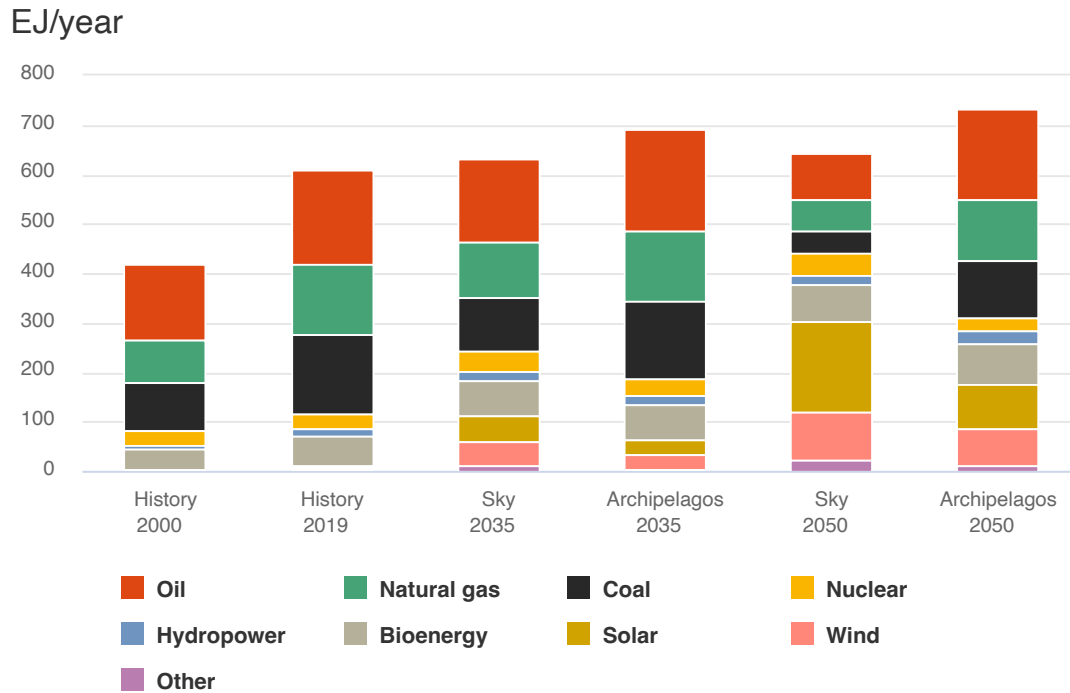
Figure 2: Primary energy trends to 2050 (Shell scenarios, 2023)

Mitigating Fossil Fuel Consumption with CCS as a Solution: Given the expected continued reliance on fossil fuels, the world must not only champion renewable energy but also mitigate the consequences of fossil fuel consumption. One strategy towards a sustainable energy future is reducing anthropogenic greenhouse-gas emissions. Solutions from the consumer side include energy conservation, and efficiency enhancement. On the production side, while renewable energies are gaining traction, the dominant role of fossil fuels necessitates solutions like Carbon Capture and Storage (CCS). Introduced in the 1990s, CCS was seen as a transitional technology that could be deployed faster and more affordably than renewables. Modern perspectives, however, view CCS as a technology that can be combined with biomass combustion to achieve negative-CO_2 pathways or used for producing hydrogen for low-carbon power generation. The merger of CCS and biomass combustion not only curtails emissions but can also actively reduce atmospheric CO_2 concentrations. Nevertheless, the effectiveness and scale of CCS and related technologies remain uncertain and present challenges.

Carbon Capture and Storage Overview: Carbon Capture and Storage (CCS) is a technology designed to reduce greenhouse gas emissions from industrial sources, thereby playing a pivotal role in global efforts to combat climate change (IPCC, 2005). CCS involves three major steps: capturing CO_2 produced by industrial processes and power generation, transporting the captured CO_2 to a suitable storage site, and securely storing the CO_2 underground in geological formations (Herzog, 2011; Holloway, 2005) (Figure 3).

Capture: The capture of CO_2 can be accomplished through various techniques such as pre-combustion capture, post-combustion capture, and oxy-fuel combustion, each with its unique set of technologies and suitability for different types of industrial plants (Bert Metz et al., 2005; Rochelle, 2009). Pre-combustion capture involves removing CO_2 before fuel combustion, often in gasification processes; post-combustion capture, the most widely studied, entails scrubbing CO_2 from flue gases after combustion; and oxy-fuel combustion burns fuel in pure oxygen, resulting in flue gases with high CO_2 concentrations, thereby simplifying capture (Boot-Handford et al., 2014; Davison, 2007).

Transport: Once captured, CO_2 is compressed into a liquid state to facilitate its transport via pipelines or ships to storage locations. The infrastructure for transport must ensure that the CO_2 is moved safely and efficiently, minimizing the risk of leaks and maintaining the integrity of the CO_2 stream (Figueroa et al., 2008).

Storage: The final step in the CCS chain is the storage of CO_2, usually in deep geological formations such as depleted oil and gas fields, deep saline aquifers, or unminable coal seams (Bachu, 2008; Dooley et al., 2009). The suitability of these storage sites is determined by their capacity to hold large volumes of CO_2 for extended periods, their ability to ensure that CO_2 does not leak back into the atmosphere, and their overall economic feasibility (Benson and Cole, 2008; ZER, 2011) (Figure 6).
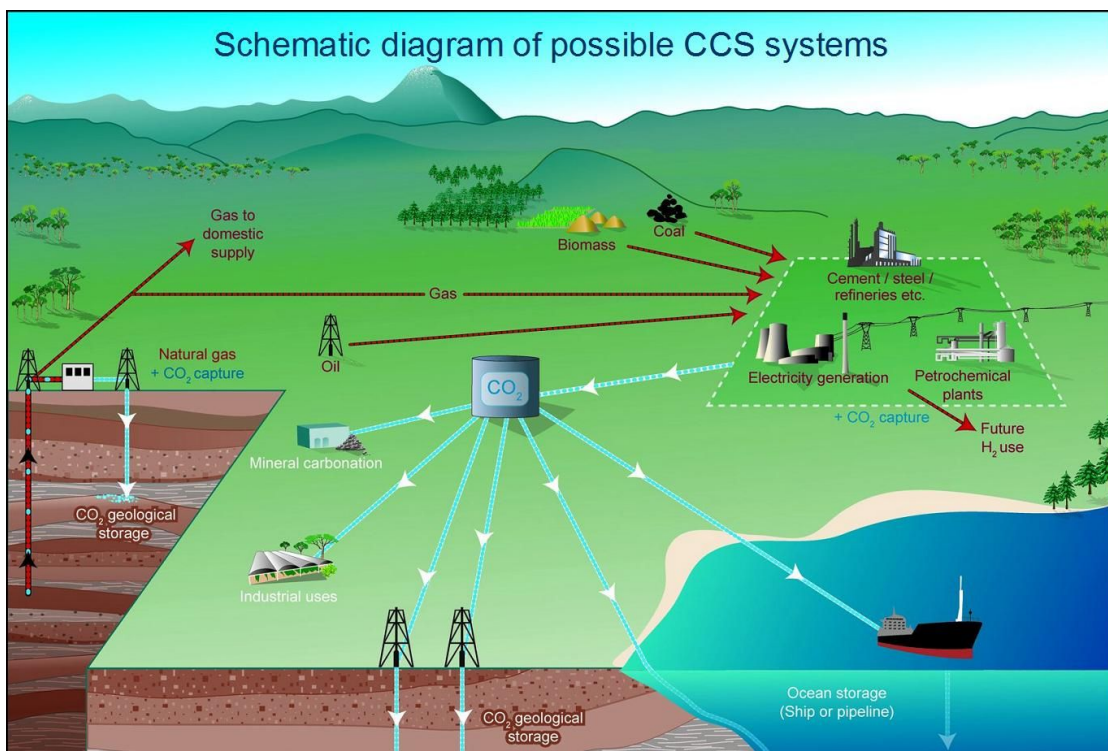

Figure 3: Major steps involved in carbon capture storage (CCS) (IPCC, 2005)

Chemical Properties and Environmental Role of CO₂: The unique chemical properties and phase behavior of carbon dioxide (CO_2) play a critical role in both its environmental impact and its potential for capture and storage. CO_2 is a linear, non-polar molecule, which contributes to its role as a potent greenhouse gas, effectively trapping heat in the Earth's atmosphere. Its phase behavior, particularly its ability to transition to a supercritical fluid under specific temperature and pressure conditions, is crucial in the context of Carbon Capture and Storage (CCS) technologies. In a supercritical state, CO_2 exhibits properties of both a gas and a liquid, allowing for more efficient transport and injection into geological formations (Span and Wagner, 1996). This phase transition is highly sensitive to temperature and pressure changes, influencing the design and operation of CCS systems (Figure 4).

Moreover, the interactions of CO_2 with other substances, such as water and various minerals found in geological formations, are essential for understanding its long-term storage behavior. CO_2 can react with water to form carbonic acid, a mild acid but one that can lead to the dissolution of certain minerals and potentially impact the integrity of a storage site (Kaszuba and Janecky, 2009). The solubility of CO_2 in brine, a common fluid in geological formations, is another critical factor as it influences the capacity and stability of CO_2 storage (Bachu and Adams, 2003). Understanding these chemical properties and phase behaviors is paramount for predicting the long-term fate of CO_2 in CCS operations and ensuring the environmental safety of this approach (Bert Metz et al., 2005).
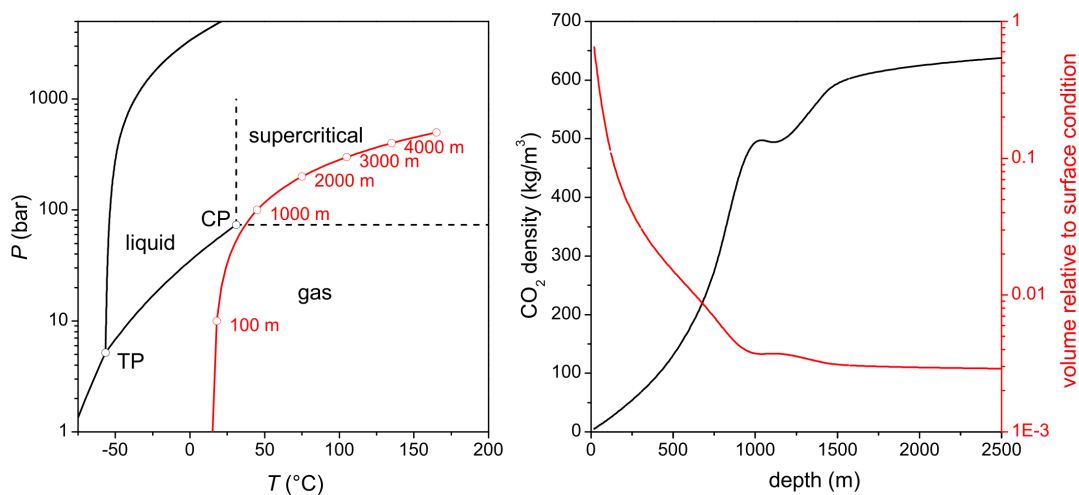
Figure 4: Left: Phase diagrams showing the relationship between pressure and temperature for CO_2. The red line shows the expected pressure and temperature based on a standard geothermal gradient and hydrostatic pressure in reservoirs. 'TP' marks the triple point, and 'CP' the critical point. Right: A chart depicting how CO_2 density varies with depth and how its volume changes compared to its volume at surface conditions (1 bar, 15°C) (Ott, 2015).

CO₂ Storage and Migration in Geological Formations: The storage phase of the CCS cycle is arguably the most complex, both in terms of scientific understanding and engineering execution. The multiphase flow of CO_2 through porous geological media, the long-term integrity of storage formations, and the risk of leakages are chief among the concerns (Bachu, 2008; Celia and Nordbotten, 2009) (Figure 5). Understanding the dynamics of CO_2 plume migration within various subsurface terrains requires sophisticated modeling and a deep knowledge of geomechanical behavior under CO_2 injection conditions (Juanes et al., 2010; Rutqvist, 2012). Monitoring and verification techniques must be advanced enough to detect even minor anomalies that could indicate storage issues, particularly over the time scales that CCS must operate to contribute effectively to climate change mitigation (Jenkins et al., 2018; Michael et al., 2010).
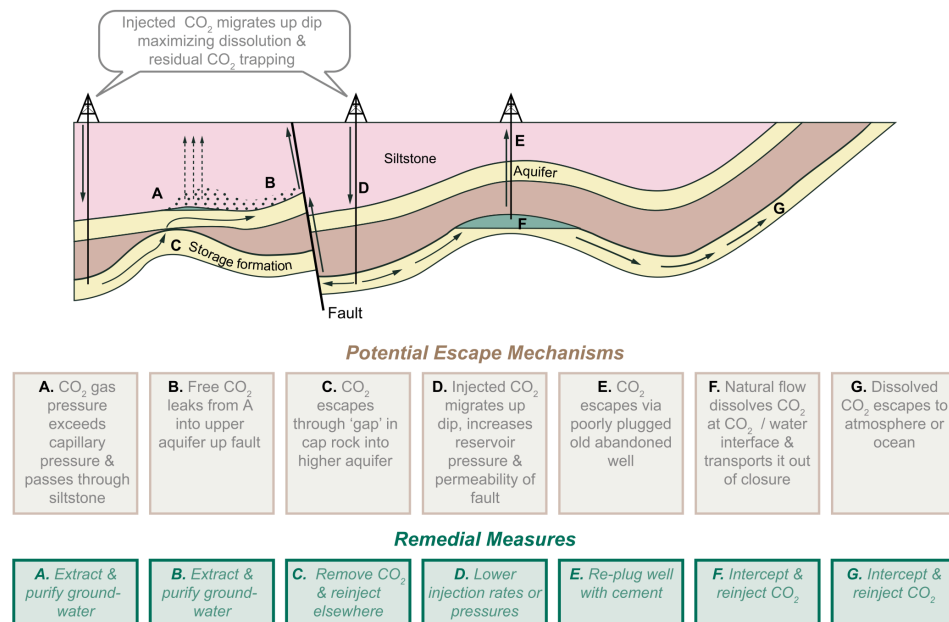
Figure 5: Potential leakage routes and remediation techniques for CO_2 injected into saline formations (Bert Metz et al., 2005)*.*

Upon injection into deep underground porous formations, CO_2 displaces the fluids initially present. Due to its lower density compared to the initial brine, CO_2 tends to migrate upwards, necessitating a sealing barrier to prevent its return to the surface. Various factors, including gravity and rock heterogeneity, can affect how effectively the CO_2 displaces other fluids. Over time, different trapping mechanisms, ranging from capillary to mineral trapping, come into play to immobilize the CO_2 (Figure 6). The primary focus of this thesis is to advance our understanding of CO_2-brine displacement dynamics in porous media and to enhance the accuracy of CO_2 plume migration predictions in CCS applications, recognizing its critical role in ensuring the safety and efficiency of CO_2 storage. Accurate prediction of plume migration

and the determination of its uncertainties is essential to ensure that it does not extend into areas with faults or insufficient characterization, thereby determining the site's overall storage capacity and safety.

Figure 6: Methods for storing CO₂ in deep underground geological formations (IPCC, 2005)

The prediction of CO_2 plume migration in subsurface reservoirs is a cornerstone of the CCS process. It is crucial for determining the amount of CO_2 that can be safely stored, as well as for evaluating potential r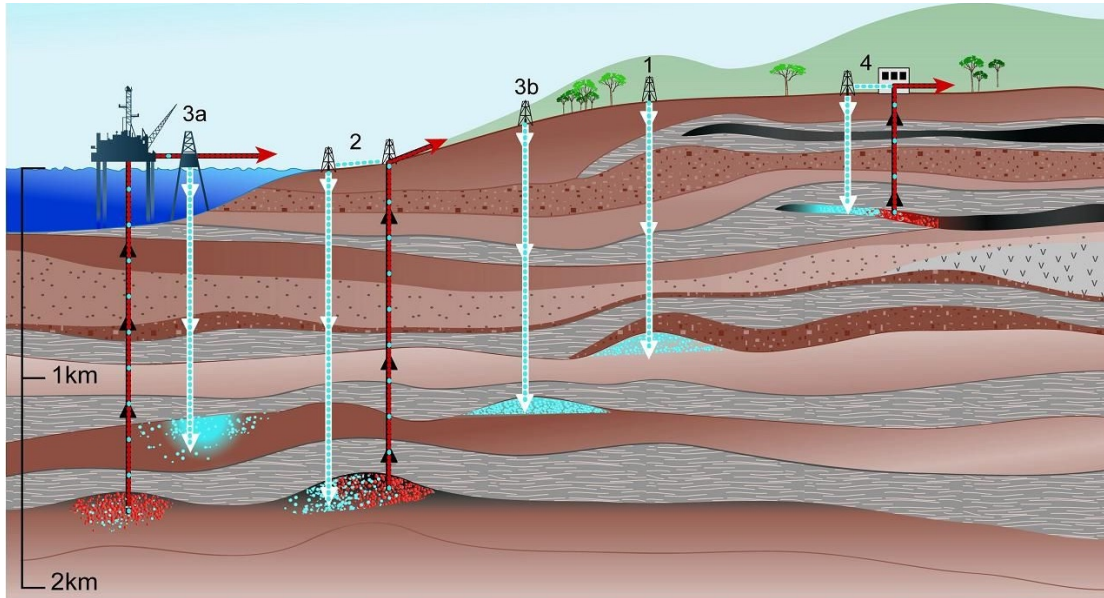isks associated with leakage. The literature has revealed that predicting CO_2 plume migration is riddled with uncertainties, both in terms of the physics involved and the geological and petrophysical properties, such as porosity, permeability, and rock composition, along with the physics of multiphase-flow dynamics and buoyancy-driven migration, of CO_2 in storage sites (Doughty and Oldenburg, 2020; Jackson and Krevor, 2020a).

Reservoirs are not uniform entities and underground CO_2 storage is intricate due to the diverse rock types and their spatial variations in geological reservoirs. Variations in porosity, permeability, and rock composition can cause CO_2 to move unpredictably. It is challenging to establish accurate geological models, especially in deep saline aquifers where fewer data points exist (Jackson and Krevor, 2020a; Krishnamurthy et al., 2022). Multiple processes govern CO_2 migration, including viscous flow, capillary trapping, and buoyancy-driven migration. Porosity, a measure of void space in the rock, dictates the volume of CO_2 that can be stored, while permeability, a measure of the ease with which fluids can flow through rock, influences the injection and migration capacity (Wildenschild and Sheppard, 2013).

Rock heterogeneity, capillary pressure, and relative permeability are also pivotal as they impact the distribution and movement of CO_2 within the storage reservoirs. Heterogeneity can lead to preferential flow paths or trapping zones, complicating the prediction of CO_2 plume evolution.

Capillary pressure, the pressure difference across the interface of two immiscible fluids in porous media, influences capillary trapping, a mechanism by which CO_2 is immobilized in the pore spaces due to interfacial tension and is a critical safeguard against leakage (Juanes and Blunt, 2006).

Furthermore, the wettability of the reservoir rock, which describes the tendency of a fluid to spread on or adhere to a solid surface, plays a role in dictating how CO_2 and brine will distribute inside the pore spaces, affecting both storage efficiency and security. Interactions with formation waters and minerals can modify rock permeability and porosity over time, potentially impacting fluid flow patterns, highlighting the importance of not treating these properties as static but rather as dynamic features that evolve with the CO_2 injection.

The interplay between these processes is intricate and varies with the specifics of the storage site (Juanes et al., 2006). Even with state-of-the-art monitoring techniques, tracking the exact movement of CO_2 in deep reservoirs remains a challenge. Subtle movements or small leaks can be hard to detect (Trevisan et al., 2017). Given these uncertainties, accurate prediction of CO_2 plume migration and especially the determination of its uncertainties becomes a complex endeavor, requiring sophisticated models, high-quality data, and iterative refinement based on real-world observations.

This Thesis: Central to this work is the exploration of two-phase flow dynamics in CO_2-brine systems, addressing three distinct yet interconnected contexts: (a) flow within homogeneous rock formations, providing a foundational understanding of the basic interaction principles; (b) flow within rock formations exhibiting textural heterogeneity, where variations in rock texture introduce complexities in fluid dynamics; and (c) flow within displacement-induced heterogeneous environments, where the movement of fluids itself alters the flow characteristics. By delving into these scenarios, this thesis aims to investigate the behaviors of two-phase flow, contributing significantly to the field of Geoenergy Engineering. This analysis is pivotal for advancing our understanding of CO_2 sequestration in various subsurface conditions, ultimately informing more efficient and reliable carbon capture and storage strategies.

It addresses the uncertainties surrounding CO_2 plume migration by combining traditional measurements with advanced methodologies. By enhancing our understanding of multiphase flow in porous media, we aim to shed light on the intricacies of CO_2-brine interactions and the factors that influence CO_2 migration patterns. This, in turn, will lead to more reliable predictions, ensuring safer and more efficient CO_2 storage.

Furthermore, methods are presented for calculation of numerous rock properties which are required for the prediction of CO_2 plume migration, especially those related to multiphase fluid dynamics, which are costly and time-consuming. It is pivotal to emphasize that in reservoir

simulations, the saturation functions - relative permeability ($k_r(S_w)$) and capillary pressure ($p_C(S_w)$) - play a more critical role than factors like porosity and permeability. These functions not only dictate fluid dynamics but also fundamentally determine the plume migration and storage capacity. While porosity, for example, has a linear effect on storage capacity, inaccuracies in these saturation functions can disproportionately reduce storage efficiency. Hence, this research focuses on paramount parameters for CO_2 storage. These functions influence fluid displacement and sweep efficiency, and with that also the injection pressure (Ahmed, 2018; Buckley and Leverett, 1942; Dake, 1983). These saturation functions are therefore essential for accurate prediction of CO_2 plume migration and storage safety.

This work is organized as the following: **Chapter 2** introduces the experimental and numerical methodologies employed in this thesis, supplemented by an extensive review of related literature in subsequent chapters that provides a contextual backdrop for each experimental and analytical approach presented. The experiments primarily focus on investigating fluid dynamics in carbonate rock systems, specifically Estaillades limestone, under various conditions to understand better the behavior of the wetting state. The chapter is divided into several key sections, each addressing different aspects of the experimental and analytical methodologies.

The experiments were conducted on different scales using two fluid pairs: decane-brine and CO_2-brine. SCAL (Special Core Analysis Laboratories) experiments were performed on small limestone samples with decane as the non-wetting phase, providing data for relative permeability and capillary pressure measurements. Larger and more heterogeneous limestone samples were used for primary drainage experiments, comparing decane-brine with CO_2-brine to study the influence of CO_2 mobility and wetting states.

In the SCAL experiments data from five rock samples, including porosity and permeability measures, were analyzed, providing insight into the rock's wetting state. Here brine and decane were used at ambient conditions, with specific attention to the viscosity of both fluids. The steady-state experiments involved oil and water injections, with measurements of differential pressure and saturation profiles. Centrifuge experiments further explored water saturation changes under increased centrifugal acceleration, using the Hassler-Brunner equations for data interpretation. This part is a reprint from (Amrollahinasab et al., 2022; Omidreza Amrollahinasab et al., 2023).

Large volume CO_2 experiments were conducted under elevated pressure and temperature, these experiments used larger limestone samples to study CO_2-brine displacement, comparing it with decane-brine displacement. This section also detailed the process of capturing and interpreting 3D saturation profiles using medical CT scanning. The process of deriving 3D porosity and saturation maps from CT scans is explained which involves using median and Gaussian-Blur-

3D filtering for image enhancement and applying difference imaging for 3D mapping. This part is a reprint from (Amrollahinasab et al., 2024a; Omidreza Amrollahinasab et al., 2023).

Numerical methods and implementation with the MRST (MATLAB Reservoir Simulation Toolbox) for simulating SCAL experiments are described, detailing the mathematical framework and solver strategies. It discusses the parametrization of saturation functions, steady-state and unsteady-state models, and the incorporation of boundary conditions. The chapter outlines the process of history matching in SCAL data interpretation, using MATLAB's fmincon function for optimization. It also addresses the uncertainty modeling using MCMC (Markov Chain Monte Carlo) methods and the ParaDRAM package for sampling and analyzing saturation function variations. This part is a reprint from (Amrollahinasab et al., 2024a, 2022; Omidreza Amrollahinasab et al., 2023, 2023) and is applied to (Burmester et al., 2023).

The numerical methodologies for incorporating heterogeneity in modeling saturation profiles, focusing on the variations in capillary pressure and permeability across different grid elements are also introduced in this section. The final section of the chapter deals with the stability analysis of CO_2-brine displacement, using a MATLAB-MRST-based simulator. It includes discussions on rock and fluid properties, determination of wavelength, and self-similarity in the context of viscous fingers in immiscible displacement. This part corresponds to a reprint from (Amrollahinasab et al., 2024b).

In **Chapter 3**, this thesis presents a sophisticated and novel approach to SCAL data interpretation, combining numerical modeling with advanced statistical methods to extract accurate uncertainties and gain deeper insights into multiphase fluid dynamics in porous media. Recognizing that multiphase flow in porous media is pivotal to Geoenergy Engineering, the research addresses the key uncertainties in reservoir engineering.

Traditional laboratory methods like core flooding have limitations, as they often can't capture the complexities of k_r and P_c in real reservoir conditions. The chapter investigates the steady-state method of measuring relative permeability, noting its inability to reach saturation endpoints and the influence of capillarity, which complicates the measurement of differential pressure. It also points out that classical analytical solutions and numerical descriptions often fail in accurately capturing the SCAL data. A more robust approach involves numerical data interpretation is suggested, which considers the full physical picture and combines various experimental data sets. This method, however, is prone to uncertainties due to non-uniqueness, instabilities, and experimental errors. The challenges in representing complex rock types like carbonates with standard parametrized models are noted and it is emphasized that single representations of Kr and Pc are not adequate for reliable flow predictions in reservoirs.

Through the development of a MATLAB-MRST-based simulator, the chapter emphasizes the significance of numerically interpreting data from different experimental techniques, assuming homogeneous rock samples. Furthermore, this chapter pioneers an uncertainty-driven approach to simultaneous simulation of SCAL experiments, ensuring more robust and accurate results. However, it also mentions that these advanced numerical interpretations and uncertainty modeling techniques are not yet common practice in SCAL due to proprietary simulation tools, which hinder progress in the field.

The limitations of such methods are shown by sample-to-sample variations of the interpretations on a complex carbonate rock. This chapter is a reprint of (Amrollahinasab et al., 2022; Omidreza Amrollahinasab et al., 2023), accompanied by Appendix A. The Appendix sheds light on the verification process for the simulations and Appendix B provides details of the user interface developed for the SCAL simulator.

Chapter 4 delves into the impact of rock heterogeneity on CO_2 migration. This heterogeneity complicates the measurement and interpretation of multiphase flow properties, influencing factors like capillary forces and saturation states, termed 'capillary heterogeneity'. The chapter discusses the limitations of conventional reservoir simulation workflows in representing small-scale heterogeneity impacts on multiphase flow properties like relative permeability and capillary pressure characteristics.

Understanding that traditional methods don't adequately account for this heterogeneity, the chapter presents a comprehensive upscaling workflow that effectively integrates state-of-the-art SCAL interpretations with continuum-scale experiments. The disparity between the scale of laboratory and special core analysis (SCAL) measurements and the larger scale of reservoir models are highlighted and the need for better understanding and characterizing capillary heterogeneity in complex rocks is addressed. A multiscale workflow from the centimeter to the meter scale is presented, combining laboratory techniques and upscaling schemes to systematically upscale multiphase flow for reservoir applications.

A case study on Estaillades limestone is referenced to illustrate the inadequacy of classical SCAL experiments in representing larger rock volumes. The chapter builds upon a previous study where a stochastic SCAL analysis workflow was developed and applied to experimental data on decane-brine primary drainage in Estaillades.

The present study aims to perform two key investigations: 1) A comparative analysis between full stochastic interpretations of SCAL data and larger-scale unsteady state (USS) core flood experiments to yield an upscaled relative permeability, and 2) Incorporating 3D porosity and permeability heterogeneity into USS experiments to determine the true relative permeability and understand the impact of heterogeneity.

By highlighting the disparity between traditional measurements and field observations, the chapter underscores the need for rigorous upscaling procedures, especially for CCS developments in carbonates. The chapter will analyze decane-brine and CO_2-brine unsteady-state experiments to study the effect of heterogeneity on relative permeability. The methodology involves progressively increasing the complexity of the fluid pairs and simulation domains to validate the approach and explore the limitations of current SCAL procedures, aiming to develop alternative methods and upscaling workflows. Appendix C complements this chapter by elaborating on the verification of the 3D simulations and the corresponding sensitivity analysis. This chapter is a reprint of (Amrollahinasab et al., 2024a; Omidreza Amrollahinasab et al., 2023).

Chapter 5 offers profound insights into the viscous-unstable displacement in CO_2 sequestration. This chapter focuses on the displacement of more viscous brine by less viscous CO_2 in subsurface formations, which can lead to the formation of viscous fingers. These fingers' wavelengths are crucial in determining storage capacity, plume migration, and the extent of capillary control in CCS.

The research challenges and extends existing theories on viscous fingering and its relation to interfacial tension and permeability. The challenged theory is the Saffman & Taylor model, which underpredicts the wavelength, and aligns more with the long-wavelength instability models of King & Dunayevsky and Yortsos & Hickernell.

It elucidates the findings from Darcy-scale numerical simulations that reveal finger wavelengths ranging from tens to a hundred meters under CCS conditions. The simulations consider factors such as rock permeability, fluid viscosity, and interfacial tension. The paper also explores the relationship between these factors and finger wavelength, finding linear relationships inconsistent with previous models.

This scale contrasts sharply with traditional predictions based on the Saffman & Taylor model, which significantly underpredict the wavelengths. The findings offer a new outlook on the complexities of viscous-unstable displacement, challenging existing theories and offering a more accurate framework to understand and predict CO_2 plume migration in CCS scenarios. It suggests a stronger influence of capillary forces on CO_2 plume migration, even at larger scales than previously thought. This has significant implications for modeling and predicting the behavior of CO_2 in subsurface environments. The insights guide the design and implementation of CCS projects, particularly in aspects of numerical modeling and field-scale uncertainty assessment. This chapter is a reprint of (Amrollahinasab et al., 2024b).

The research presented in this thesis not only contributes to the scientific understanding of CO_2-brine interactions but also has profound implications for the future of CCS technology and its

role in our collective pursuit of sustainable development as outlined by the UN Sustainable Development Goals (SDGs). Specifically, the methodologies and findings in this work support SDG 7 (Affordable and Clean Energy), SDG 9 (Industry, Innovation, and Infrastructure), SDG 12 (Responsible Consumption and Production), and SDG 13 (Climate Action) by enhancing our capabilities for effective carbon capture and storage (Ott, 2023; United Nations, 2023) (Figure 7). This could facilitate the continued yet sustainable use of fossil fuel resources while curbing emissions, promoting innovative clean energy technologies, and mitigating climate change impacts. By providing an overarching perspective on factors influencing CO_2 displacement, this thesis elevates our understanding of CCS processes. In turn, this will pave the way for optimized strategies that promote environmental stewardship and sustainable energy production.

Figure 7: Relevant UN Sustainable Development Goals (SDGs) supported by this thesis work. Specifically, the research enhances our capabilities for effective carbon capture and storage, contributing to: SDG 7 - Affordable and Clean Energy; SDG 9 - Industry, Innovation, and Infrastructure; SDG 12 - Responsible Consumption and Production; and SDG 13 - Climate Action (Ott, 2023; United Nations, 2023)*.*

Chapter 2

Materials and Methods

This chapter is a reprint of materials and methods from (Amrollahinasab et al., 2024a, 2024b, 2022; Omidreza Amrollahinasab et al., 2023, 2023).

2.1 Experimental Data Used in This Thesis

Experiments were performed on two different length scales and with two different fluid pairs, both representing water wet systems. SCAL experiments were performed on the smaller limestone samples using decane as a non-wetting phase, which is a typical choice for relative permeability and capillary pressure measurements (McPhee et al., 2015a). The primary drainage experiments on larger and heterogeneous samples of the same rock type, were performed with decane-brine reference fluids that are directly comparable to the SCAL experiments, and with the CO_2-brine fluid pair, the fluid system under investigation. By comparing decane-brine – the water wet reference – with results from CO_2-brine, statements on the influence of the high CO_2 mobility and the wetting state of the CO_2-brine-calcite system may be drawn.

2.1.1 SCAL Experiments

SCAL experiments were performed on Estaillades limestone, a rather complex, dual porosity carbonate rock type. The SS and centrifuge (CF) data were published in (Ott et al., 2015). The data set represents a primary drainage process on the original water-wet state of the rock.

Rock Samples: Experimental results from 5 rock samples taken from the same outcrop block of Estaillades limestone are discussed in this paper. The average porosity was determined to be $\phi = 0.28$, and the average permeability was determined to be $K = 164$ mD. The properties of the individual samples are summarized in Table 1. The block showed overall porosity variations of 10% and permeability variations of 28% (Ott et al., 2015).

Table 1: Rock samples, rock properties and experimental process.

Sample ID	Porosity (fraction)	Permeability (mD)	Measurement
1	0.293	142.3	Steady-state relative permeability; primary drainage
2	0.271	141.8	
3	0.283	204.1	Multispeed centrifuge capillary pressure; primary drainage
4	0.283	141.2	
5	0.274	189.8	

The rock type exhibited dual porosity with a pure calcite mineralogy (Ott et al., 2015). The samples were drilled and cut to dimensions of 3.75 cm diameter and 5 cm length for both types of experiments. Subsequently, the samples were cleaned, and $S_w = 1$ was established as the starting point for the drainage experiments.

Fluids: The SCAL experiments were performed at ambient pressure and temperature conditions (22°C) using brine and decane as wetting and nonwetting fluids. The brine contained 3 wt% NaCl and 5 wt% CsCl as X-ray doping agents. Under experimental conditions, the brine viscosity was measured to be 0.993 cP, and the viscosity of decane was measured to be 0.827 cP. Decane-brine is a classical water-wet reference case and often used in SCAL experiments (McPhee et al., 2015a).

Steady-State Experiments: Primary drainage SS relative permeability experiments were performed in vertical geometry by simultaneously injecting oil and water from top to bottom. The total injection rate was kept constant at 3 ml/min at different water fractional flow (f_w) steps.

The samples were initially saturated to $S_w = 1$ under vacuum conditions, followed by the first SS measurement at $f_w = 1$, referring to the first point on the primary drainage relative permeability. Furthermore, at $S_w = 1$, a multi-rate absolute permeability measurement was performed. f_w was then stepwise decreased by keeping the total flow rate constant. For each f_w step, the differential pressure and the 1D saturation profile along the core were measured after reaching steady state.

The differential pressure was measured in two ways: (a) from injection to production end over the total porous domain (the data shown here) and (b) locally, over a length of 2.5 cm around the center of the plug over which the saturation profile was essentially flat, excluding the capillary end effect. The local measurement allows us to analytically calculate the relative permeability point-by-point analytically using Darcy's law. The analytical solution serves as

an initial guess for numerical interpretation. The saturation was monitored by measuring the X-ray attenuation profile along the core, which is sensitive to different X-ray absorption coefficients of the fluids and hence to the saturation state.

Multispeed Centrifuge Experiments: Centrifuge experiments were performed in drainage mode, starting from $S_w = 1$, established in the same way as for the SS experiments. The samples were desaturated in multiple steps of increasing centrifugal acceleration adjusted by the angular frequency (McPhee et al., 2015a). During the experiment, the cumulative water production was recorded by an automatic stroboscopic read-out system. At the end of each experimental step no further water production was observed. From the cumulative water production, the average water saturation ($\overline{S_w}$) can be calculated. From $\overline{S_w}$ and the centrifugal acceleration, $p_C(S_w)$ can be estimated by the Hasser–Brunner equations (Hassler and Brunner, 1945), which serve as a starting point for the numerical data interpretation further below.

2.1.2 Large Volume CO$_2$ Experiments

The work was performed using experimental results published by (Ott et al., 2015). The experiments were performed on Estaillades (EST) limestone samples with a length of 15 cm and a diameter of 7.5 cm. The average rock porosity and permeability were experimentally derived to $\phi = 0.297$ and $K = 260$ mD, respectively.

The experiments were performed at elevated pressure and temperature conditions of 100 bar and 50°C, referring to approximately 1000 m reservoir depth at which the injected CO$_2$ is in the supercritical state (sc). To investigate the primary displacement process of brine by CO$_2$, the sample was first saturated to $S_w = 1$ and then flooded with scCO$_2$. A reference measurement was performed with decane as the injection phase; the decane-brine experiments serve as a reference and can directly be compared to the earlier SCAL interpretation since SCAL measurements were performed with the same fluid pair and on rock samples from the same block of the Estaillades outcrop. The flooding experiments were conducted under unsteady-state (USS) conditions, employing distinct constant injection rates for decane and CO$_2$. Specifically, a liquid injection rate of 0.25 ml/min was used for both decane and CO$_2$ at the pump. However, due to the characteristics of CO$_2$, where it changes from the liquid to the supercritical state on the way from the injection pump to the injection point, a volume correction is applied. As a result, the effective injection rate for CO$_2$ is calculated to be 0.44 ml/min. These flow rates correspond to capillary numbers of $Ca \sim 5 \times 10^{-8}$ for decane-brine and $Ca \sim 6 \times 10^{-9}$ for CO$_2$-brine. It can safely be expected that at both capillary numbers, the systems are far away from a capillary desaturation (well on the plateau of the capillary desaturation curve (Lake et al., 2014)) with the relative permeability being independent on the rate. This process allows a fair comparison and interpretation of the displacement processes

between the reference decane-brine and the CO_2-brine system. During the experiments, the pressure drop was measured, and the upfront 3D porosity profiles and in-situ 3D saturation profiles were taken by difference imaging in medical CT scanning. Brine-production curves were derived from CT saturation monitoring. 3D saturation profiles are shown in Figure 8 for the decane-brine displacement (top row) and the CO_2-brine displacement (bottom row) with the invading fluid in orange and the initial rock-fluid system as a semitransparent background. Further experimental details can be found in (Ott et al., 2015).
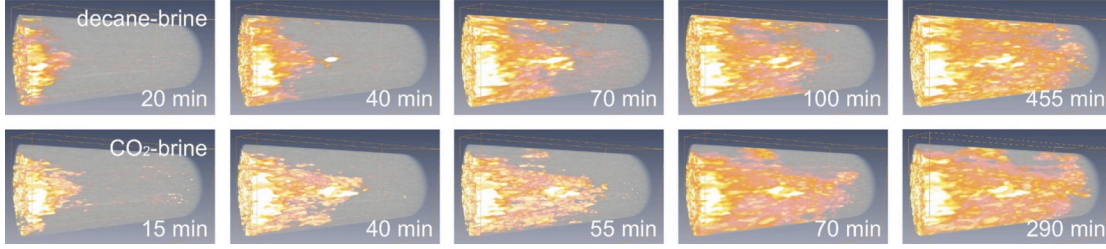
Figure 8: CT time sequences of the decane–brine (top) and CO_2–brine (bottom) experiments. The decane and CO_2 saturation distributions are illustrated in orange, and the initial rock-fluid system is displayed as a semitransparent background. Note that the threshold setting for the saturation is comparable but arbitrary to highlight heterogeneity in the saturation distribution.

2.1.3 Converting Medical-CT Data To 3D Saturation Maps

The 3D porosity and saturation maps were calculated from medical CT scans. The underlying grayscale images are given in absolute Hounsfield units (HU). The images were processed by median and Gaussian-Blur-3D filtering to reduce noise within the gathered scans and to enhance the contrast between the fluid phases.

The 3D porosity map was derived from difference imaging, i.e., taking the difference between the brine-saturated scan and the dry scan, as suggested by (Ott et al., 2015, 2012; Wellington and Vinegar, 1987). The 3D porosity profile was obtained by using a voxel-by-voxel approach:

$$\phi(\vec{x}) = \frac{HU_{brine}^{sat}(\vec{x}) - HU_{dry}(\vec{x})}{HU_{brine} - HU_{air}} = \alpha \cdot \left(HU_{brine}^{sat}(\vec{x}) - HU_{dry}(\vec{x}) \right), \qquad (1)$$

where $HU_{brine}^{sat}(\vec{x})$ refers to the scan of the fully brine-saturated sample, $HU_{dry}(\vec{x})$ to the dry scan, and HU_{brine} and HU_{air} correspond to the HU values of brine and air. To achieve the best calibration, the difference scan is scaled by the factor α to match the experimentally measured porosity of the plug.

Consequently, the 3D fluid distributions were calculated as a function of space and time from the dynamic CT profiles, $HU_{exp}(\vec{x}, t)$ by equation (2):

$$S_{CO_2}(\vec{x}, t) = \frac{HU_{brine}^{sat}(\vec{x}, t_0) - HU_{exp}(\vec{x}, t)}{HU_{brine}^{sat}(\vec{x}) - HU_{CO_2}^{sat}(\vec{x})}, \qquad (2)$$

where $HU_{brine}^{sat}(\vec{x}, t_0)$ and $HU_{exp}(\vec{x}, t)$ correspond to the initial scan at $S_w = 1$ and the current experimental time step, respectively, and $HU_{CO_2}^{sat}(\vec{x})$ is the scan of the fully CO_2-saturated sample. The two calibration scans in the denominator were conducted prior to the flooding experiment. The experimental and simulated 3D saturation profiles are shown in Figure 24 (a) to (f).

The original resolution of the CT images is 0.18×0.18×0.5 mm³. For computational efficiency, we binned 24×24×8 voxels, which means that each grid block measures approximately 4 mm cubed. To analyze the sensitivity of the simulation results to the choice of binning, simulations were performed with a lower binning of 12×12×4 for the decane-brine case. Since the effect of downscaling on the results was found to be minimal and since the simulation time increases exponentially with the number of grid blocks, a binning of 24×24×8 was used for the majority of the simulations.

2.2 Numerical Methods and Implementation

The forward modeling part is using the MRST to simulate the SS, unsteady state (USS), and CF experiments both in an imbibition and drainage mode. We use the term "forward modeling" for the case in which we have the full set of rock and fluid properties available, and we numerically simulate SCAL experiments. Forward modeling is especially useful to design experiments and for quality control purposes of, e.g., third-party data, or to judge the validity of analytical solutions as starting point for numerical analysis; typically, analytical solutions serve as starting points of the numerical workflow.

The initial step in our methodology begins with calculating the saturation functions from the experimental measurements using the corresponding analytical solutions, i.e., the Darcy equation for SS experiments and the Hassler–Brunner equations (Hassler and Brunner, 1945) for CF experiments. Then, we implement an objective function with which we search for the least mean square error between the experimental measurements of the SS (pressure and saturation profiles) and CF experiments (average water saturation) and the corresponding simulation predictions. These errors are summed up in a single total error to be able to match both experiments simultaneously. This objective function is then fed into the MATLAB optimization toolbox *fmincon* function.

The *fmincon* function attempts to optimize the saturation functions by minimizing the least mean square error defined in the objective function. The variation in the saturation functions is done in a point-by-point fashion to overcome the limitations of saturation function

parametrization functions, e.g., Corey (R. H. Brooks and A. T. Corey, 1964) and LET (Lomeland et al., 2005), which is further explained in the section on the parametrization of saturation functions. The results of the history matching simulation are then input into the *ParaDRAM* package to run the Monte Carlo simulations, sampling variations of the saturation tables in the vicinity of the history match results and quantify the uncertainty ranges around the history-matched solution.

As far as the convenience of use and the computational efficiency are concerned, MRST serves our purpose. Details, especially on the latter, are discussed further below.

Flow Equations and Solver: For the simulation of SCAL experiments, immiscible and incompressible fluid phases are assumed. Furthermore, fluid viscosities are assumed to be pressure independent and can be specified by the user. Under these conditions, two-phase flow can be described by the following governing equations: in the absence of source and sink terms, the material balance is expressed as:

$$\phi \, \partial_t(S_\alpha) + \nabla \cdot (\overrightarrow{v_\alpha}) = 0 \qquad \alpha = w, o \tag{3}$$

Here, ϕ is the porosity and S_α is the phase saturation—both dimensionless—and $\overrightarrow{v_a}$ is the Darcy phase velocity vector in units of m/s. Without the restriction to a specific combination of fluids we refer the two phases α to oil (o) and water (w) in the following. The Darcy velocity $\overrightarrow{v_a}$ is given by Darcy's law:

$$\overrightarrow{v_\alpha} = -\left(\frac{k_{r\alpha}}{\mu_\alpha}\right) K(\nabla p_\alpha - \rho_\alpha \vec{g}) \qquad \alpha = w, o \tag{4}$$

where $k_{r\alpha}$ are the dimensionless relative permeability saturation functions and μ_α are the phase viscosities in Pa · s. K is the absolute rock permeability in m^2, p_α are the phase pressures in Pa, and g is the gravitational constant in m/s^2. Furthermore, the phase saturations satisfy $S_w + S_o = 1$, and incompressible flow is further restricted to $\nabla \cdot (\overrightarrow{v_w} + \overrightarrow{v_o}) = 0$.

The solver is based on the MRST automatic differentiation (AD) toolbox, including differentiation and divergence operators, automatic differentiation to compute the Jacobians, object-oriented framework, and state functions from which we make use in the simulator. The details on how these operators are implemented in the MRST framework can be found in (Krogstad et al., 2015).

The simulation time and the desired time stepping are managed by using the MRST *rampupTimesteps* function, which increases the simulations' stability and accuracy since there are usually relatively larger changes in the saturation and pressure at the beginning of a

simulation schedule. Then, the *simulateScheduleAD* function is used for simulations using fully implicit formulation and adaptive time step adjustments in case of convergence failures.

For the carbonate rock simulations shown in this paper, a maximum time step of ~20 hours with ~10 geometrically ramped-up time steps show the best tradeoff between the accuracy and the simulation speed for most of the cases.

Parametrization of Saturation Functions: SCAL data are numerically calculated by varying $k_r(S_w)$ and $p_C(S_w)$ to be compared with the experimental measurements, e.g., pressure and saturation measurements. Traditionally, these saturation functions are constructed using parametrized power law functions. These functions are partly physically motivated (R. H. Brooks and A. T. Corey, 1964) and partly designed to allow an effective description of a wide range of rock types (Lomeland et al., 2005). The disadvantage of power laws is that they generally constrain the shape of the resulting saturation function. They also impact the history matching process, as they may cause highly non-unique response surfaces of the objective function that the optimizer is trying to minimize (Berg et al., 2021a).

In this work, saturation functions are constructed point by point since a higher flexibility was needed to describe the specific carbonate rock type. In the point-by-point approach, we interpolate linearly between adjacent points using the MRST *interpTable* function. Derivatives are then computed by the piecewise linear interpolant. To find the overall best match of $k_r(S_w)$ and $p_C(S_w)$, the SS and multispeed CF data sets are interpreted pairwise and simultaneously. The saturation points are chosen on the basis of the experimental average water saturations after steady conditions were reached. The achieved saturation ranges of the individual data sets may be different. In the present case of primary drainage, S_{cw} may be reached by CF but typically not by SS. Therefore, outside the SS saturation range, k_r is sensitive only to the CF measurement. The average of the saturation profiles at each fractional flow from SS defines the middle range water saturations, and the average water saturation from CF experiment defines the lower water saturations. In this way we define the water saturation vector on which the history matching process is performed. For simultaneous evaluation of $k_r(S_w)$ and $p_C(S_w)$, the MATLAB *fmincon* function automatically scales the input parameters to assist the optimization process. However, during the uncertainty quantification using the ParaDRAM package, no input parameter scaling is applied. To date, the point-by-point approach has not caused any numerical stability problems.

Steady-State and Unsteady-State Model: Steady-state and unsteady-state core flood experiments are modeled in a 1D linear domain as displayed in Figure 9 using the *tensorGrid* function in *MRST*. The domain size is adapted to the dimensions of the rock samples and regularly discretized in the flow direction with a grid size of 1 mm. This gridding scheme is

inspired from the work of (Maas and Schulte, 1997). As typical in SCAL, the domain is considered homogeneous in all rock properties and is populated with the experimentally determined average values for K and ϕ.
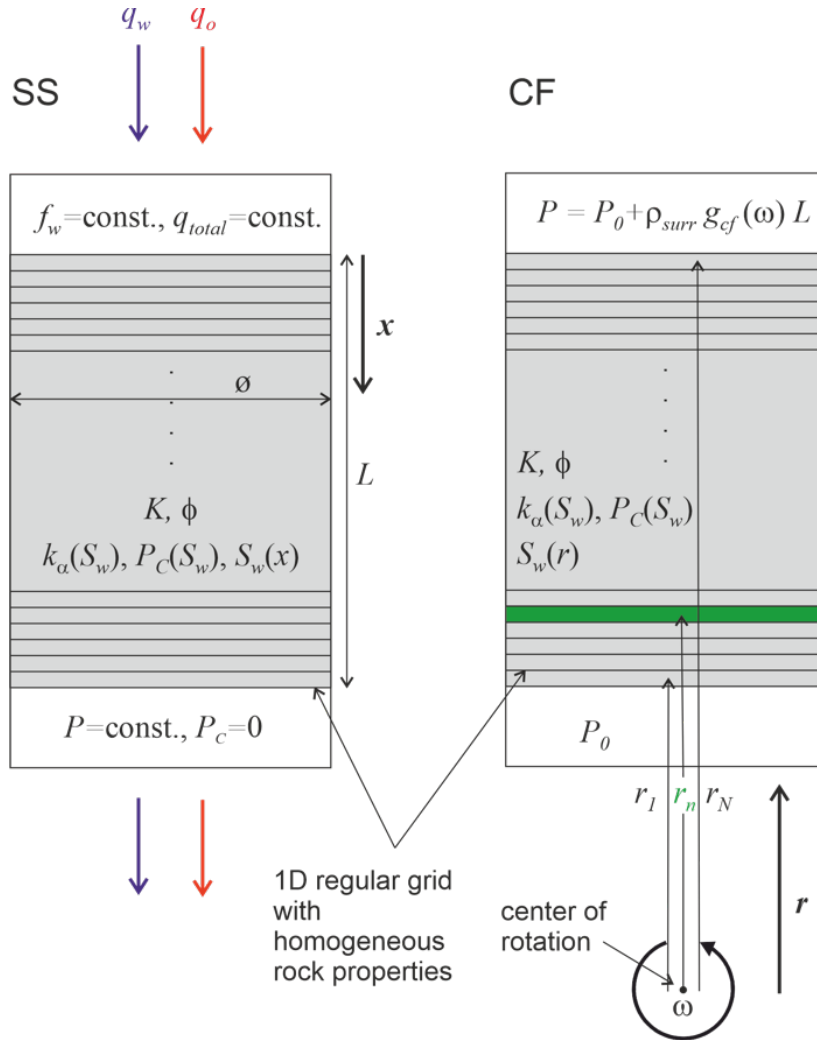

Figure 9: Modeling domains for matching steady-state (SS, left) and centrifuge experiments (CF, right). In this figure, f_w is the fractional flow of water, q_{total} total injected flow rate, ϕ porosity, P_C capillary pressure, K the absolute permeability, S_w water saturation, and P_0 initial pressure.

Extra grid blocks with the same volume are added to either end of the simulation domain to apply the inlet and outlet boundary conditions. By assigning $\phi = 1$, $P_C = 0$, and straight-line k_r functions, the discontinuity at the inlet and outlet boundary is introduced (Maas and Schulte, 1997). The experimental boundary conditions are also applied to these extra grids; at the inlet boundary cell, constant flow rates, and at the outlet, constant pressure boundary conditions are applied by using the *fluxside* and *pside* functions in the *MRST*.

The differential pressure is calculated as the pressure difference between the boundary cells at each end of the core. Since we assume the capillary pressure in these boundary cells to be zero,

the water and oil pressures are the same in both cells, and the reported differential pressure applies to the respective connected fluid phase in the domain. For the calculations of average water saturations, these boundary cells are omitted from the water saturation profile outputs since the boundary cells are not a part of the main core body.

For the initialization of the primary drainage processes, the water saturations in the inlet and outlet boundary cells are set to one, and for the first imbibition process, they are set to zero. These settings follow the experimental layout, with the experiments starting at $f_w = 1$ for drainage and at $f_w = 0$ for imbibition.

By realizing the boundary conditions as described referring to the experimental settings of the injection pumps and the backpressure system, the experimental responses can be modeled and compared to the actual measurements. These are the differential pressure as measured by pressure transducers and the 1D saturation profiles, which are determined by X-ray absorption measurements.

Multispeed Centrifuge Model: For modeling centrifuge experiments, the modeling domain is set up as for the SS and USS core flood experiments. However, the driving force refers to the gravity term in equation (4). The model geometry is given on the right side of Figure 9. In centrifuge experiments, gravity is applied by centrifugal acceleration $g_{cf} = \omega^2 r$, in which r denotes the distance from the center of rotation; therefore, gravity varies along the modeling domain, i.e., along the core sample.

For the simulations of an individual experimental step at a constant angular frequency ω, both ends of the core are assigned a constant pressure boundary condition. The pressure boundary conditions in CF experiments are governed by the hydrostatic pressure in the surrounding fluid that invades during the CF experiment. At the boundary toward the center of rotation, the pressure is set to a constant $P_0 = \rho_{surr} \omega^2 r_0$, while on the opposite side of the modeling domain, the gravitational head amounts to $P = \rho_{surr} \omega^2 r_{N+1}$, with r_0 and r_{N+1} being the positions of the two boundary grid blocks and ρ_{surr} being the density of the surrounding/invading fluid, which is oil in the case of drainage and water in the case of an imbibition process. Defining the boundary conditions as above allows us to establish the surrounding hydrostatic pressure and naturally account for the gravity-induced fluid flow in and out of the modeling domain.

A centrifuge device requires a certain time to reach the predefined angular velocity, which is called the startup time. This startup period affects the production profile, especially from cores with high absolute permeability. In the simulator, to account for the startup period we divide the startup rotation per minute (RPM) to the startup time and assume a linear increase in the centrifuge RPM to calculate a maximum rate at which the centrifuge RPM can change over

time (in the units of RPM/s). Then we scan through the CF rotation schedule and break it down into smaller RPM increase steps based on the maximum rate that the CF RPM can change. In the simulations, a startup period of 100 s to 2000 rpm is assumed, discretized in five 20-second steps.

2.2.1 History Matching

SCAL data interpretation by numerical history matching is well established but not yet common practice. A best practice is an assisted history matching procedure based on a user-defined objective function to be minimized, which also allows for a subsequent uncertainty analysis (Berg et al., 2021a). In this work, we go two steps beyond: first, similar to (Maas et al., 2019; Prores, n.d.), we analyze data sets of different measurements simultaneously instead of subsequently. Simultaneous analysis facilitates finding the best combined match of $k_r(S_w)$ and $p_C(S_w)$ by minimizing a common and normalized objective function. Second, in numerical HM, the $k_r(S_w)$ and $p_C(S_w)$ functions are typically represented by power laws, which is physically expected for simple rock types (Corey, 1954; R. H. Brooks and A. T. Corey, 1964). The present module also allows a point-by-point description of $k_r(S_w)$ and $p_C(S_w)$ to match experimental data from highly complex rock types without the limitations of specific power-law representations.

In general, numerical HM is an underdetermined process, for which the Levenberg–Marquardt algorithm is used because of its robustness to the starting values (Berg et al., 2021a; Maas et al., 2019). However, in contrast to the Levenberg–Marquardt approach, the *MATLAB fmincon* function implements interior-point or active-set algorithms in which a constrained nonlinear optimization algorithm allows for the implementation of inequalities; inequalities are essential for the aspired point-by-point approach to enforce monotonic behavior of k_r and p_C saturation functions, which is naturally the case by power-law representations. Monotonicity is demanded from a physical point of view, since we do not expect that, e.g., the phase permeability decreases with increasing saturation.

Inside the *fmincon* function, we set the optimization algorithm to be the *active set,* as it provides the best possible results by minimizing the following objective function:

$$K = \frac{1}{N_{obs}} \sum_{i=1}^{N_{obs}} \left(\frac{d_i - y_i}{d_i}\right)^2 \qquad (5)$$

where d_i are the observed experimental values, y_i are the simulated responses, and N_{obs} is the number of parameters, which is equal to the number of measured data points. Various objective functions are reported in the relevant literature (Berg et al., 2021b). The convergence criteria

for the *fmincon* function is the default 10^{-6} difference between the two last calculated objective function values. The χ^2 function is most commonly used as objective function for history matching purpose, however we found equation (5) to be more suitable for the simultaneous history matching of SS and CF experiments and point-by-point representation of the saturation tables. Simultaneous experiments affect the data that we are matching (causing a different error surface) and the choice of representation affects the points that we are iterating on. This is because the measurements are at different scales (i.e., numerical values) and at different resolutions (i.e., point density), which is accounted for by the well-normalized objective function in equation (5). The available analytical solutions serve as a starting point for the HM process, which ensures that the solution is close enough to the optimal solution to minimize the chances of approaching a local minimum instead of the optimal solution.

2.2.2 Uncertainty Modeling

After finding a match between the experimental and numerical responses, we explore the response surface around our optimal solution and determine its sensitivity. As also shown by (Berg et al., 2021a), the history matching problem is ill-posed with local minima. In such cases, solutions through a Hessian matrix and a χ^2 analysis may fail. Instead, we opt for MCMC sampling.

In the traditional MCMC methods, manual tuning of parameters within the sampling algorithm may be required to ensure the convergence of the Markov chain to the target densities for the problem at hand. To avoid manual tuning, we use the ParaDRAM library, which offers a practical implementation of the delayed-rejection adaptive-metropolis MCMC or DRAM algorithm. DRAM is fully automated regarding the selection of the free parameters and is an extension of the traditional Metropolis–Hastings (MH) method (Shahmoradi and Bagheri, 2020).

The DRAM algorithm combines two algorithms, namely, the delayed-rejection (DR) and adaptive-metropolis (AM) algorithms. The AM algorithm, as opposed to the MH algorithm, adapts the proposal distribution based on the past history of the Markov chain (the points sampled thus far), and the DR algorithm improves the efficiency of the MCMC sampler, especially in higher dimensional problems; in high-dimensional domains, the number of rejections can become more significant than the acceptance, strongly compromising the efficiency of the sampler. Therefore, DRAM can be useful since the point-by-point construction of saturation functions refers to a high-dimensional space. Furthermore, this method is particularly useful for multimodal target density functions separated by deep valleys of low likelihood. Therefore, in the case of multiple local minima in the objective function response surface, this method can help us find them (Kumbhare and Shahmoradi, 2020).

The MatDRAM algorithm (Kumbhare and Shahmoradi, 2020) (existing in the ParaDRAM library) offers a practical variant of the generic DRAM algorithm relaxing the requirements for (a) a set of delayed-rejection-stage proposal distributions and (b) reduces the complexity of the acceptance probability. Symmetric proposal distributions with a fixed shape are used through the DR process, and the scales are determined through a user-defined schedule. To run the MCMC simulations, we use a likelihood estimation function as follows:

$$J = \frac{1}{N_{obs}} \sum_{i=1}^{N_{obs}} -\frac{1}{2}(\frac{d_i - y_i}{error \cdot d_i})^2 \qquad (6)$$

where $error$ is a fixed value between 0 and 1 (expressed as a percentage below) and we multiply -1/2 to this function since here we aim to maximize the probability rather than minimizing as in equation (6). We assume a relative error of 2.5% for the pressure reading, 1% for the saturation profile of SS experiments, and 1% for the average water saturation of CF experiments. These fixed error values are simple assumptions coming from the experimental measurements' average standard deviation after steady state was reached. The experimental measurements act as observed (true) values, and through ParaMonte iterations, J is calculated from simulation predictions. During the MCMC simulations, $k_r(S_w)$ is hard bounded between zero and one, and $p_c(S_w)$ bounds are set to be half and double the optimum values (the minima – or the best saturation function - which is found in the history matching simulations) as lower and upper boundaries.

To force a monotonic behavior of the point-by-point saturation functions, we define a prior inequality function that checks if:

$$Ax \leq b \qquad (7)$$

Where x is a vector, containing the parameters that are history matched, and the matrix A and vector b are defined in a way to have:

$$x_i \leq x_{i+1} \text{ or } x_i \leq x_{i-1} \qquad (8)$$

based on the type of monotony that is forced on the parameters. This inequality is run before the likelihood estimation above (equation (6)), and if it is not valid, we reject the sample before running the simulations to save computational time. In this function, we create the A and b matrix, in the same way the inequalities are forced in the MATLAB optimization toolbox and reject the samples that are not monotonic prior to our main likelihood estimation function. This method saves computational time by not rejecting samples without running the main likelihood estimation function.

2.2.3 Introducing Heterogeneity

To model the heterogeneous saturation profiles, as presented in Figure 20 (c) and (f), the methodology presented by(Hosseinzadeh Hejazi et al., 2019) is used. The authors characterize core heterogeneity by scaling the capillary pressure in the grid block. In the methodology implemented here, the 1D simulation domain is divided into 2-mm-size slices, which captures the sample heterogeneity with considerable detail. Each grid (j) is assigned a distinct value for capillary pressure $P_c^j(S)$, porosity ϕ_j, and absolute permeability K_j. Small-scale variations in fluid saturation by capillary heterogeneity can be quantified through variations in capillary entry pressure for each grid element in the system(Hosseinzadeh Hejazi et al., 2019). In Brooks-Corey parametrization (R. H. Brooks and A. T. Corey, 1964), this entry pressure is denoted as P_d; therefore, we have:

$$P_c^j(S) = \frac{1}{f_j} P_c(S) = \frac{P_{dj}}{P_d} P_c(S) \quad j = 1, \dots, N, \tag{9}$$

where f_j is the scaling factor, N is the number of elements in the system and P_{dj} is the entry pressure for the jth element. $P_c(S)$ is the reference capillary pressure curve, which is measured experimentally by MICP or by history matching SCAL experiments. To consider heterogeneity, we use Brooks-Corey parametrization for the reference capillary pressure, and we history match its parameters to calculate the system's capillary pressure. To calculate the spatial variations in porosity and absolute permeability, we use the Leverett-J function, $J(S)$, which states:

$$J(S) = \sqrt{K/\phi} \frac{P_c(S)}{\gamma} \tag{10}$$

Analogous to the formulation for capillary scaling, we can write:

$$f_j = \frac{P_d}{P_{dj}} = \sqrt{\frac{K_j/\phi_j}{K_m/\phi_m}} \tag{11}$$

where K_j and ϕ_j are the absolute permeability and porosity for each grid element and K_m and ϕ_m are the experimentally measured average porosity and permeability of the core, respectively. For heterogeneous modeling, the steady-state saturation profile can be calculated using the equation below:

$$\frac{dS}{dx_D} = \left(\frac{q\mu_{nw}I}{AK_j}\right)\left(\frac{1}{k_{r,nw}(S)}\right)\left(\frac{f_j}{dP_c(S)/dS}\right), \tag{12}$$

in which we solve for the jth element of the system. This equation is similar to the one that we solve for homogeneous modeling, except f_j is multiplied by the last term of the equation. In the simulator developed for this purpose (based on MRST), a saturation number is assigned to each

grid element, and the capillary pressure of each element is divided by the corresponding scaling factor f_j. To calculate the scaling factors, we minimize the following objective function:

$$E(x_j) = \sum_{k=1}^{N_q} \left(\frac{P_c\left(S^{exp}(x_j)\right) - f_j P_c\left(S^H(x_j)\right)}{P_c\left(S^{exp}(x_j)\right)} \right)^2 , j = 1, \dots, N, \tag{13}$$

where P_c is the reference capillary pressure curve, f_j is the scaling factor, $S^{exp}(x_j)$ is the slice average water saturation measured during the experiment, and $S^H(x_j)$ is the saturation profile calculated with homogeneous simulations. This approach is justified since the capillary pressure profile is almost unaffected by small-scale heterogeneities (Hosseinzadeh Hejazi et al., 2019).

Having calculated the scaling factors using equation (13), we then calculate K_{hm} using equation (11) and the porosity profile shown in Figure 20 (c). Therefore, for heterogeneous modeling, each grid cell has three distinct properties, namely, porosity ϕ, absolute permeability K (calculated from equation (11)), and capillary scaling factor f (calculated using equation (13))

The numerical responses of the pressure difference ΔP, brine production Q, and saturation profiles $S(x)$ are then history matched to the experimental measurements using a multiobjective error function that is minimized using the genetic algorithm from the MATLAB optimization toolbox:

$$I = \frac{1}{N}\sum_{j=1}^{N} \left(\frac{\Delta P^{sim}(x_j) - \Delta P^{exp}(x_j)}{\Delta P^{exp}(x_j)} \right)^2$$

$$J = \frac{1}{N}\sum_{j=1}^{N} \left(\frac{Q^{sim}(x_j) - Q^{exp}(x_j)}{Q^{exp}(x_j)} \right)^2 \tag{14}$$

$$K = \frac{1}{N}\sum_{j=1}^{N} \left(\frac{S^{sim}(x_j) - S^{exp}(x_j)}{S^{exp}(x_j)} \right)^2 .$$

In the methodology presented by (Hosseinzadeh Hejazi et al., 2019), the capillary pressure scales are calculated from steady-state drainage experiments, in which the saturation profiles at the end of each fractional flow were evaluated. The novelty of the methodology presented here is the analysis of single-rate drainage experiments. For this purpose, the scaling factors are calculated from one saturation profile at the transient state and one at the steady state, i.e., late in the injection period.

2.3   Numerical Stability Analysis

This section is dedicated to the materials and methods used to analyze the stability of CO_2 brine displacement in Chapter 5. Here the same numerical tool as explained in section 2.2 is used – however the tool is further developed to fit the purpose of analyzing viscous fingers in immscible displacement.

2.3.1   Numerical Setup

An Open-Source Darcy-scale numerical simulator based on MATLAB-MRST-based was used for the simulations – similar to numerical setup of section 2.2 - assuming incompressible and immiscible fluid phases (Omidreza Amrollahinasab et al., 2023) utilizing the MRST AD toolbox (Krogstad et al., 2015) for improved stability and accuracy in particular at the initial stages when changes in saturation and pressure are typically more pronounced. Two-phase flow is described by the material balance equation and Darcy's law. In the absence of source and sink terms, the material balance is expressed as: $\phi \frac{\partial S_\alpha}{\partial t} + \nabla \cdot \mathbf{v}_\alpha = 0 \ \alpha = w, co_2$ where ϕ is the porosity and S_α is the phase saturation and $\mathbf{v}_\alpha$ is the Darcy phase velocity vector in units of m/s. Without the restriction to a specific combination of fluids, we refer the two phases α to water (w) and CO_2 in the following. The Darcy velocity $\mathbf{v}_\alpha$ is given by Darcy's law: $\mathbf{v}_\alpha = -\frac{k_{r\alpha}}{\mu_\alpha} K (\nabla p_\alpha - \rho_\alpha \mathbf{g}) \ \alpha = w, co_2$ where $k_{r\alpha}$ are the dimensionless relative permeability saturation functions and μ_α are the (constant) phase viscosity in Pa· s. K is the absolute rock permeability in m², p_α are the phase pressures in Pa, and $\mathbf{g}$ is the gravitational constant in m/s². The phase saturation satisfies $S_w + S_{co_2} = 1$, and incompressible flow is further restricted to $\nabla \cdot (\mathbf{v}_w + \mathbf{v}_{co_2}) = 0$. Adaptive time-step was implemented in the simulations to ensure accurate shock front representation and minimize numerical dispersion (Figure 29C).

Simulations were performed on 2D domains with lengths ranging from 15 cm to 90 m and an aspect ratio of 2 between length and width. The simulation domains were discretized with a Cartesian grid of $800 * 400$ blocks. A typical result of the numerical simulation is displayed in Figure 41.

The discretization level of the fingers was kept constant to maintain a constant numerical dispersion. A critical aspect of our analysis is that the simulated dispersion is physical and not numerical in nature; therefore, great care was taken to ensure that the solver generated shock fronts controlled by capillary dispersion. This is shown in Figure 29C, where the saturation fronts of the 1D simulations are compared with the slice averaged saturation fronts from the 2D results. The 1D simulations were performed on a comparable domain with 800 grid blocks,

otherwise using the same parameters as the 2D simulations, except for the random permeability field introduced in the 2D simulations to induce viscous fingers.

2.3.2 Rock and Fluid Properties

The input parameters were derived from a series of laboratory experiments on CO_2-brine displacement in Berea sandstone under realistic sequestration conditions (Berg and Ott, 2012). The interfacial tension σ was tested within a range from 0 to 30 mN/m covering a range of gaseous, supercritical CO_2 cases down to miscibility with brine (Georgiadis et al., 2010) , which is perhaps less relevant for CCS but useful to test the scaling relationship. The capillary pressure curve was measured experimentally at an $\sigma = 50 mN/m$ so the experimental curve was scaled with the desired σ for each simulation using Young-Laplace equation as $P_c^{(new)} = P_c^{(measured)} \cdot \frac{\sigma^{(new)}}{\sigma^{(measured)}}$. To build the relative permeability, the Corey parametrization (Corey, 1954; R. H. Brooks and A. T. Corey, 1964) was used with the following parameters: $S_{w\ residual} = 0.2$, $S_{co_2\ residual} = 0$, $K_{rw\ max} = 1$, $K_{rco_2\ max} = 0.5$, $n_w = 2$, $n_{co_2} = 3.5$.
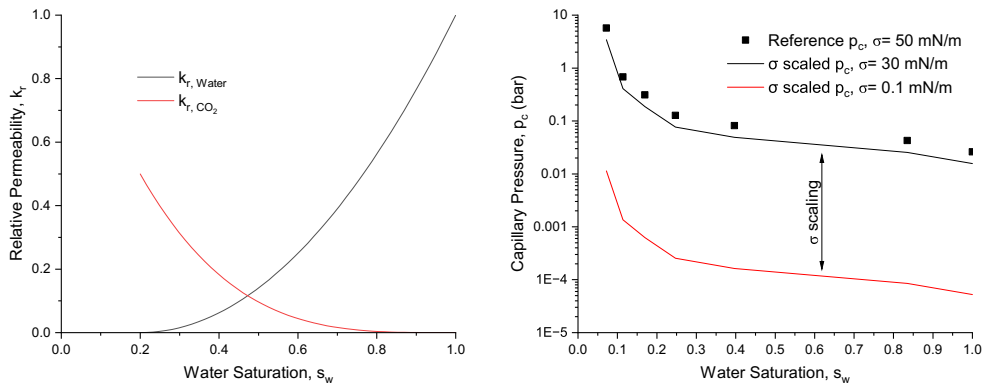
Figure 10: Relative permeability and capillary pressures used for stability analysis of CO_2-brine immiscible displacement.

The capillary number $Ca = \mu v/\sigma$ ranged from 5.7×10^{-8} to 1.9×10^{-10}, implying that relative permeability is not a function of interfacial tension. Injection rates were adjusted in proportion to the inlet size to maintain a consistent linear flow velocity of $v = 8.48 \times 10^{-6}$,m/s. The porosity was set at 22.2%, and the permeability was set at 380~mD. To encourage the formation of fingers, a uniform random permeability field variation of 1% was introduced. The viscosity of brine was set to 0.674~cp and the viscosity ratio was set to 1000, representing a situation for gaseous CO_2, chosen as a convenient demonstration case; however, the principle is also valid for other conditions, e.g., supercritical CO_2 with smaller viscosity ratios as long as the stability criteria are met (Maas et al., 2023).

2.3.3 Determination Of Wavelength and Self-Similarity

The wavelength of the fingers varies strongly with the interfacial tension σ (see Figure 26) Therefore, for a reliable determination of the finger wavelength, λ, the size of the simulation domain was varied to obtain a similar number of fingers for the different σ settings, as indicated in Figure 26. Since we are targeting the onset of instability, a good criterion must be found at which point the wavelength is evaluated. We are safe at the onset when the amplitudes of the fingers are on the order of λ (see Figure 29A). This criterion also prevents secondary effects such as merging or coalescence of fingers from distorting the results (Kampitsis et al., 2021; Lanza et al., 2023; Nijjer et al., 2018).

Using this criterion, self-similar behavior was observed across the interfacial tension (σ) and length scales. Figure 29C shows the 1D (black lines) and 2D (blue lines) longitudinal dispersion curves superimposed as a function of the dimensionless distance X_D. The agreement within the respective data sets shows the tendency for capillary dispersion and dispersion by fingering to scale linearly with σ and not with the square root of σ as commonly expected, which is equivalent to the key aspect of the present work.

Chapter 3

1D-Homogeneous Stochastic Interpretation of Displacement Experiments

This chapter is a reprint of (Amrollahinasab et al., 2022; Omidreza Amrollahinasab et al., 2023) and the code for this chapter is available at (Amrollahinasab and Azizmohammadi, 2022).

3.1 Development of DPE SCAL simulator

Understanding multiphase flow in porous media is pivotal to Geoenergy Engineering applications like CO_2 storage and oil recovery. However, inherent uncertainties exist regarding key parameters that govern fluid dynamics in reservoirs, especially relative permeability and capillary pressure saturation functions. This chapter tackles these uncertainties through the development of an advanced simulator for analyzing core flooding experiments. Specifically, the limitations of traditional SCAL analysis methods are examined and a stochastic approach to numerically interpret multiple data sets simultaneously is introduced. Further on a flexible point-by-point parameterization of saturation functions along with the probability distributions and correlations between matched parameters are calculated. By enhancing the interpretation of lab-scale displacement tests, this work aims to improve the characterization of subsurface reservoirs. The outcomes will support more robust predictions of CO_2 plume migration in the context of carbon capture and storage.

3.1.1 Special Core Analysis

Special Core Analysis (SCAL) is a technique widely used in reservoir engineering to quantify multi-phase flow in reservoir rocks under reservoir conditions. SCAL data provide essential inputs for reservoir simulations, helping to predict the performance of oil and gas reservoirs

over time. However, the interpretation of SCAL data has long been a topic of research and debate, particularly regarding the characterization of relative permeabilities and capillary pressure — key parameters that govern multiphase flow in porous media. Traditional interpretation methods often rely on certain assumptions and simplifications, which may not hold for more complex rock types, leading to potential inaccuracies in the derived saturation functions.

This chapter focuses on introducing and applying a comprehensive workflow to interpret SCAL data, specifically targeting the complexities associated with two-phase flow of CO_2 and brine in carbonate rocks. The work aims to provide a more accurate and objective interpretation of experimental data by leveraging numerical history matching techniques and a novel point-by-point parameterization approach. This research seeks to improve the understanding of two-phase flow in complex rock types, contributing to better reservoir management strategies and more accurate predictions of oil recovery.

The objectives of this research are threefold:

1. To critically examine the limitations of traditional power-law representations and the implications for interpreting complex SCAL data.
2. To develop and apply a simultaneous point-by-point approach in interpreting steady-state (SS) and centrifuge (CF) experimental data sets, providing a more flexible and accurate characterization of saturation functions.
3. To assess the uncertainties involved in the history matching process through Monte Carlo Markov Chain (MCMC) simulations and to investigate the impact of sample-to-sample variation on the derived results.

Through these objectives, this chapter aims to enhance the reliability and accuracy of SCAL data interpretation, ultimately leading to a better understanding of the complex multiphase flow processes in carbonate reservoirs and their uncertainties. The outcomes of this chapter are expected to have significant implications in the field of reservoir engineering, particularly in improving reservoir simulation predictions and optimizing oil recovery strategies. By offering a more flexible and comprehensive approach to SCAL data interpretation, this work contributes to bridging the gap between experimental observations and numerical simulations, promoting a more accurate representation of real-world reservoir conditions. The code developed in this chapter is open-sourced under (Amrollahinasab and Azizmohammadi, 2022) and it is also available as a part of MRST modules called ad-SCAL available to download (Sintef, 2023).

Dynamic reservoir simulations require relative permeability ($k_r(S_w)$) and capillary pressure ($p_C(S_w)$) saturation functions when immiscible fluid displacement is of concern. Common examples are water flooding for oil production (water/oil), the production of deep geothermal

systems (water/steam) and the geological storage of CO_2 (water/CO_2). In these operations, $k_r(S_w)$ and $p_C(S_w)$ decisively dominate the fluid displacement efficiency, sweep efficiency and injection/production pressure. History matching (HM) and predicting reservoir performance by numerical simulations therefore require an accurate input for those saturation functions. Classically, $k_r(S_w)$ and $p_C(S_w)$ are measured in laboratories by core flooding, which is subject to special core analysis (SCAL).

In SCAL, relative permeability is measured by the flooding experiments e.g. steady-state (SS) method, in which the two fluid phases, e.g., oil and water or CO_2 and water, are injected simultaneously at a constant total injection rate and at a certain fractional flow. By measuring the differential pressure and the water saturation after reaching steady-state conditions, Darcy's law can be used to calculate the relative permeability at that fractional flow point, and the scanning of the fractional flow curve allows us to measure the entire relative permeability curves. However, typically, the measured differential pressure cannot be assigned to a single S_w, since capillarity influences the fluid distribution in the rock—the so-called capillary end effect—$k_r(S_w)$ and $p_C(S_w)$ are coupled (Huang and Honarpour, 1998; Leverett, 1941). Furthermore, in flooding experiments, the saturation endpoints are typically not reached in a finite time. Toward endpoints, relative permeability measurements are often extended by other experimental methods, such as single-speed centrifuge experiments. In these examples, it turns out that single measurements may not describe a saturation function sufficiently, which means that measurements and analyses need to be combined. This is due to the natural inference of $k_r(S_w)$ and $p_C(S_w)$ in any type of two-phase flow experiments. For this reason, the classic analytical solutions to the SCAL experimental methods, such as using Darcy's law for SS, JBN analysis (Johnson et al., 1959) for un-steady state (USS), and Hassler–Brunner (Hassler and Brunner, 1945) and Hagoort's (Hagoort, 1980) approaches for the analysis of centrifuge measurements, fail, as does the numerical description of individual data sets (Maas and Schulte, 1997).

By numerical data interpretation, the full physical picture can be considered by a subsequent interpretation of $p_C(S_w)$ and $k_r(S_w)$ experiments or by a simultaneous interpretation of data sets (Loeve et al., 2011; Maas et al., 2011). The latter case does not refer to the best match of the individual data set but to the best combined description, leading to a robust and reliable interpretation. Numerical SCAL interpretation refers to the inverse modeling approach, in which the simulation results are iteratively matched to the experimental data. However, inverse modeling is an ill-posed problem with intrinsic uncertainties (Berg et al., 2021a). Non-uniqueness and instabilities in part are the results of weighting assigned in the objective function, averaging methods applied and experimental uncertainties such as

instrumental noise and systematic errors. It is also not necessarily given that the underlying physical model is sufficient to describe experimental observations. Examples may be simple, e.g., sample heterogeneity that is typically not accounted for in SCAL interpretation, and pressure and saturation fluctuations by ganglion dynamics are not represented in the modeling approach using Darcy's law (Berg et al., 2021b; Rücker et al., 2021). Additionally, the restriction to certain parametrized representations of $p_C(S_w)$ and $k_r(S_w)$, such as the Brooks Corey (R. H. Brooks and A. T. Corey, 1964), modified Corey (Corey, 1954) or LET (Lomeland et al., 2005) representations, may be a threat for the interpretation of complex rocks such as carbonates (Berg et al., 2021a). As a result of this discussion, single representations of p_C and k_r saturation functions may not be sufficient for reliable reservoir flow predictions; uncertainty intervals should be included in modern stochastic reservoir modeling. The first promising attempts in this direction have been made in (Berg et al., 2021a, 2021b). However, neither numerical interpretation nor uncertainty modeling is yet common practice in SCAL interpretation. A reason may be that the sophisticated SCAL simulation tools are proprietary, which hinders developments in this area.

With this chapter, we provide an MRST-based open-source simulator running in MATLAB, for a comprehensive interpretation of SCAL experiments. The work focuses (a) on uncertainty modeling and probabilistic analysis following a Monte Carlo type of sampling with the goal of obtaining realistic intervals for early decision making and stochastic reservoir modeling. (b) Saturation functions are optionally constructed differently from common representations, depending on the complexity of the rock type under investigation. For the interpretation of rock types with a high complexity (the majority of carbonates), we introduce an optional point-by-point approach, which does not follow a specified mathematical function. With this approach, we overcome the limitations of the classic parametrization, which is demonstrated and discussed on a complex carbonate. The simulator runs forward simulations with the MATLAB Reservoir Simulation Toolbox (MRST) (Lie, 2019). The gradient-based history matching used the MATLAB optimization toolbox. We also employed parallel high-performance delayed-rejection adaptive-metropolis Markov chain Monte Carlo (MCMC) (ParaDRAM) (Shahmoradi and Bagheri, 2020), all of which are open-source toolboxes built in MATLAB.

3.2   Benchmarking

The model's accuracy was verified by using synthetic data sets published by (Lenormand et al., 2017) and (Loeve et al., 2011) for the forward modeling and history matching modules, respectively. The simulator has been benchmarked with 5 simulation cases to the results of accepted SCAL simulators by comparing the results to (Lenormand et al., 2017). Figure 11

shows (a) the $k_r(S_w)$ and (b) the $p_C(S_w)$ input and the comparison with the differential pressure and saturation data simulated by the SCORES simulator expressing $k_r(S_w)$ with a Corey model and $p_C(S_w)$ as tabulated values. Case 1 (c) represents the differential pressure during SS imbibition in a neutral-wet system.

For the benchmark and verification, the extended Corey model (Corey, 1954; R. H. Brooks and A. T. Corey, 1964) is used as to parametrize the relative permeability as:

$$S_w^* = \frac{S_w - S_{wc}}{1 - S_{wc} - S_{nr}} \tag{15}$$

$$k_{rw} = K^0{}_{rw}(S_w^*)^{n_w} \tag{16}$$

$$k_{ro} = K^0{}_{ro}(1 - S_w^*)^{n_o} \tag{17}$$

Where S_w^* is the rescaled water saturation since the water saturation is bounded by connate water saturation S_{wc} and residual non-wetting saturation S_{nr}. k_{rw} is the water relative permeability, $K^0{}_{rw}$ is the water relative permeability at residual oil saturation, and n_w is the water exponent. k_{ro} is the oil relative permeability, $K^0{}_{ro}$ is the oil relative permeability at connate water saturation, and n_o is the oil exponent.

The modified Skjaeveland model presented by (Loeve et al., 2011) is used to parametrize the capillary pressure. This formulation divides the saturation into three zones. The low water saturation is divided into three zones. If the water saturation is between S_{wc} and S_{wd} then the capillary pressure is:

$$p_c = \frac{c_{wi}}{(\frac{S_w - S_{wc}}{S_{wd} - S_{wc}})^{a_{wi}}} - c_{wi} + S_{wd} * r_i + b_i \tag{18}$$

If the water saturation is between S_{wd} and S_{od}:

$$p_c = S_w * r_i + b_i \tag{19}$$

if the water saturation is between S_{od} and S_{or}:

$$p_c = \frac{c_{oi}}{(\frac{1 - S_w - S_{or}}{1 - S_{od} - S_{or}})^{a_{oi}}} - c_{oi} + S_{od} * r_i + b_i \tag{20}$$

In this formulation for the synthetic history matching of the benchmarks a_{wi} and a_{oi} are set to 2. The details of the saturation function parameters used for different benchmark and verification cases are shown in Appendix A.

The synthetic data set includes bump floods as typically performed at the end of SS experiments to increase the accessible saturation window. Figure 11 (d) refers to a water-wet primary drainage process and the respective average water saturation from a CF experiment.
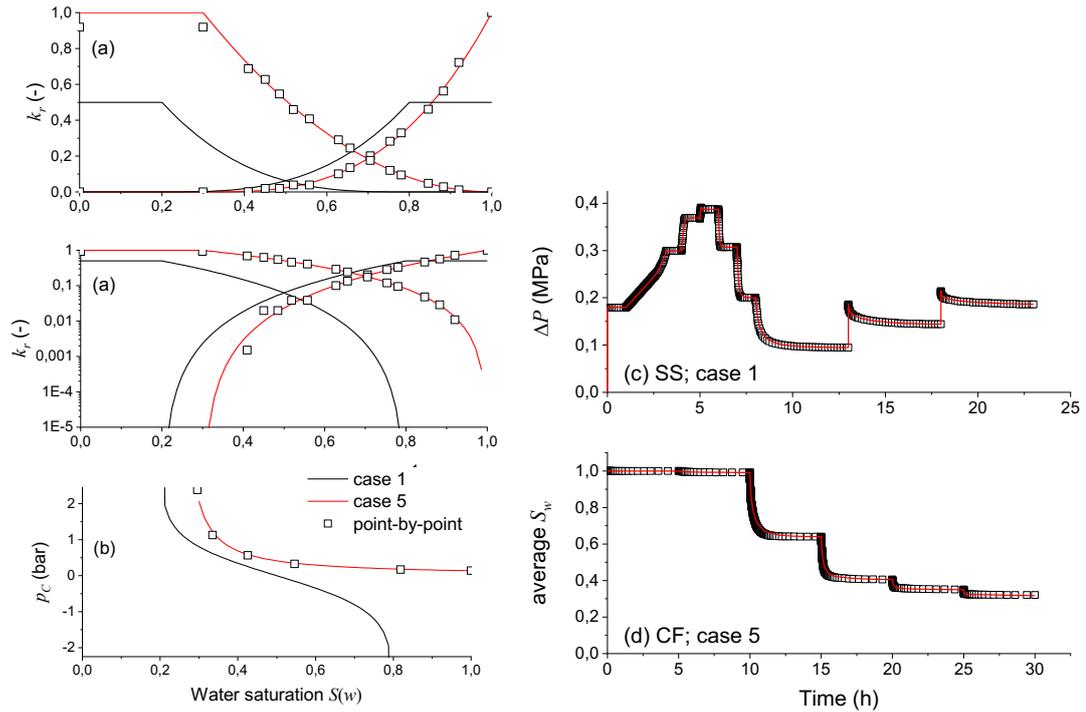
Figure 11: Verification by forward simulation using the reference data set presented by (Lenormand et al., 2017)*. (a) and (b): Relative permeability and capillary pressure saturation functions, respectively, for primary drainage (case 5) and first imbibition (case 1). Panels (c) and (d) show the forward simulated differential pressure from SS (case 1) and the simulated average water saturation of the CF experiment of case 5, respectively. The symbols are simulated with SCORES, and the lines correspond to the simulator developed in the present work. The open squares in (a) and (b) refer to point-by-point matches of forward simulated experimental responses.*

All simulation results show perfect agreement between all simulators, including the one developed in this work. For case 1, a domain discretized into 80 grid cells and a maximum time step of 0.2 h lead to a runtime of ~16 s using a 9th series core i7 Intel CPU. For this benchmark we use *simulateScheduleAD* with the default parameters – fully implicit scheme and *LinearSolverAD* that calls standard MATLAB direct solver mldivide.

To benchmark the HM module and to demonstrate the MC uncertainty quantification, we use the synthetic data set by (Loeve et al., 2011) to simultaneously match an USS and multi-speed CF imbibition experiment. The data set consists of unsteady-state (USS) and multispeed centrifuge simulated calculations (the synthetic pressure and production data). The Corey-type $k_r(S_w)$ (R. H. Brooks and A. T. Corey, 1964) and the Skjaeveland-type (Skjaeveland et al., 2000) $p_C(S_w)$ input functions are shown in Figure 12 (a) and (b). The upper and lower bounds as well as the starting point of the HM are chosen as in (Loeve et al., 2011). The results are shown in the same panels. Deviations from the true values are found at connate water saturation and the oil endpoint relative permeability. The reason may be the limited information an USS

imbibition experiment delivers at low water saturations. The uncertainty analysis is performed by assuming a 2.5% relative error for the pressure and production responses. Figure 12 (c) shows the resulting histograms and the two-parameter correlations for the relative permeability functions. On the contour plots, the Pearson's correlation strengths are given in addition to red numbers (Pearson, 1895). Strong correlations are found between the endpoint relative permeability and endpoint saturations of the complimentary phase, as evident in the Pearson's correlation matrix. The endpoint relative permeability also shows a strong correlation with the respective Corey exponents. This is a property of the specific mathematical representation of the saturation functions. For example, a change in the oil Corey exponent directly modifies the oil endpoint relative permeability at a given connate water saturation. The correlations may also provide a physical interpretation as far as the used function is physically motivated.

Above, the classic power-law representations are used to history match (HM) the synthetic datasets and benchmark the SCAL simulator HM module. In the point-by-point representation of the saturation functions, how many free history-matching parameters we have is determined by the count of the fractional flow steps implemented in the SS experiment, and the count of different rotational speeds implemented in the CF experiment. We use the $k_r(S_w)$ and $p_c(S_w)$ of (Lenormand et al., 2017) case 5 as input to simulate the primary drainage SS and CF experiments with 12 SS fractional flow (f_w) steps and 5 CF centrifugal speed steps. The simulated experimental responses are then matched with the point-by-point approach using the analytical solutions as starting points. The resulting saturation curves are shown as scatter graphs in Figure 11 (a) and (b). Naturally, the solution shows a certain scatter but describes the input saturation functions well. Deviations are found at the oil endpoint k_r. This may be expected since the SS drainage does not reach true S_{wc} and the centrifuge is missing sensitivity to k_r of the invading phase at that point.
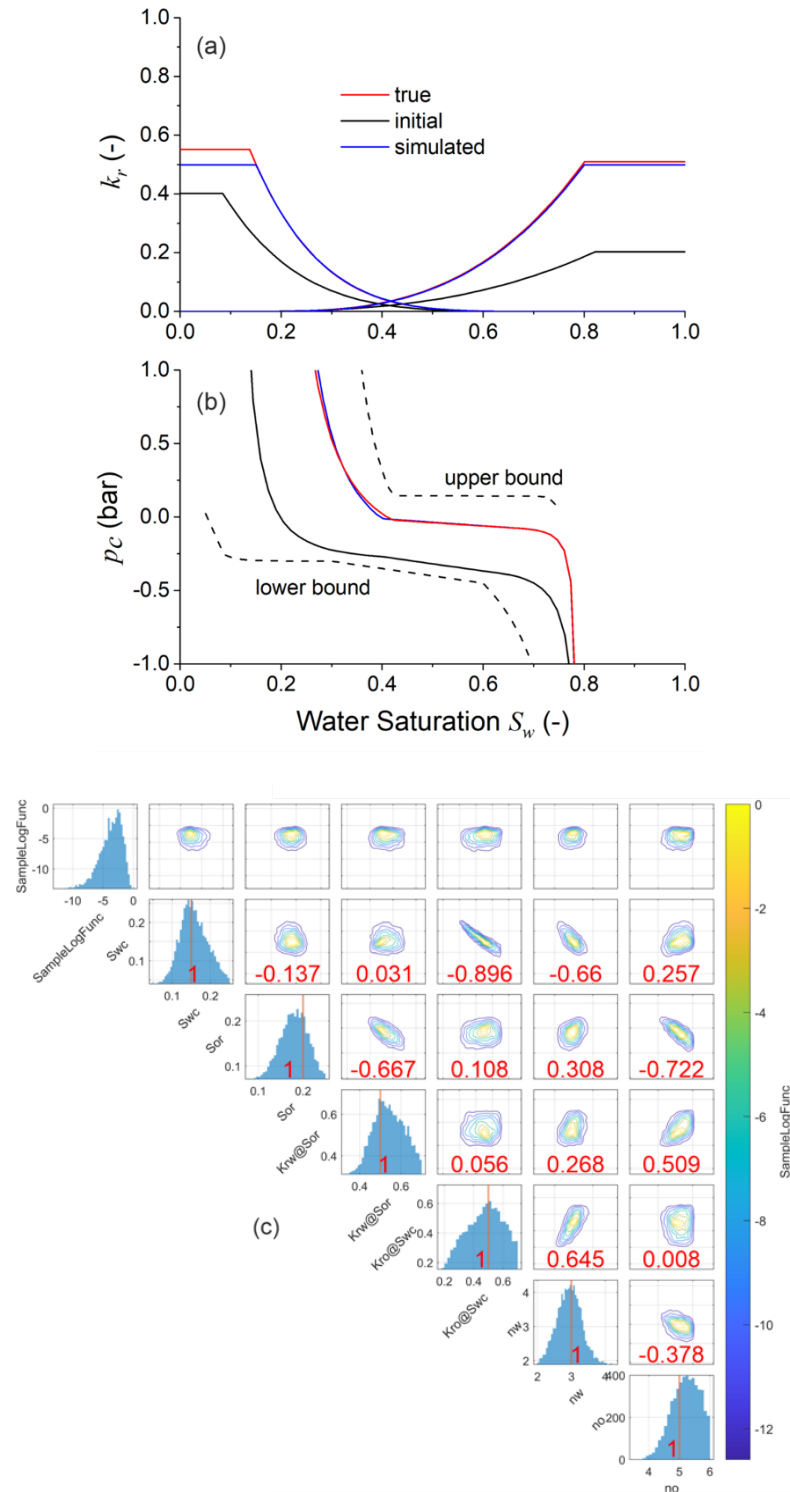
Figure 12: Simultaneous history matching and uncertainty quantification for benchmarking. Synthetic data sets of an unsteady-state and a multispeed centrifuge experiment (Loeve et al., 2011) are matched with modified Corey and Skjaeveland parametrizations. True values, starting points and the matches are shown in (a) for relative permeability and (b) capillary pressure (see text for details). (c) shows the result of the MCMC uncertainty analysis. The diagonal shows the single parameter probability distribution (histograms). The off-diagonal elements (contour plots) show the two-parameter correlations for the relative permeability curves. The red numbers refer to the Pearson correlation strength matrix.

3.3   Enhanced SCAL Interpretation

The real case study is performed on an SCAL data set of Estaillades limestone. The data set consists of two steady-state primary drainage relative permeability measurements and three multispeed centrifuge experiments. The experiments have been pair-wise simultaneously matched. Data from a CF/SS combination (samples 2 and 5) are shown in Figure 13. Details about the rock type and rock properties of the individual plugs are summarized in the Materials and methods section above.
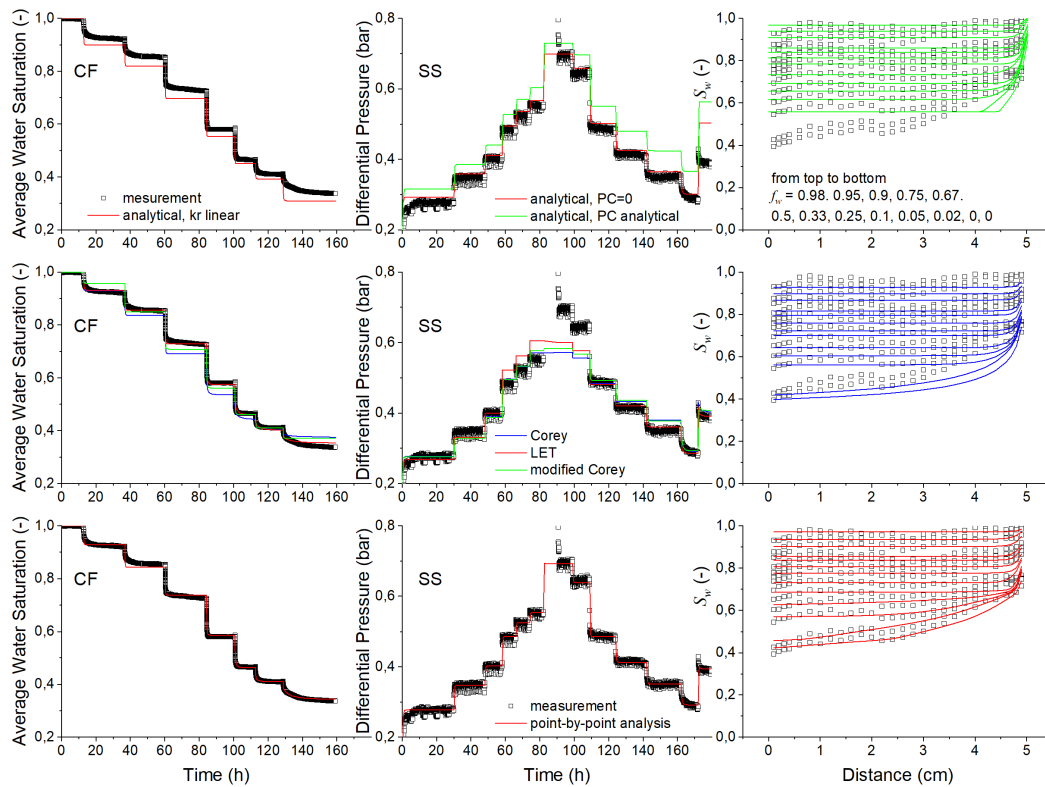
Figure 13 : Experimental data and analytical/numerical interpretations: CF average water saturation (left), SS differential pressure (middle), and SS saturation profiles (right). Top row: forward simulations using the analytical solutions. Middle row: automated and simultaneous history march using different $k_r(S_w)$ power-law input functions in combination with their corresponding $p_C(S_w)$ representations. Lower row: best match using the point-by-point approach.

3.3.1 Finding Solutions

The analytical solutions using Darcy's law for SS and the Hassler–Brunner equations for CF experiments are shown in Figure 14 and are used as starting points for the numerical simulations. The quality of the analytical solutions is demonstrated by forward simulations and comparison of the results to the experimental data, as shown in the top row of Figure 13. The comparison of the SS differential pressure shows a reasonable match as capillary pressure is ignored. Including the Hassler–Brunner analytical solution in the forward simulation of the SS

experiment, the data are no longer matched but rather an overestimation of the differential pressure. The Hassler–Brunner analytical solution itself underestimates the average water saturation of the CF experiment. The observed mismatches emphasize the importance of including both data sets in the analysis and even the importance of simultaneous history matching of $k_r(S_w)$ and $p_C(S_w)$, matching SS and CF experiments simultaneously.

At first, we simultaneously matched CF (average water saturations) and SS (pressure and saturation profiles) experimental measurements by using various power-law representations for $k_r(S_w)$, namely, Corey, LET and modified Corey, and the corresponding representations of $p_C(S_w)$. Since the data set refers to a primary drainage process, the water endpoint relative permeability is fixed to $k_{rw}(S_w = 1) = 1$. All the other parameters are left open. The residual water saturation is, however, a history matching parameter common for both $k_r(S_w)$ and $p_C(S_w)$ but matched separately from each other. This means that S_{wc} can principally be different for both types of data sets. The starting point of the history match is the analytical solution shown in Figure 14.
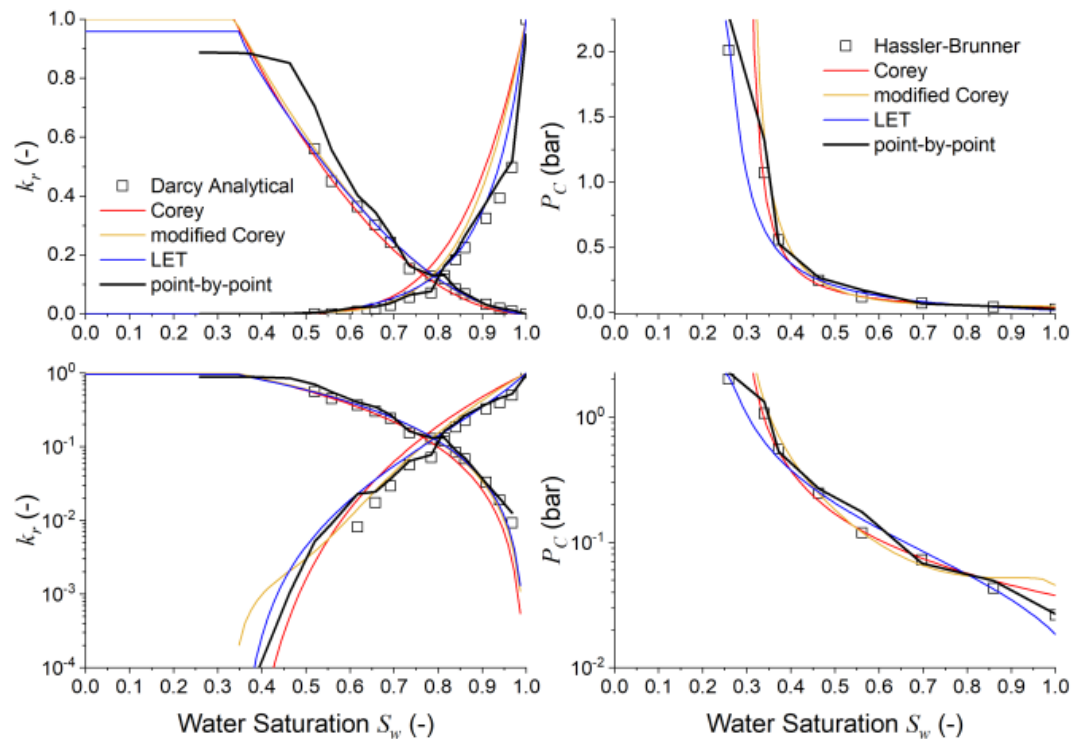
Figure 14 : Analytical solutions (symbols) and results of the history matching using various representations of $k_r(S_w)$ and $p_C(S_w)$, as indicated in the legends. Top: saturation functions on a linear scale. Bottom: the same functions on a logarithmic scale.

As shown in Figure 13, none of these models suitably describe the experimental data sets. Referring to the SS differential pressure, the deviation is strongest close to the crossing points

of relative permeability, where the total fluid mobility is lowest, i.e., highest differential pressure values. However, referring to the combined data set of SS and CF, the overall deviations are unacceptable.

With the point-by-point HM approach, we give the system much more degrees of freedom. In this approach we used 17 points for water relative permeability, 17 for oil relative permeability and 8 points for the capillary pressure table. The points for the relative permeability tables are coming from the average of the saturation profiles at each fractional flow until the minimum water saturation measured in the SS experiment. Below this water saturation we get the points from average water saturations of the CF experiment. For the capillary pressure table, we get the points from the average water saturation of the CF experiment. Here we only vary the functional values, and the saturation values are constant. The lower row of Figure 13 shows the resulting simulated versus experimental responses. With point-by-point matching, the $k_r(S_w)$ and $p_c(S_w)$ line shapes are not restricted to follow a certain functionality, and with this, complex rock structures may be described. In the present case of Estaillades limestone, all responses can be well described, including the SS saturation profiles for all $f_w(S_w)$. The resulting $k_r(S_w)$ and $p_c(S_w)$ are shown in Figure 14, in which all solutions are compared. The point-by-point approach delivers rather unregularly shaped saturation functions but closely follows the irregularities directly observed in the experimental responses. Furthermore, all resulting saturation functions from the HM of the experimental measurements with the simulation predictions are within rather narrow intervals, which is surprising, considering the quality of the matched versus experimental responses. This opens the important question about the uncertainty in the procedure and finally the resulting uncertainty in the saturation functions.

The results of the HM simulations depend on the optimization algorithm being used and for the point-by-point approach presented here we found the active-set algorithm in MATLAB *fmincon* function to be the most efficient. The Levenberg-Marqardt (LM) method which is used in the literature (Berg et al., 2021a; Maas et al., 2019) does not allow the implementation of inequalities (equation (5)) which is an integral part of the point-by-point approach to force the monotonic behavior for the saturation functions. Other algorithms e.g., interior-point can sometimes lead to a closer match to the experimental measurements in case power law representation for saturation functions are used.

3.3.2 Uncertainty Analysis

To quantify the uncertainties, we run Monte Carlo simulations using ParaMonte. We specify a chain size of 20,000, which is the number of unique points to be sampled from the likelihood estimation function. For this case it leads to ~1,5 million total likelihood estimation function

calls or ~1.5% acceptance rate for the MCMC algorithm. Considering the high-dimensional parameter space, the uncertainty analysis requires a large computational effort resulting in approximately a week of computational time on the used computer system. Figure 15 top shows the value of the likelihood estimation function, which reduces in the early iterations and then oscillates around a value of -15. The adaptation measure is a real number between 0 and 1 with 0 implying no proposal adaptation and 1 implying extreme adaptation. The convergence of the adaptive Markov chain – the type of MCMC simulations that we are using in this study - to the target density is guaranteed, as long as the adaptation of the Markov chain monotonically decreases throughout the simulation. It is, therefore, important to monitor the amount of adaptation in ParaDRAM simulations to ensure the adaptation of the proposal distribution diminishes progressively throughout the simulation (Shahmoradi and Bagheri, 2020). This value is shown in Figure 15 bottom and the moving average is shown to be monotonically decreasing. This is a healthy sign for the implemented Monte Carlo simulation, which shows a convergence in both the sampled likelihood estimation function and input parameters (Shahmoradi and Bagheri, 2020). For the samples used in this study the point-by-point approach showed the best convergence and match with experimental data whereas; the power-law-like saturation functions do not well match the experimental data, which leads to convergence problems of the Monte Carlo simulation. In that case, the tracer chains overshoot to high values, making the uncertainty range larger. This behavior is sample specific, and the saturation functions can be predicted using power law function with a high confidence level as shown in the literature (Maas et al., 2019).

Figure 16 shows the histograms of the simulated k_{ro} (a), k_{rw} (b), and p_C (c) points along the water saturation axis. These histograms can be used to quantify the uncertainty, which may be defined by calculating the P10 to P90 interval given in Figure 17. The interval refers to the probability of 10 to 90% that the quantity—in this case the fluid relative permeability—exceeds the given value. The P50, given in the same panel, refers to a best match from the Monte Carlo approach. In addition, Figure 16 shows the MCMC chain plots (the accepted Markov chain) at selected saturations along with the correlations between neighboring saturation points exemplarily for k_{ro}. The histograms and the MC line tracers show nearly Gaussian distributions except for the endpoint at connate water saturation. This means that the modeled drainage process is less sensitive to the endpoint, reflected in the elongated histogram shape. This leads to the large uncertainty range at the tail of the water relative permeability in Figure 17 (a). The same is true for the capillary pressure (c), as the centrifuge multistep simulation is less sensitive to the capillary pressure at residual water saturation, leading to a larger uncertainty at S_{wc}.
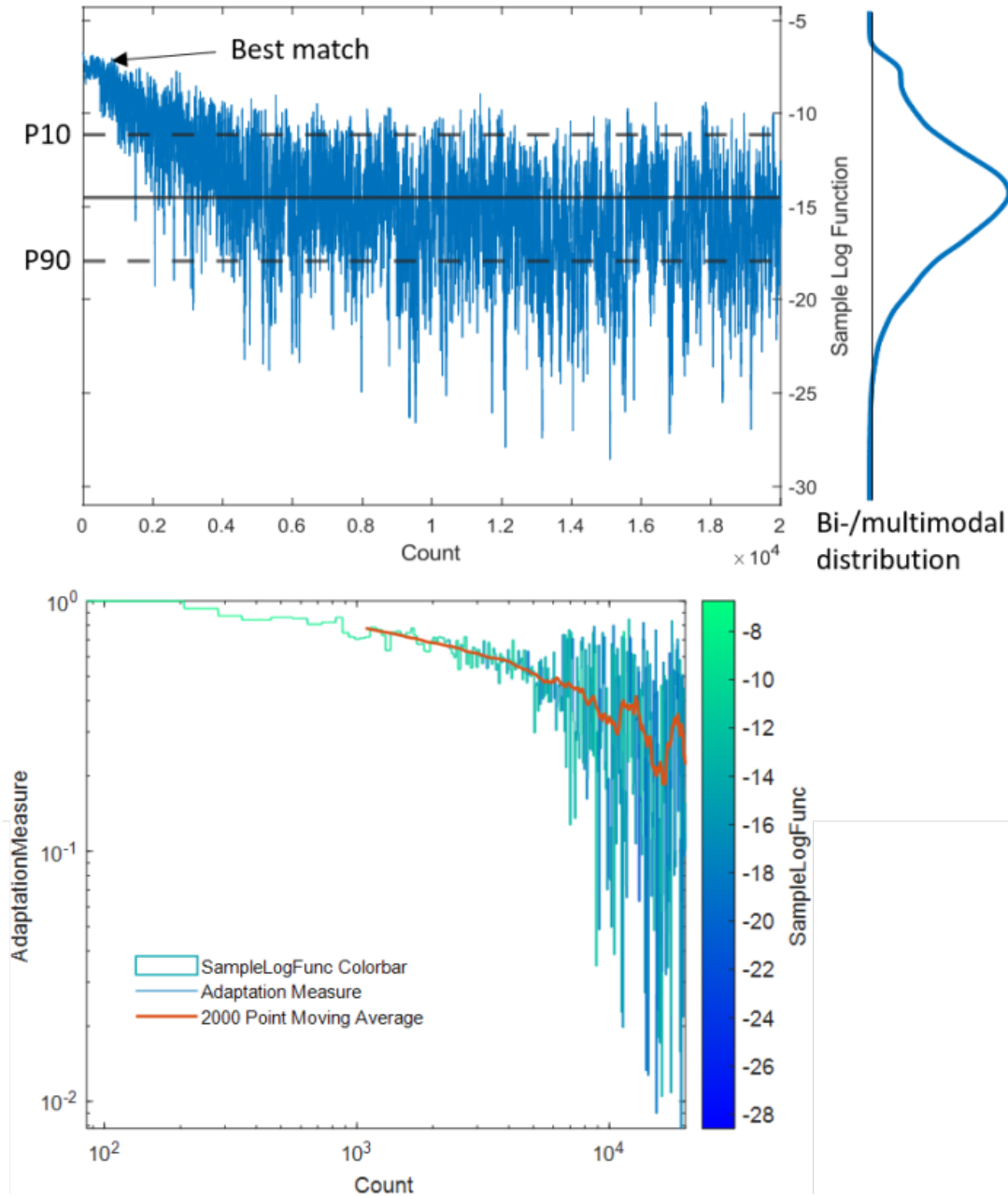
Figure 15: Top: the value of the sampled likelihood estimation function (equation (6)) during the MCMC for the accepted chain of samples. Bottom: the adaptation measure for the full Markov chain.

Although the histograms mostly show Gaussian behavior, the tracer in some chain plots does not always oscillate around a constant value (e.g., $k_{ro}(S_w = 0.97)$). Longer period temporary deviations may be caused by the relatively large parameter space and the respective degrees of freedom, in which the values of some parameters can deviate from the general trend and still be accepted. However, then because of the increased error in the likelihood estimation function, the rejection rate increases, and the chain returns to the previous trend that it was following before.

Figure 17 shows all relative permeability and capillary pressure curves calculated for the Estaillades experimental data sets. It also shows the P10 and P90 range calculated from the earlier discussed data set referring to the histograms in Figure 16. The best history match lies within this range. However, it does not lie on the median of the interval. By performing a forward simulation of the experimental response in the boundary of the P10-to-P90 interval, the P10 and P90 pressure ranges are obtained, as shown in the inset of Figure 17(a). The measured pressure is well within the uncertainty range except around the highest-pressure points (lowest total fluid mobility) and around the pressure of the bump flood. These parts of the pressure plot are close to the boundaries of the calculated range.

The range here corresponds to the fixed relative error that we decided in the beginning before running the MCMC simulations. The resulting uncertainty range around the pressure is higher than the assigned 2.5%, since we also allocate 1% error to the saturation profile and 1% error to the average water saturation from the centrifuge experiment. Depending on the standard deviation of the experimental measurements, the error assigned to the measurements in the equation (6)) varies, which affects the calculated uncertainty range.
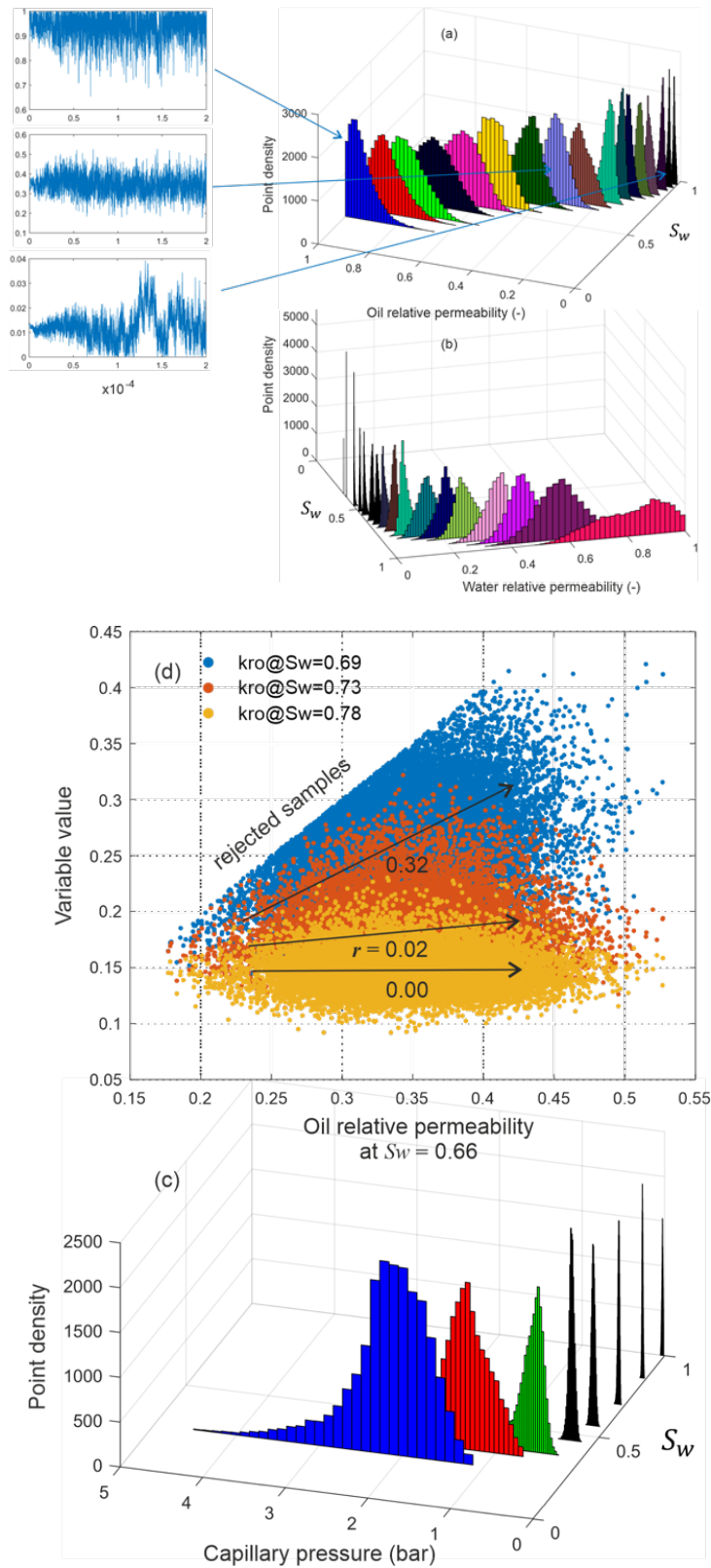
Figure 16: Histograms providing single parameter uncertainties of oil and water relative permeability, (a) and (b), respectively, and capillary pressure (c) saturation functions. MCMC chain plots are exemplarily given for oil relative permeability. (d) Correlation of oil relative permeability at the given water saturation with neighboring saturation points.

The reasoning behind this is intuitive since by doing so, we change the shape of the sampled response surface. The Pearson correlation matrix and the full grid plots for this analysis show the correlation strength between the history matched parameters. The map shows strong correlations between neighboring saturation points. This is partly caused by the forced monotonic behavior that we apply to our simulations. The relative permeability table shows positive correlation between the water saturation points next to each other (Figure 16 (d)) and this correlation is negative for the capillary pressure table. At lower water saturations, the positive correlation between k_r saturation points span several next neighbors, which is the reason for the larger uncertainty interval at low S_w. At higher water saturations, there is a negative correlation between the water and oil relative permeability. This means that at higher water saturations, the total mobility (relative permeability at constant viscosity) is split between oil and water; as phase mobility increases, the mobility of the complimentary phase decreases— a behavior that we physically expect.

Figure 16 (d) illustrates the correlation strength between k_{ro} at $S_w = 0.66$ and its neighboring points. The Pearson's correlation strength r is labeled in the plot below the black arrows. This demonstrates that with increasing water saturation, the correlation vanishes.
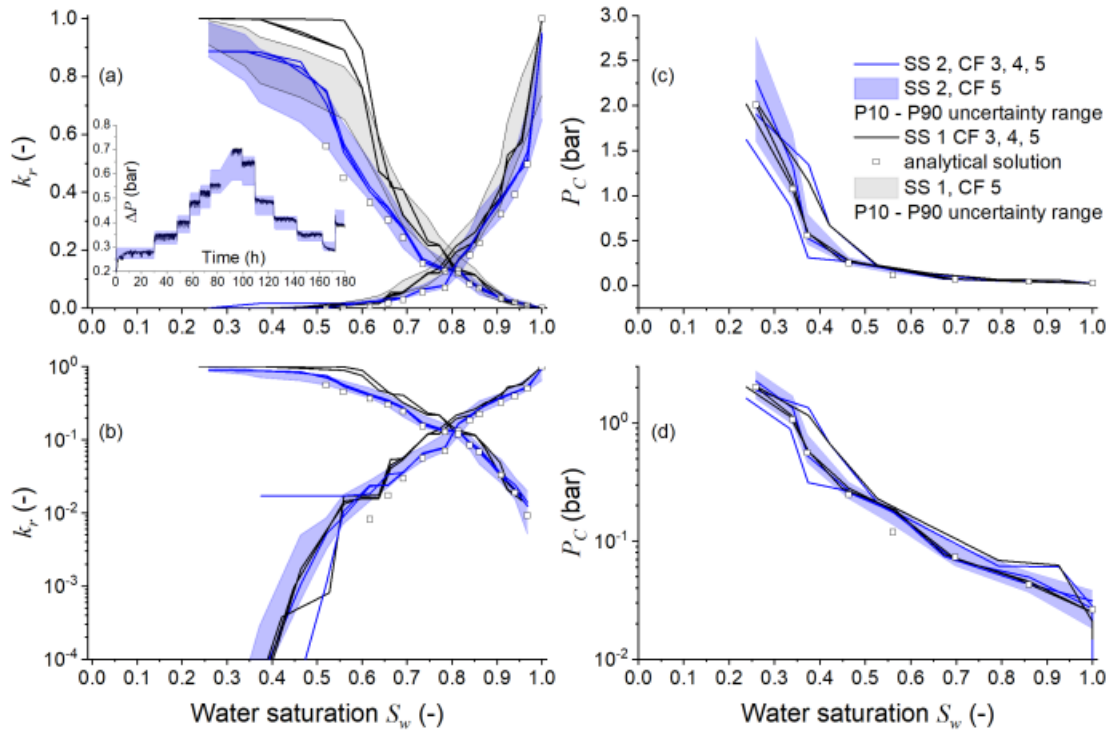
Figure 17: Panel (a) and (b): resulting relative permeability on a linear and logarithmic scale from experiment/sample SS 2 in combination with CF 2, 3 and 5. The uncertainty range is given for the combination SS2, CF 5. For comparison, the pair-wise analysis of SS1 with CF 3, 4 and 5 is given as well. Panel (c) and (d) provide the same information, but for the capillary pressure. The inset in (a) shows the P10 to P90 uncertainty interval for the differential pressure response during the SS 2 experiment as an example.

3.3.3 Sample-to-Sample Variation

It is a common problem that carbonates often show heterogeneity on various scales. In SCAL, we typically ignore heterogeneity on the plug scale, and SCAL data are numerically interpreted by assuming a simulation domain with homogeneous rock properties. However, sample-to-sample variations are common, even if the samples are drilled from locations close to each other. Therefore, it should be common practice to measure saturation functions on more than one plug from the region. In the present study on Estiallades, which is a common outcrop rock, the samples are from the same block and are therefore "twin plugs". A natural question is whether measurements on twin plugs deliver results within the uncertainty range of the individual data set. (Maas et al., 2019) proposed a method to deal with the common data interpretation problems that rises from the heterogeneities of samples in SCAL experiments. They argued that by calculating the variability number (V) of the plugs using the X-Ray measurements one can decide on the significance of the heterogeneity based on the cut-off value for V. Their approach warrants further work to be looked into, also in the framework of the reliability of the analysis provided from a small number of samples, in the future.

What we deliver in this study is an indication only because 5 plugs (a common number of samples available for SCAL) and 2 and 3 repeat measurements may or may not provide a solid statistical basis (Maas et al., 2019). However, we use the two SS and the three CF experiments from (Ott et al., 2015) and simultaneously analyze all possible SS and CF combinations. The results are shown in Figure 17 (a) and (b) for relative permeability and (c) and (d) for capillary pressure. The simultaneous analysis shows a strong deviation between the SS results but a relatively small influence of the sample-to-sample variation in the CF experiments; the resulting curves split into two groups referring to the two SS experiments, which differ predominantly in the oil branch toward low water saturations, where the strongest point-to-point correlations are found as will be discussed further below.

With respect to uncertainty, for simulations with a given SS data set, the k_r curves generated by combining with the different CF data lie within a narrow window compatible with the individual uncertainty range from MCMC. However, the two groups do not fall into the individual uncertainty ranges but show a certain overlap over the whole saturation range. In this specific case, it appears that sample-to-sample variation plays a stronger role than the uncertainty coming from individual data sets and their combinations.

3.3.4 Bimodal Distributions

The samples from the likelihood estimation function shown at the top of Figure 15 show a rather multimodal histogram, indicating that there is no unique solution in the error surface. Figure 18 shows the histograms of $k_{ro}(S_w)$ for the SS 1/CF 5 case, where the best match lies partly outside the P10-P90 interval; in (c), the histograms are bimodal for water saturations below 0.6 and above 0.95, with a pronounced narrow maximum and an overlapping broad component. The global minimum is found using the MATLAB *fmincon* function—the best match, while the broad component dominates the uncertainty range in the MCMC sampling. Using equation (5) as the objective function in the *fmincon* function (without the -1/2 factor) leads to comparable results and trends when the *fmincon* function is used with equation (6) (see section 4.1), which excludes the influence of the specific choice of the objective function.

The complex bimodal histograms may be related to the following aspects: (a) At low S_w, the dataset is outside the range of the SS experiments. The information regarding k_r therefore comes exclusively from the centrifuge experiments. (b) Especially in the SS1 case, the HM result for k_{ro} is closely tied to 1 in this saturation range. If a monotonic behavior with $k_r \leq 1$ is required, most of the samples are rejected during HM in the respective range.
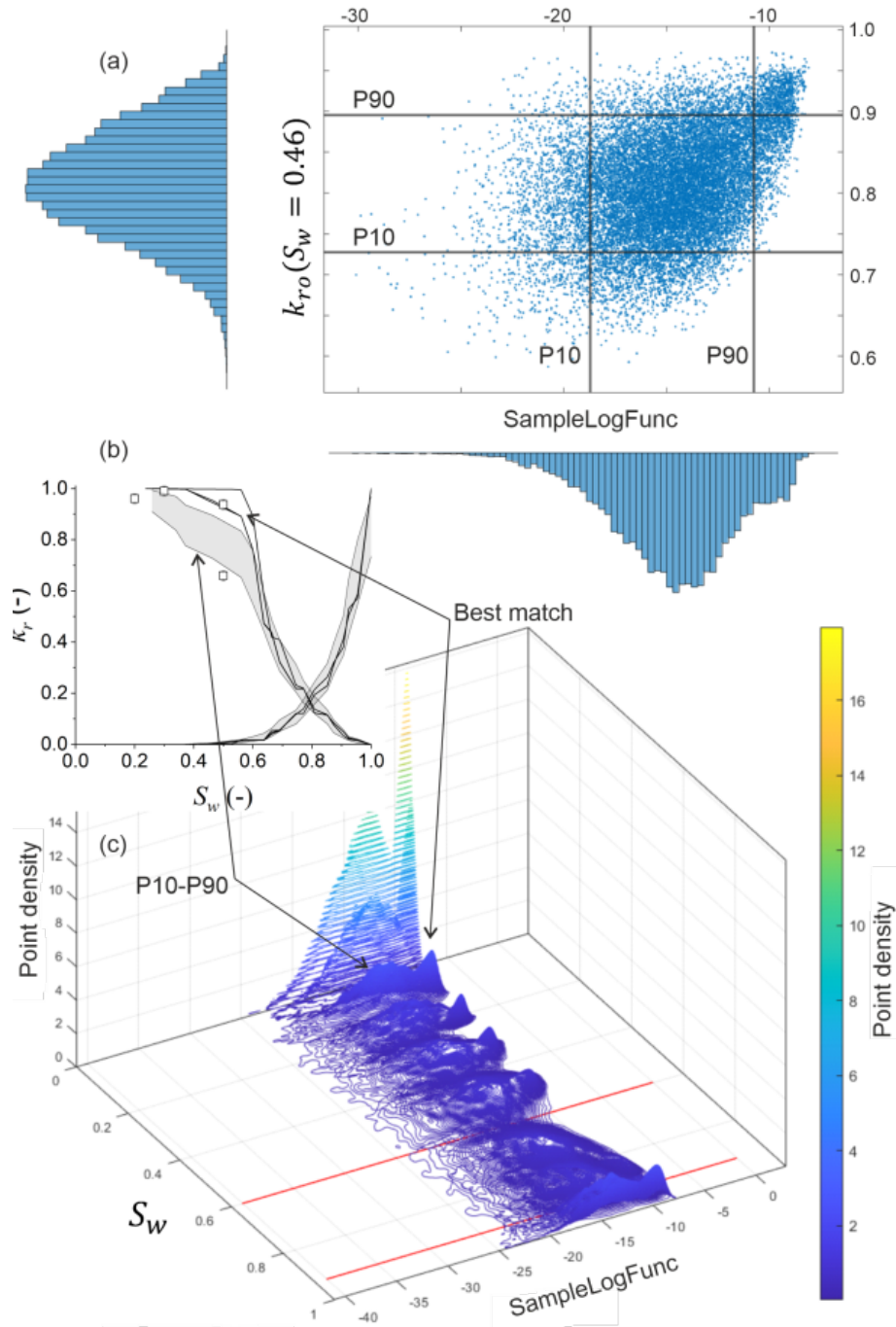
Figure 18: Sampled likelihood estimation function (equation (6)) versus oil relative permeability for the SS1 and CF5 combination. (a) for a single saturation state, $S_w = 0.46$; (c) for the full range of S_w. (b) Relative permeability and uncertainty interval from Figure 17 for comparison. The white symbols represent results from porous plate experiments, with errors of individual measurements in the order of the symbol size.

The symbols in Figure 18 (b) show the results of porous plate (PP) experiments (Ott et al., 2015). By means of the PP method, samples are desaturated to a certain water saturation close to S_{wc}. Subsequently, the effective permeability is measured by multi-rate decane flooding (at $f_w = 0$). Assuming that the aqueous phase is largely immobile, k_{ro} was derived. However, also

with the additional PP data, it is not possible to decide on the true k_{ro}. Due the sample-to-sample variation—considering that the PP experiments were performed on different samples—the derived k_{ro} values vary in the full spread of generated data.

3.3.5 Conclusions on SCAL Interpretations

In the present study, we present a comprehensive way to interpret SCAL data. We apply a workflow starting from the well-known analytical solutions, directly derived from the individual data sets, as input for numerical history matching. The experimental data sets are described simultaneously and by means of a point-by-point parameterization - 34 points for the two relative permeability tables combined and 8 points for the capillary pressure table. With these innovations, a good description of complex saturation functions is possible.

Different parametrizations of the saturation functions are used. The study shows that using classic power-law representations is not sufficient to conclusively analyze data derived from more complex rock types, such as microscopically heterogeneous carbonates. For this purpose, the point-by-point approach, in which the saturation functions were evaluated at the individual saturation points defined by the experimental steps that serve as HM parameters. This approach allows us to match complex rocks since the functions are not restricted to power laws.

Furthermore, the simultaneous evaluation of SS and CF experimental data sets accounts for the fact that k_r and p_C are coupled. The results show that simultaneous rather than subsequent evaluation of those data sets leads to more objective results. With "objective" we mean to prefer a solution without manual, respectively personal intervention in the process. However, the massive increase in the free parameters in the simultaneous point-by-point approach substantially increases the required computational power, especially in cases where uncertainty analyses are performed.

The uncertainties are evaluated by MCMC simulations sampling the response surface of the likelihood estimation function of the combined data set. This allows the extraction of single parameter distribution functions and correlations between those parameters on the saturation scale. The study shows that despite the given high degree of freedom, the simultaneous point-by-point approach delivers a very robust description of two-phase flow in complex rock types. While the gradient-based HM reliably finds the best match, MCMC sampling demonstrates the complexity of the response surface. This results in one SS data set for a separation of the best match and the P10-P90 uncertainty interval (the best match is within the P01-P99).

By combining all available SS and CF experimental results for analysis, a comparison of the sample-to-sample variation with respect to the error of the individual data set could be made. For the specific rock type, the sample-to-sample variation seems to be dominant (as far as the

limited data set allows for that statement). The results group around the individual SS curves with a narrow bandwidth by the various CF measurements. The P10-to-P90 uncertainty intervals of the two SS curves just marginally overlap apart from the saturation range around S_{wc}; the individual data sets also show the greatest uncertainty around S_{wc}, which may have to do with the missing next-neighbor information toward lower water saturations.

Chapter 4

Analysis of Displacements in Heterogeneous

This chapter is a reprint of (Amrollahinasab et al., 2024a; Omidreza Amrollahinasab et al., 2023) and the code for this chapter is available at (Amrollahinasab, 2024).

Rocks

Heterogeneity is ubiquitous in geological formations and can significantly impact multiphase fluid flow and therefore CO_2 plume migration. However, conventional SCAL workflows for determining key parameters like relative permeability do not account for sub-core scale heterogeneities. This chapter investigates the influence of heterogeneity on CO_2-brine displacement experiments through comparing SCAL interpretations to larger-scale tests assuming homogeneity and incorporating 1D and 3D heterogeneity models derived from CT imaging. The impact of rock heterogeneity on relative permeability is demonstrated via history matching and upscaling procedures, proposing a methodology to link core-scale observations with field-scale predictions. By extending traditional SCAL methods to include heterogeneity in carbonates, this work underscores the importance of adapting existing workflows to better capture the complexities inherent in such rock formations. Accurate prediction of fluid flow and two-phase displacements in subsurface reservoirs is essential for a range of applications, including hydrocarbon extraction and geological CO_2 storage. However, the unexpected migration of carbon dioxide in CO_2 injection operations highlights the need to improve our understanding of the underlying mechanisms, particularly in heterogeneous reservoirs (Aminu et al., 2017; Hosseini et al., 2013; Lu et al., 2013; Onoja and Shariatipour, 2019). Rock formations are typically heterogeneous on various scales. This poses a major challenge for the design and interpretation of measurements of multiphase flow properties, as the definition of a representative elementary volume (REV) depends not only on the scales of heterogeneity versus

the sample size but also on the nature of the measured property (Georgiadis et al., 2013; Hosseinzadeh Hejazi et al., 2019; Ringrose et al., 1993; Zhang et al., 2000). The dependency of capillary forces on heterogeneity results in a local variation in saturation states during immiscible displacements, referred to as 'capillary heterogeneity'. Conceptionally, this effect can be described through the spatial variability of the capillary-pressure saturation function (Chang and Yortsos, 1992). This phenomenon has practical consequences, as the measurement of multiphase flow parameters may depend on the measurement scale (Jackson et al., 2018; Kuo and Benson, 2015; Reynolds and Krevor, 2015). For example, rock heterogeneity at the submeter scale, such as laminations and bedding, can significantly impact fluid flow properties and must be considered to successfully model and predict fluid flow at larger scales (Berg et al., 2013; Jackson et al., 2018; Wenck et al., 2021). The effect can be particularly strong in multiscale heterogeneous carbonates and when significant viscosity contrasts are observed (e.g., CO_2-brine displacements).

Conventional reservoir simulation workflows naturally cannot explicitly represent the impact of small-scale heterogeneity on multiphase flow properties, such as relative permeability and capillary pressure characteristics (Egermann and Lenormand, 2005; Jackson and Krevor, 2020b; Renard and de Marsily, 1997). Relative permeability is a key parameter that controls the displacement and sweep efficiency in immiscible displacement. The main challenge in characterizing relative permeability is that laboratory and special core analysis (SCAL) measurements are usually performed on homogeneous samples that do not accurately represent the average property at the size of the discretization of a reservoir model. To illustrate this point, we can compare the size of a SCAL plug, which is on the order of centimeters, to a typical grid block in a reservoir simulation, which may be orders of magnitude larger. The information we have from the subsurface is scarce, and the understanding of the upscaling workflow from the homogeneous rock–fluid properties (SCAL) to the heterogeneous next scale is limited. Therefore, different approaches have been developed to characterize capillary heterogeneity within rock cores (Berg et al., 2013; Kong et al., 2015; Krause et al., 2013, 2011; Krause and Benson, 2015; Kuo et al., 2011; Ni et al., 2019; Pini and Benson, 2013a, 2013b; Reynolds et al., 2018), but uncertainty remains in characterizing more complex rocks typical of subsurface reservoirs across the fractional flow curve and for different flow rates (Berg et al., 2021a, 2021b).

Multiscale workflow from the micron (pore) scale to the meter scale, offer new opportunities to systematically upscale multiphase flow for reservoir application purposes (Kurotori and Pini, 2021). These workflows combine laboratory-based characterization techniques, such as core flooding with in situ imaging methods on various scales and digital rock physics, with upscaling schemes that account for capillary pressure heterogeneity. With rigorous upscaling, small-scale

effects can be incorporated into continuum-scale models when interpreted by numerical modeling using an optimization routine; effective petrophysical parameters and relative permeability saturation functions can be calculated, including their uncertainties (Omidreza Amrollahinasab et al., 2023; Burmester et al., 2022; Hosseinzadeh Hejazi et al., 2019; Kurotori and Pini, 2021; Pini and Benson, 2013a; Ruspini et al., 2021). However, implementing sample heterogeneity for interpretation of relative permeability refers to a downscaling rather than an upscaling as long as the heterogeneity is not represented in a grid block of a reservoir model.

A well-studied candidate rock sample with a high degree of heterogeneity is Estaillades limestone. Studies have shown that relative permeability saturation functions derived from classical SCAL experiments do not adequately represent the behavior of larger rock volumes that are 12 times the volume of the samples typically used in SCAL studies, particularly when these volumes encompass 3-inch diameter cores (Ott et al., 2015).

In the previous chapter (Omidreza Amrollahinasab et al., 2023), we developed a comprehensive stochastic SCAL analysis workflow and applied it to steady-state and centrifuge experimental data on decane-brine primary drainage in Estaillades. The analysis yielded confidence intervals of combined measurements and sample-to-sample variations.

In the present chapter, building upon our previous work (Omidreza Amrollahinasab et al., 2023), we perform two key investigations depicted in Figure 19:

a. We conduct a comparative analysis between full stochastic interpretations of SCAL data (steady state and centrifuge) and larger-scale unsteady state (USS) core flood experiments using 1D homogeneous simulation domains. By presuming homogeneity – which is traditionally the case for SCAL data interpretation (McPhee et al., 2015a) - the analysis of the USS experiment yields the upscaled $K_r(S_w)$, inclusive of the confidence interval.

b. We incorporate the 3D porosity profile as determined by X-ray computed tomography (CT) and the resulting permeability and capillary heterogeneity. By history matching the USS experiment on the 3D heterogeneous domain, we aim to determine the true $K_r(S_w)$ and shed light on the impact of heterogeneity on the investigated scale.
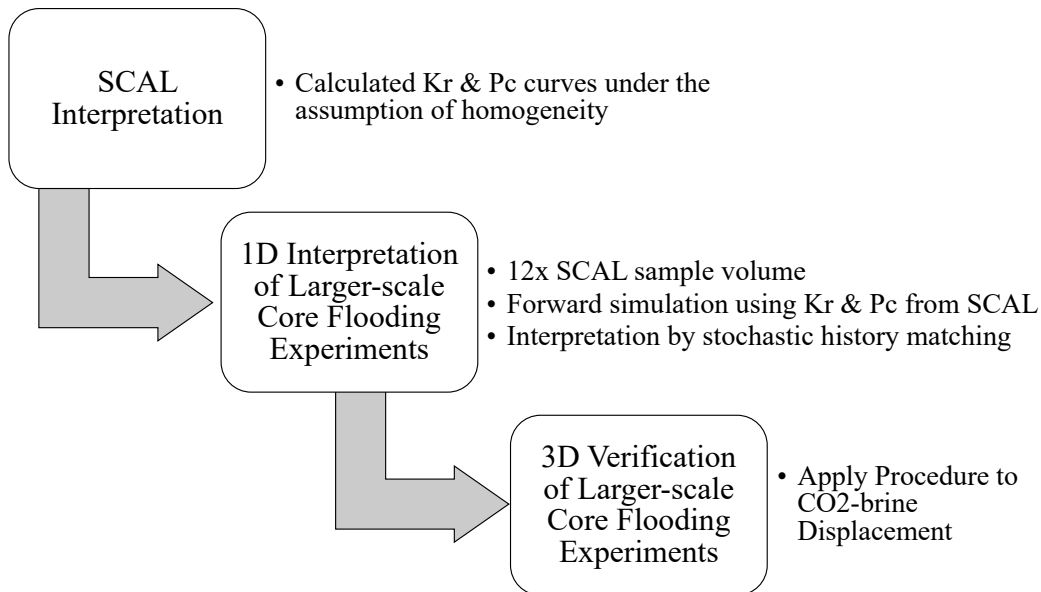
Figure 19: Workflow of the study. This diagram illustrates the progressive approach taken in this research, starting from the homogeneous analysis through to the 3D heterogeneous simulation. It depicts the distinct steps and methodologies employed at each stage, underlining the complex interplay between experimental work, numerical interpretation, and the investigation of heterogeneity effects on relative permeability saturation functions.

These investigations are intended to delineate the influence of rock heterogeneity on relative permeability measures and capillary pressure, thereby improving our understanding and predictive capability of CO_2-brine displacement in heterogeneous carbonate rocks.

To study the effect of heterogeneity on relative permeability, we analyze decane-brine and CO_2-brine unsteady-state experiments. The first serves as a water-wet reference case that directly refers to the earlier steady-state measurements, and the second is the system under investigation. Heterogeneity is introduced step by step in the simulations by first considering a 1D homogeneous simulation domain, then a 1D heterogeneous domain, and finally the actual 3D heterogeneous domain. For 1D homogeneous cases, a full stochastic analysis is feasible and thus, carried out. For the 1D heterogeneous domain, simple history matching is performed to derive the base case $k_r(S_w)$, which is also used for the 3D simulations, considering the full set of experimental saturation data. By progressively increasing the complexity of the fluid pairs and simulation domains, we ensure that the approach is robust and applicable to a wide range of scenarios. This methodology will provide valuable insights into the validity and limitations of the current SCAL procedures and pave the way for the development of alternative methods and upscaling workflows for calculating saturation functions.

4.1   Interpretation Assuming Homogeneity

A key assumption in classical SCAL interpretation is that the samples are considered homogeneous, resulting in a simple 1D homogenous simulation domain. This assumption requires careful sample selection and reasonably small samples with a volume that can be considered a representative elementary volume (REV). The data once interpreted are therefore single sets of relative permeability and capillary pressure saturation functions that do not need further interpretation. In reservoir simulations, such $k_r(S_w)$ and $P_c(S_w)$ saturation functions are typically assigned to rock types with heterogeneity being accounted for by a Laverett-J scaling of the $P_c(S_w)$ (Leverett, 1941). In any case, in a single grid block, only one $k_r(S_w)$ and $P_c(S_w)$ saturation function is assigned, implicitly considering the grid block as homogeneous.

Compared to small-scale SCAL experiments, larger-scale core flooding is typically affected by the size and heterogeneity of the sample, and sweep effects are observed (Berg et al., 2013; Ott et al., 2015). Now, there are two options for numerically interpreting the data: (a) introducing rock heterogeneity of various properties into the simulation model, resulting in "true" saturation functions, and (b) ignoring rock heterogeneity, i.e., considering the rock domain as homogeneous and representative. In the latter scenario, where rock heterogeneity is ignored, we do not anticipate obtaining the same relative permeability. Instead, we expect to derive an effective $k_r(S_w)$ that accurately represents the investigated volume, a value we consider the upscaled $k_r(S_w)$. This upscaled value, however, might still be influenced by the scale of the investigation.

In our initial step, we use a 1D-homogenous SCAL approach to extract the relative permeability from the larger-scale USS experiments. To achieve this, we first simulate the displacement process, utilizing the 'true' SCAL saturation functions applicable to the same rock type, as per (Omidreza Amrollahinasab et al., 2023). Subsequently, we perform a history match of the experimental data to determine $k_r(S_w)$, using $P_c(S_w)$ derived from MICP, data that is usually available for standard core analysis. To apply the MICP curve to primary drainage, we perform a scaling operation based on the interfacial tension (IFT) as follows:

$$P_c(\sigma) = \frac{\sigma \cos\theta}{\sigma_{ref} \cos\theta_{ref}} \, p_{c,ref}, \tag{21}$$

where σ_{ref} is the mercury-air IFT (480 mN/m) , θ_{ref} is the corresponding contact angle of (140 degrees assumed for both fluid pairs (θ for CO_2-brine)), and σ is the IFT of the decane- and CO_2-brine systems, which is assigned 45 mN/m and 40 mN/m (Georgiadis et al., 2010), respectively. Furthermore, we apply the closure correction to MICP based on the methodology presented by (McPhee et al., 2015b). The pressure drop and the production data were then matched by varying $k_r(S_w)$. The MICP-scaled $P_c(S_w)$ for decane-brine, in comparison with

the data derived from SCAL measurements, is examined in (Omidreza Amrollahinasab et al., 2023). This is depicted in Figure 21 (c) and (f) for both decane-brine and CO_2-brine systems. Except for the entry pressure, the scaled MICP curve falls well within the uncertainty range of the SCAL data.

The SCAL interpreted $k_r(S_w)$ and $P_c(S_w)$ from (Omidreza Amrollahinasab et al., 2023) can now be directly compared to the decane-brine USS flooding experiments since both refer to the same rock-fluid system. There is a large deviation between the predicted and observed results; the pressure drop and the brine production curve are strongly underestimated, as indicated in Figure 20 (a) and (b) – the SCAL data are not directly applicable to the investigated scale.

A good match can be achieved by history matching the experimental data. For this, $k_r(S_w)$ is parametrized using the two commonly used representations, namely, Corey (R. H. Brooks and A. T. Corey, 1964) and LET (Lomeland et al., 2005). Since the experimental process is primary drainage, the residual decane saturation and the respective endpoints were fixed to $S_w = 1$ an $k_{rw}(S_w = 1) = 1$ using Corey, and all other parameters of $k_r(S_w)$ were open for matching. The matched experimental pressure drop, production curve and saturation profiles are shown in the top row of Figure 20 Even if the saturation profiles simulated on a homogeneous domain cannot reflect the experimental profiles, ΔP and the cumulative brine production are matched well with some deviations in the transient part and specifically at the breakthrough point.

The LET parametrization is used as a second attempt to match the experimental measurements using a 1D homogeneous model, which offers greater flexibility at the expense of more fitting parameters. For uncertainty analysis, we used MCMC simulations, the same methodology as applied to the SCAL experiments in (Omidreza Amrollahinasab et al., 2023). Note that in the present case, $P_c(S_w)$ is kept constant to the scaled MICP mentioned before.

The history match results and the quantified uncertainty ranges are shown in Figure 21, along with the best match from the SCAL interpretation in Figure 21 (a) and (b). The LET matches the experimental data perfectly. In comparison to the SCAL reference data, however, Corey $k_r(S_w)$ generally shows a lower mobility of both phases, while LET shows a crossover with higher mobilities at high phase saturations and lower mobility at lower phase saturations. In any case, the differences between SCAL and the larger scale homogeneous interpretations are not subtle but substantially out of the given confidence interval of the SCAL data (Omidreza Amrollahinasab et al., 2023) and the USS data given for the LET parametrization. The saturation profiles show a poor match as expected; specifically, a homogenous simulation domain cannot represent a heterogeneous rock sample, but the brine production curve's overall material balance is met.
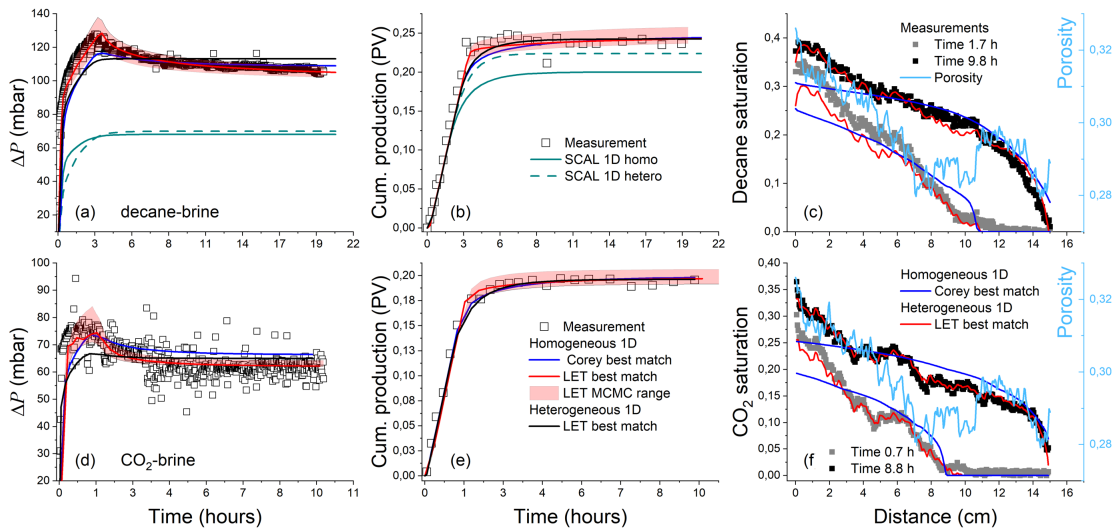
Figure 20: Comparative Analysis of Experimental and Numerical Interpretations of Decane-Brine and CO₂-Brine Displacement Tests in Homogeneous Domains. This figure presents the comparison between experimental outcomes (depicted by symbols) and their corresponding numerical interpretations for both decane-brine (upper row) and CO₂-brine (lower row) displacement tests. From left to right, the panels show: (a) the pressure differential, (b) the brine production curve over time, and (c) the decane and CO₂ saturation profiles at two distinct time intervals as indicated in the legend. The solid lines in each graph represent the 1D numerical history-matching outcomes using homogeneous and heterogeneous simulation domains based on the CT density profile (represented by the light blue line). The models used for the relative permeability calculations and their respective uncertainty intervals are highlighted in the legend and elaborated upon in the main text. Consistent coloring and symbols are utilized across all figures to enhance comprehension. For example, the blue line labelled 'Corey best match' in figure (e) retains the same meaning in all related figures.
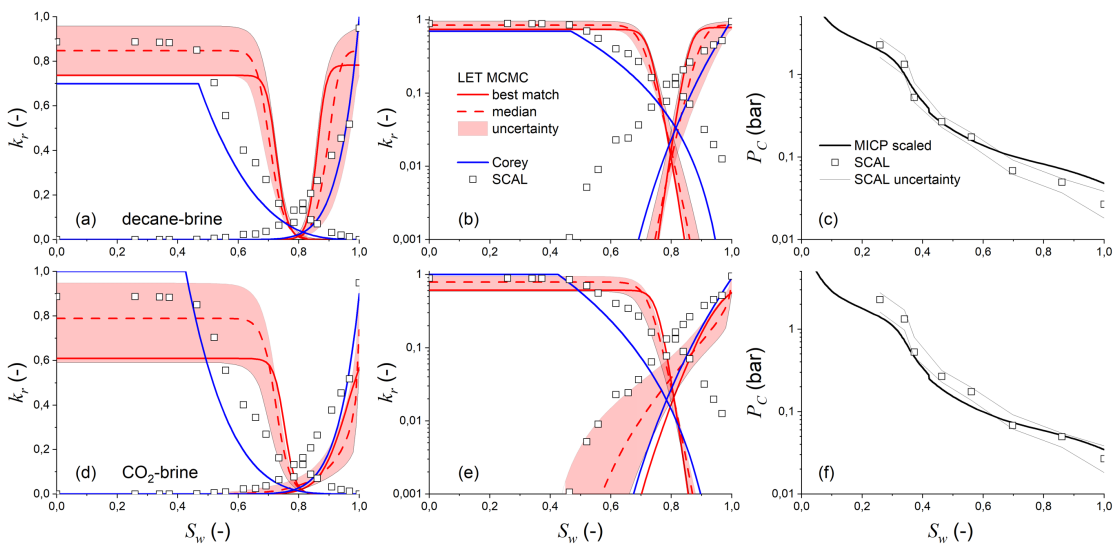
Figure 21: Comparative Analysis of Relative Permeability and Capillary Pressure Saturation Functions in Decane-Brine and CO₂-Brine Displacement Experiments in Homogeneous Domains. This figure shows the results of history matching performed on 1D homogenous and 1D heterogeneous simulation

domains, utilizing capillary pressure functions (shown on the right) as input. The top panels (a) to (c) represent the history matching (HM) results for the decane-brine experiments, while the lower panels (d) to (f) showcase the results from the CO₂-brine displacement experiments. From left to right, each panel depicts: relative permeability k_r presented in both linear and logarithmic scales, and capillary pressure P_c on a logarithmic scale. The squares in each panel correspond to SCAL results, which are measured on a smaller, homogenous scale. Consistent symbols and colors are used throughout the figure to ensure ease of understanding and coherence.

The same procedure was applied to the CO_2-brine displacement experiment, as shown in the lower row in Figure 8 and Figure 20. Additionally, here, we applied a homogeneous 1D simulation domain and Corey and LET parametrization of the relative permeability to be matched. The MICP curve was scaled in the same way with an IFT of 40 mN/m and a contact angle of 140 as representative of the CO_2-Brine fluid pair (Leverett, 1941).

By history matching, good matches similar to the decane-brine case could be achieved with the advantage of the LET model. The data are shown in Figure 20 (d) and (e). The MCMC confidence interval (P10 to P90) covers the experimental data points well. The respective saturation profiles for two subsequent time steps are shown in Figure 20 (f). Again, the complexity of the experimental saturation profile cannot be matched, but the material balance is honored.

The resulting $k_r(S_w)$ values are shown in Figure 21 (d) and (e). Compared to the decane-brine system, the relative CO_2-brine permeability shows a significant difference in water mobility, which is initially smaller but decreases significantly less with increasing CO_2 saturation than in the reference system. Furthermore, compared to the reference case, the uncertainty from the MCMC analysis (P10 to P90) is significantly lower for the brine relative permeability but higher for the CO_2 phase.

From these observations, we conclude that (a) HM complex experimental data with a 1D homogeneous simulation domain allow a perfect description of the experimental ΔP and the brine production curve using a flexible $k_r(S_w)$ parametrization. (b) The simulated saturation profiles S_w do not match the complex experimental profiles but match the material balance as a result of the assumed homogeneity. (c) By assuming homogeneity, $k_r(S_w)$ represents the average sample volume and may therefore be considered upscaled.
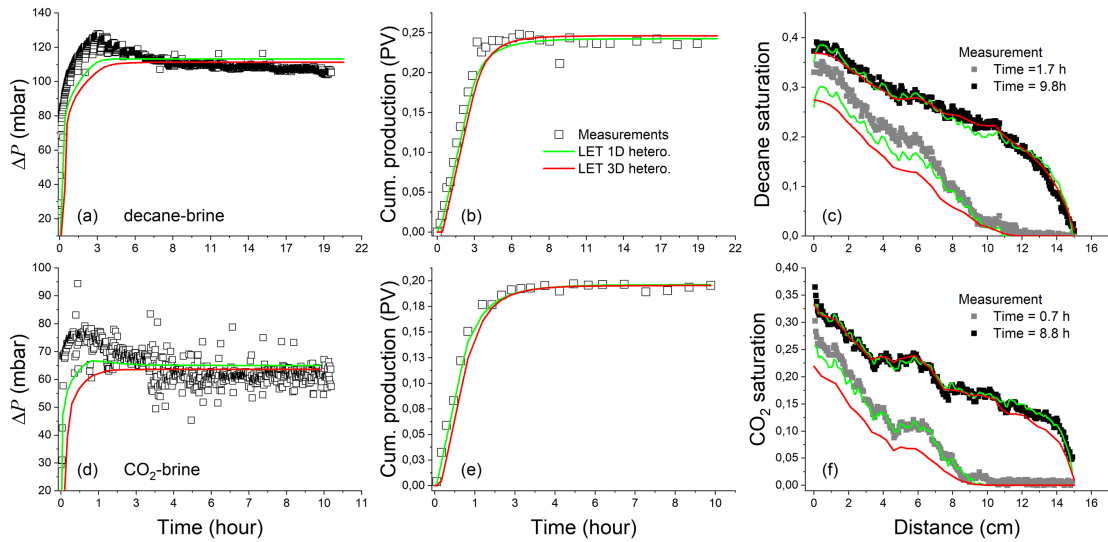
Figure 22: *Comparative Analysis of Experimental and Numerical Results in Decane-Brine and CO2-Brine Displacement Experiments Considering Heterogeneity. The top and bottom rows represent the experimental responses (indicated by symbols) for decane-brine and CO2-brine displacement experiments, respectively, and their corresponding numerical interpretation similar to Figure 20 From left to right, each panel depicts: the pressure difference and brine production curves over time, and saturation profiles for decane and CO2 at two subsequent time steps as specified in the legend. The lines in each panel represent the results from the numerical history-matching process utilizing a 1D heterogeneous domain derived from the CT density profile and the full 3D heterogeneous volume. The employed relative permeability models are indicated in the legend and discussed in detail in the main text. This figure demonstrates the integration of heterogeneity in modeling the displacement experiments.*
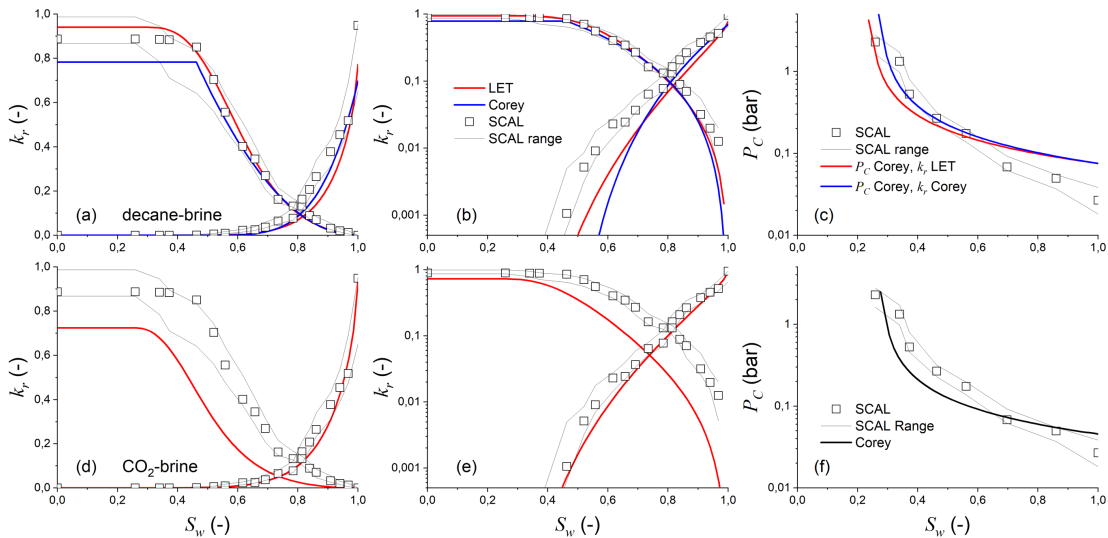
Figure 23: *Comparative Visualization of Relative Permeability and Capillary Pressure Saturation Functions in Heterogeneous Domains. This figure showcases the outcomes of history matching processes applied on the 1D and 3D heterogeneous simulation domains, derived from decane-brine and CO2-brine displacement experiments. The top row panels (a) to (c) exhibit the history-matching results for the decane-brine experiments, whereas the bottom row panels (d) to (f) represent the outcomes for the CO2-*

brine displacement experiments. Each set of panels, from left to right, display: relative permeability k_r on both linear and logarithmic scales, and capillary pressure P_c on a logarithmic scale. The squares in each graph correspond to the SCAL results that were obtained from measurements on a smaller scale deemed as homogeneous. This figure aids in contrasting and understanding the impact of heterogeneity on relative permeability and capillary pressure functions.

4.1.1   Interpretation Considering the 1D Porosity Profile

With the above discussed model, we implement porosity, permeability and capillary heterogeneity in the 1D simulation domain. The match of a forward simulation using the SCAL interpreted $k_r(S_w)$ and $P_c(S_w)$ (Omidreza Amrollahinasab et al., 2023) is shown in Figure 20 (a) and (b). It shows that, even when the simulations are performed on the heterogeneous modeling domain, the $k_r(S_w)$ and $P_c(S_w)$ interpretation from SCAL lead to large deviations in ΔP, the brine production is underestimated and the saturation profiles cannot be matched.

The history match of the experimental responses for decane-brine (top row) and CO_2-brine (bottom row) are shown in Figure 22. By including the exact porosity profile, more experimental data have to be described with only a few additional parameters, such as the scaling factor. This is at the expense of the quality of the agreement of the numerical interpretation with the experimental data, as shown in Figure 22. The saturation profiles and the brine production curve are now satisfactorily described. However, the pressure difference ΔP shows that the transient part around the breakthrough time cannot be described exactly, which is also visible in the agreement with the other experimental responses.

The resulting Corey and LET $k_r(S_w)$ and Brooks-Corey $P_c(S_w)$ are shown together with the SCAL interpretations in Figure 23; including the heterogeneity in the simulations causes the resulting $k_r(S_w)$ to come ultimately close to the uncertainty range predicted from the SCAL interpretation by (Omidreza Amrollahinasab et al., 2023). By "ultimately close" we mean that our model predictions closely align with the observed experimental data, indicating a high level of accuracy in our simulations. The predicted brine $k_r(S_w)$ for both fluid pairs is just at the lower boundary of the uncertainty range, but the decane $k_r(S_w)$ is well inside the uncertainty interval. The largest deviation shows the calculated CO_2 k_r, which is substantially lower than the SCAL predictions. However, the SCAL experiments refer to the decane-brine system rather than to CO_2-brine and may be caused by different wetting properties.

The good agreement of the simulation and experiment demonstrates the following: (a) the methodology developed by (Hosseinzadeh Hejazi et al., 2019) is applicable to a single-rate USS drainage experiment, and (b) including the heterogeneity results in $k_r(S_w)$ saturation functions that come close to the formerly called "true" $k_r(S_w)$, as obtained from classical SCAL experiments. However, as the comparison with the homogeneous simulations shows, this "true"

$k_r(S_w)$ is just meaningful if the heterogeneity is explicitly described. It is imperative to understand that the significance lies in the interpretation of experimental data, which must be contextualized and explained within the framework of the studied phenomena.

The calculations of the scaling factors and Pareto fronts from the optimization method used show a linear trend between the error from production and the error from the saturation profile. This addresses the inconsistency observed in the homogeneous simulations and confirms the need for heterogeneous simulations for the EST core plug.

4.2   3D Heterogeneous Modeling

The methodology of capillary pressure scaling can be extended from 1D to 3D simulation domains (Kurotori and Pini, 2021); the principle of calculating the scaling factor is the same as that for 1D but is calculated on the 3D grid. Because of the computational demand, it is not possible to history match the experimental data in 3D since each simulation usually takes around four hours. Instead, we forward simulate the displacements using the best match – the LET $k_r(S_w)$ case – obtained from the 1D heterogeneous model and statistically compare the simulated and experimental responses on fluid saturation. The benchmark of 3D simulations compared to the 1D simulations and the sensitivity to different layering systems are demonstrated in Appendix C.

The measured and predicted saturation distributions are shown in Figure 24 (a) and (b) for the decane-brine and (e) and (f) for CO_2-brine displacement. For better comparison, the 1D projection, i.e., the resulting 1D saturation profiles, are plotted in Figure 22 (c) and (f) together with the experimental and 1D-derived saturation profiles. The match of the 3D results to the 1D and experimental projected saturation profiles is reasonable, considering that it is not the result of a history match but a forward simulation. The ΔP and the cumulative brine production are comparable to the responses of the 1D heterogeneous results with the same limitations around the breakthrough time, as discussed previously. This may be a limitation of the capillary pressure scaling method, as one of the underlying assumptions of the methodology is that the system is in a steady state (Hosseinzadeh Hejazi et al., 2019; Pini et al., 2012).

To better quantify the saturation profile, Figure 24 (c) to (h) shows a statistical comparison of the experimentally determined and numerically simulated 3D saturation profiles presented in Figure 24 (a) and (b). (c) and (g) show the respective histograms for the decane-brine saturation state after 9.8 h and the CO_2-brine saturation state after 8.8 h of flooding. The data show a perfect match over a wide saturation range, which is further quantified in the respective correlation plots (d) and (h), which are obtained by plotting the simulated saturation of each grid block versus the experimentally measured saturation. The data show a high degree of

correlation with correlation coefficients above 0.99 and 0.98 for the decane and CO_2 cases, respectively. Deviations in the experimentally and numerically derived histograms and hence in the correlations are predominantly at high-brine phase saturations, where the experimental data show saturations above one, which is an error in the measurements. However, the affected range is not relevant for fluid displacement physics.
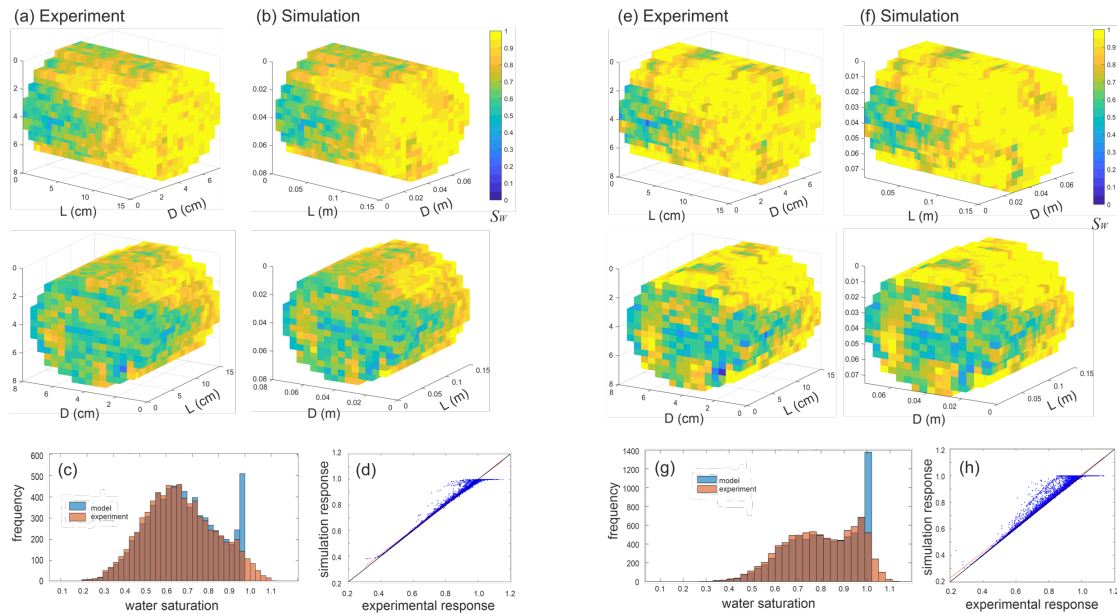
Figure 24: (a) Measured 3D water saturation profiles after 9.8 h of decane flooding. The flow direction is from left to right. (b) Corresponding simulation output. (c) Comparative experimental and simulated water saturation histograms and (d) correlation between simulated and experimentally measured saturations. The black line indicates the slope of unity with zero intercept. The red line shows a linear regression to the data. Figures (e) to (h) show the same data after 8.9 h of CO_2 flooding.

4.3   Conclusions on the Effects of Heterogeneity

In a first attempt to interpret the experimental data, we proceeded as in a classical SCAL workflow and assumed the simulation domain to be one-dimensional and homogeneous. This has the advantage that the stochastic analysis is the same as that for the SCAL data, which is numerically too costly for heterogeneous systems that are in three dimensions. A simple forward simulation using the SCAL data cannot describe the experimental data on the next larger scale with a 12× larger volume. However, good agreement can be achieved by varying the relative permeability except for the complex saturation profile, which cannot be described in the frame of a homogeneous model. This, of course, has the consequence that the relative permeability curves extracted from both scales do not match.

Consideration of the 1D porosity profile and the corresponding permeability and capillary scaling is the first step in capturing the influence of heterogeneity on two-phase flow. However, the use of SCAL data in forward modeling still leads to a discrepancy between simulation results and experimental responses. However, the experiments can again be matched by optimizing the $k_r(S_w)$ saturation functions; for the decane-brine system, the experimental responses, including the saturation profiles, are well described. The extracted $k_r(S_w)$ and $P_c(S_w)$ are close to the SCAL k_r and scaled MICP P_c. A similar picture can be drawn for the CO_2-brine displacement, but the relative CO_2 permeability, i.e., CO_2 mobility, is significantly lower with respect to the SCAL standard. However, the data are trustworthy since the SCAL data refer to the decane-brine displacement and the CO_2-brine system may have different wetting behaviors.

To verify the approach of heterogeneity implementation, the displacements were forward simulated in the 3D heterogeneous domain using $k_r(S_w)$ and $P_c(S_w)$ of the best match of the 1D heterogeneous model. For both systems, the numerical and experimental saturation states show very good correlation. The heterogeneous models, even providing a good overall description of USS experiments, experience deviations from the experimental data around the breakthrough time, as evident in all experimental responses. The exact reason for this deviation is still an open question and is under investigation.

In this article, the challenges of interpreting multiphase flow experiments on laboratory samples of rocks with mm-scale heterogeneities are discussed. Practically, it is not yet possible to implement such small-scale heterogeneity in reservoir simulations where it would be on a subgrid scale. The proof that the classic SCAL-derived relative permeability is only valid when considering small-scale heterogeneity makes SCAL application in reservoir simulation questionable. This is especially true for multiscale-heterogeneous carbonates and CO_2-brine displacements with its unfortunate mobility contrast. For such complex rocks, new concepts are needed. A better choice would be the naturally upscaled result of the 1D homogeneous interpretation, which describes the system on the scale of investigation. However, such data cannot be extracted from standard SCAL measurements as performed in the frame of field developments and may still be scale dependent.

Our results demonstrate that simple USS experiments can be used to investigate the influence of capillary heterogeneity on $k_r(S_w)$ which is especially valuable for CO_2 research since CO_2 steady state experiments are extremely demanding in terms of maintaining fluid phase equilibria during the experiment. It further shows that a rigorous upscaling procedure including rock heterogeneity on various scales is needed to use standard workflows such as special core analysis for CCS developments in carbonates.

Chapter 5

Viscous Instability and Scaling of Finger

This chapter is a reprint of (Amrollahinasab et al., 2024b) and the code for the chapter is available at (Amrollahinasab, 2024).

Wavelength

One key question regarding understanding subsurface dynamics of CO_2 brine displacement is whether CO_2 displacement of brine may become viscously unstable, given CO_2's significantly lower viscosity. Viscous fingering can profoundly impact CO_2 plume migration and storage efficiency. This is especially true if the finger width, which we refer to "wavelength", interferes with the length scale geological heterogeneity.

A critical parameter is the dominant wavelength of unstable fingers. If comparable to typical lamina thickness in layered reservoirs, instability and subsequent gravity override could strongly channel CO_2 migration. However, if much smaller, heterogeneity would dissipate fingers. Traditional Saffman-Taylor theory grossly underpredicts observed finger wavelengths.

In this study, Darcy-scale simulations reveal linear scaling of finger wavelength with interfacial tension and permeability. This observation diverges from traditional expectations set by Saffman-Taylor theory, which predominantly suggest a different scaling behavior. While our results align with the long-wavelength instability theory, a deeper analysis challenges the conventional understanding in this field.

This revelation not only necessitates a reevaluation of established models, particularly in their application to carbon capture and sequestration (CCS) processes, but also highlights a gap in our understanding of such phenomena. The observed discrepancies raise crucial questions about the accuracy and applicability of traditional theories in explaining the dynamics observed in

our simulations. Furthermore, these findings are shown to hold substantial practical implications.
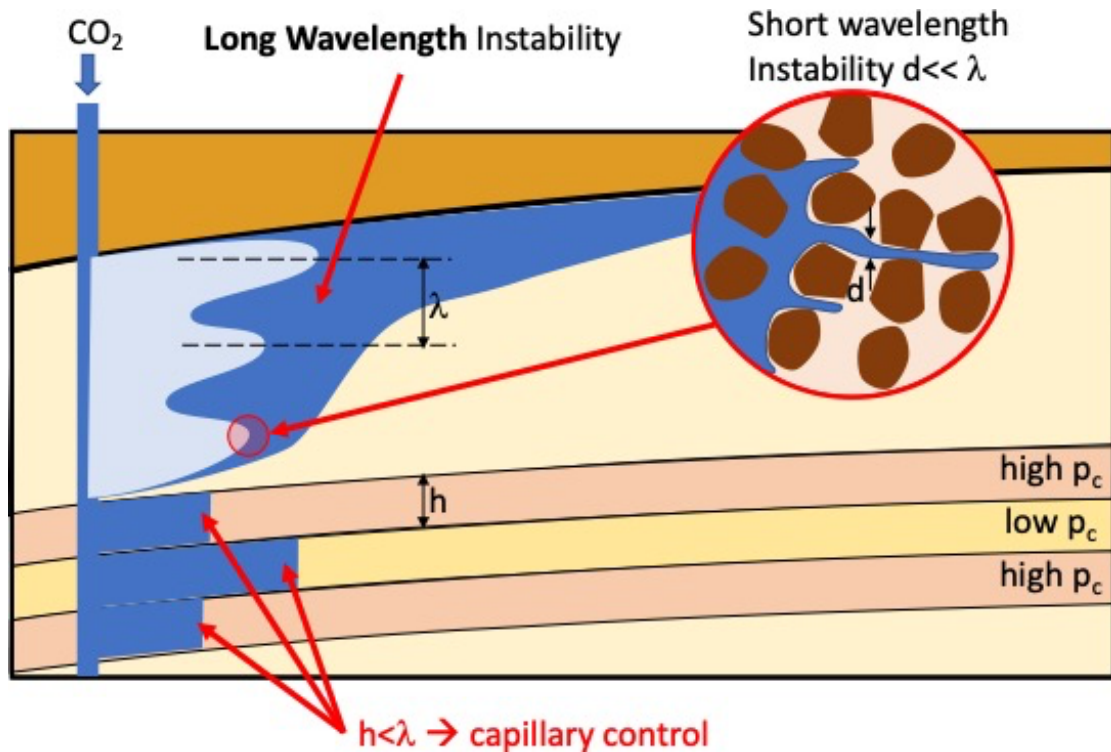
Figure 25: Injection of supercritical CO_2 into a subsurface geological formation which due to much lower viscosity of the CO_2 can become unstable (Maas et al., 2023, 2022). This long-wavelength fingering instability (King and Dunayevsky, 1989; Yortsos and Hickernell, 1989) produces fingers on the order of tens of meters for CCS relevant conditions, which are many orders of magnitude larger than the short-wavelength instability observed at pore scale with finger thickness on the order of pore scale dimensions d (Homsy, 1987; Lenormand et al., 1988). If the finger wavelength λ is much larger than the thickness h of a lamina in the geological formation, a series of fingers might be resolved but gravity will cause an unstable gravity tongue. If, however, the lamina thickness is smaller than the finger wavelength h < λ then capillary heterogeneity controls the frontal propagation of fingers (Berg and Ott, 2012) which for CCS would still occur at the length scale of tens of meters. This suggests a much stronger capillary control of CO_2 plume migration at length scales which in traditional reservoir simulation are assumed to be viscous dominated.

5.1 Stability of CO₂-brine displacement

Climate change mitigation strategies increasingly rely on carbon sequestration, necessitating a detailed understanding of this process. carbon capture and sequestration (CCS) and related processes are broadly recognized as having the potential to play a key role in meeting climate change targets (Budinis et al., 2018; Bui, 2018) and climate scenarios that stay within a maximum temperature increase of 1.5°C generally include CCS (Global CCS Institute, 2022;

IEA, 2022; Bert Metz et al., 2005; B Metz et al., 2005; Shell Inernational Limited, 2023). CCS has many economic and engineering challenges (Bui, 2018). While many aspects such as the trapping and dissolution mechanisms (Krevor et al., 2015) have already been researched at great detail, comparably little attention has been given to unstable displacement which could have a significant impact such as CO_2 plume migration distance in the subsurface. Viscous fingering is a hydrodynamic instability that can occur when a more mobile phase displaces a less mobile phase causing it to propagate much further than volumetric injection predicts. Since CO_2 has a significantly lower viscosity than the displaced brine (factor 20 for a typical supercritical CO_2 sequestration case (Berg et al., 2013)), viscous instability becomes an obvious question (Abidoye et al., 2015; Cinar and Riaz, 2014).

Numerous studies indicate instability (Cao et al., 2016; Garcia and Pruess, 2003; Liu et al., 2016; Wang et al., 2013), but traditional linear stability analysis for immiscible fingering suggests marginal stability (Berg and Ott, 2012). However, a more recent study questions the validity of the linear stability-analysis derived criteria for immiscible fingering and suggests instability for CCS cases (Maas et al., 2023, 2022). Thus, the scenario of viscous fingering of supercritical CO_2 injected into subsurface formations which is sketched in Figure 25 becomes more relevant.

A key question is what the relevant finger wavelength, λ, is. Closed-form solutions for the finger wavelength exist for short-wavelength fingering (Saffmann and Taylor, 1958) while for the probably more relevant long-wavelength fingering, only complicated integral formulations exist which due to their impractical formulation are rarely used for CCS (Daripa and Pasa, 2008; Riaz and Tchelepi, 2004; Yortsos and Hickernell, 1989). The magnitude of λ in relation to the heterogeneity length scale can be of importance (Chuoke et al., 1959). If the heterogeneity scale is larger than λ, unstable displacement (Tan and Homsy, 1992; Tchelepi et al., 1993) and gravity (Berg and Ott, 2012; Riaz and Tchelepi, 2006) can further amplify the impact of geological heterogeneity which already in stable displacement can increase the plume migration distance twofold (Benham et al., 2021a, 2021b).

Modelling studies have shown that stratification of the CO_2 flood front can significantly reduce storage efficiency by causing bypass of the lower permeability layers in the reservoir or reduction in microscopic sweep efficiency (Lenormand et al., 1988).

This increases the risk that the CO_2 may pass a spill point or a break in the top seal, potentially causing a leak (Bonto et al., 2021). Viscous fingering can also have a major impact on mixing (Nicolaeides et al., 2015) which is known to be of significant relevance for CCS (Flemisch et al., 2022). If λ is smaller than the length scale associated with capillary heterogeneity, as sketched in Figure 25, then capillary controls on displacement become more important at the

Darcy scale (Berg et al., 2013). Consequently, when predicting plume migration, Darcy-scale capillary heterogeneity needs to be considered to a greater extent when predicting plume migration.

This suggests a much stronger capillary control of CO_2 plume migration at length scales which in traditional reservoir simulation are assumed to be viscous dominated. Traditionally, the length scale at which viscous forces start to dominate over capillary forces is on the order of centimeters, consistent with the length of the capillary end-effect (Huang and Honarpour, 1998). As a consequence, reservoir simulation in hydrocarbon recovery is often conducted in the viscous limit, sometimes even using capillary pressure $p_c = 0$, except for modelling transition zones and a few other situations.

At a finger wavelength λ at the order of pore scale dimensions as predicted by the classical Saffman-Taylor equation (Saffmann and Taylor, 1958), viscous fingering would be mixed by geological heterogeneity already at the mm level and become irrelevant at the reservoir scale, and hence reservoir simulation in the viscous limit would still be adequate.

However, if the finger wavelength was on the same order of the dominant features such as lamina thickness in layered reservoirs typically considered for CCS, the situation would change completely and reservoir simulation for CCS would be capillary dominated or at least influenced potentially at the scale of tens of meters. That underlines the importance of a good understanding what the finger wavelength actually is for CCS relevant conditions.

Here we use numerical simulation to determine the finger wavelength λ and the numerical details are explained in section 2.3. Numerical simulation has been established as an important method to study viscous fingering (Bakharev et al., 2020; Blunt et al., 1994; Homsy, 1987; Mostaghimi et al., 2016). Good agreement with experiments was observed for miscible (Berg et al., 2010) and immiscible fingering (Matsuura et al., 2013). Salmo (Salmo et al., 2022, 2020) demonstrated a robust numerical model that can accurately match immiscible viscous fingering in experiments.
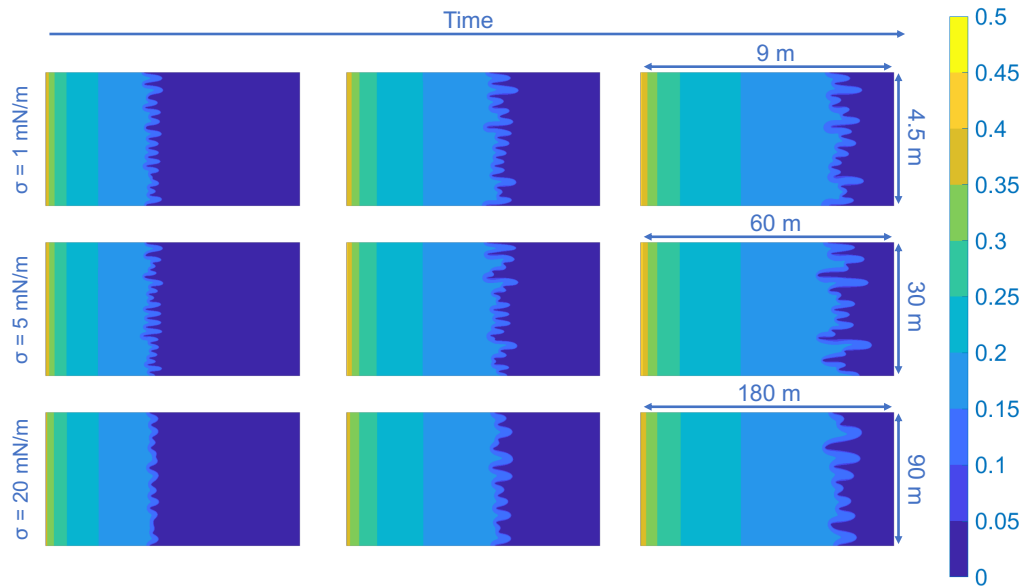
Figure 26: Saturation profiles for different domain dimensions and different σ values after different CO$_2$ injection times - each row represents the same dimensions. To count the fingers, the "contour" function in MATLAB is used to draw the 95% saturation contour line. Then, the "findpeaks" function is employed to count the peaks. Only peaks beyond the average finger amplitude were counted. The amplitude of a finger is defined as the difference between the minimum and maximum values of the saturation contour - essentially the distance from the farthest behind valley to the farthest ahead peak of a finger.

5.2   The   Finger   Wavelength   in   Immiscible   Viscous Fingering

5.2.1 The Short Wavelength Instability (Saffman & Taylor)

The viscous instability during immiscible fluid displacement in porous media has been extensively discussed in the literature since the 19th century (Chuoke et al., 1959; Dietz, 1953; Engelberts and Klinkenberg, 1951; Hagoort, 1974; Hill, 1952; Jevons, 1857; Lewis, 1949; Rayleigh, 1883; Riaz and Tchelepi, 2006, 2004; Saffmann and Taylor, 1958; Taylor, 1949). Efforts to understand and model this process have been made through various approaches, including linear stability analysis, direct numerical simulation, experimental studies at the core/slab scale, and discrete and pore-scale modeling (Salmo et al., 2022).

There are two general categories of viscous fingering: immiscible and miscible fingering. They both have in common a viscous instability which is driven by a more mobile fluid displacing a less mobile fluid (Homsy, 1987).

However, in both cases there are different mechanisms that counteracts the viscous instability. In immiscible viscous fingering this is assumed to be a capillary restoring force caused by a curved interface around a finger which is then associated with a capillary pressure. The picture is very much based on a presumed analogy between porous media flows and Hele-Shaw cells (Hele-Shaw, 1897) which both follow a viscous flow equation of Darcy type.
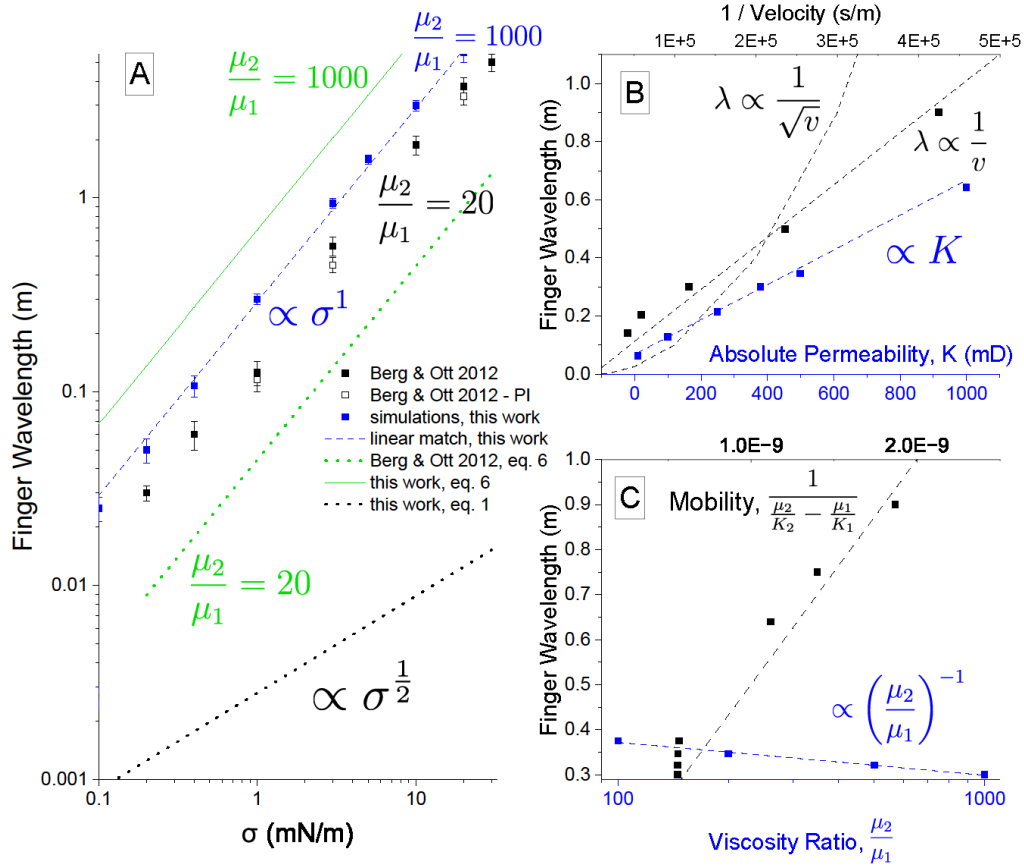
Figure 27: (A) Log-Log plot of finger wavelength λ and interfacial tension (σ) for this study (for a gaseous CO_2 case) and that of (Berg and Ott, 2012) (for a supercritical CO_2 case). (B) Finger wavelength λ as a function of permeability K suggesting a linear relationship between λ and K (C) as a function of viscosity ratio μ_2/μ_1 suggesting a linear relationship with $(\mu_2/\mu_1)^{-1}$. All scaling relationships are inconsistent with the (Saffmann and Taylor, 1958) analytical model from equation (22) which suggests square root relationships for σ, K and μ_2/μ_1 while the simulation data suggests linear relationships. Linear relationships for σ and K are predicted using the analytical model for miscible fingering and a capillary dispersion coefficient (equation (22)), however, the scaling with μ_2/μ_1 is not correct.

The concept of Hele-Shaw cell geometry (Homsy, 1987) is that a longitudinal viscous instability is balanced by a transversal capillary restoring force (represented by interfacial tension σ), where the capillary pressure from the curvature induced by the fingers becomes the restoring force that flattens the interface.

The traditional view is that the description of immiscible fingering in porous media follows the same logic as in Hele-Shaw cells. The linear stability analysis by (Saffmann and Taylor, 1958) for viscous fingering predicts a wavelength λ with maximum growth rate:

$$\lambda = \sqrt{3} \cdot 2\pi \sqrt{\frac{\sigma}{(\mu_2/k_2 - \mu_1/k_1)(u - u_c)}} \propto \sigma^{1/2} \tag{22}$$

where k_1 and k_2 are the permeability and μ_1 and μ_2 the viscosity of the displacing and displaced phases, respectively. k_i/μ_i is the mobility of fluid phase i which is a common concept in fractional flow physics (Dake, 1978). u is the velocity and u_c is the critical velocity which depends on gravity (as gravity can stabilize the fingering when flowing in vertical direction) (Homsy, 1987).

Regarding porous media, the review paper by Homsy (Homsy, 1987) points out that the wavenumber $k = 1/\lambda$ of the fastest growing mode scales as $k \propto O(Ca^{1/2})$ meaning that $\lambda \propto Ca^{-1/2} \propto \sigma^{1/2}$. King & Dunayevsky and Yortsos & Hickernell distinguish between short- and long-wavelength instability (Daripa and Pasa, 2008; King and Dunayevsky, 1989; Riaz and Tchelepi, 2004; Sorbie et al., 2020; Yortsos and Hickernell, 1989; Yortsos and Hunag, 1986). The short-wavelength instability is associated with fingering at the pore scale (Lenormand et al., 1988; Zhao et al., 2016) because the finger wavelength λ is on the same order of magnitude as the radius of curvature of the interface r, as shown in Figure 28A, and has the same scaling as in Hele-Shaw cells, i.e., equation (22). This intuitive picture is consistent with equation (22), assuming that the permeability scales with $\frac{1}{r}$.

However, in a Darcy-scale porous medium, the length scale at which the fluid-fluid interface is curved occurs at the pore scale. In most relevant porous media, this pore-scale dimension is many orders of magnitude smaller than the length scale of viscous fingers observed at the Darcy scale. While many studies attempted to accommodate for this by introducing an effective interfacial tension, the results remain effectively within the influence of the concept of the short-wavelength instability (Smith and Zhang, 2001).

The long-wavelength instability relevant for the Darcy scale, has the fastest growing mode scaling linearly with capillary number (Yortsos and Hickernell, 1989), i.e., $\lambda \propto Ca^{-1} \propto \sigma^{1}$ (compatible with Figure 27). However, Stokes et al. observed a wetting fluid displacing a non-wetting fluid (imbibition) at the Darcy scale $\lambda \propto \sigma^{1/2}$ (Stokes et al., 1986) and argued that the drainage process is different, but they did not provide a scaling law.

The difference between short- and long-wavelength instability is not that commonly known because the overwhelming body of literature cites the Saffman & Taylor work (Saffmann and Taylor, 1958) with equation (22) that drastically underestimates λ data from experiments (Stokes et al., 1986) (see also the comparison with situations relevant for CCS in Figure 27). Additionally, the controversy regarding the correct scaling, i.e., (Stokes et al., 1986) vs. (Yortsos and Hickernell, 1989), is not fully resolved.

The sensitivity to wetting (Stokes et al., 1986; Zhao et al., 2016) could point to a more conceptual difference between forced drainage vs. spontaneous, capillary-driven imbibition processes, which follow very different scaling laws (Schmid and Geiger, 2012). Perhaps it is as simple as noting that for spontaneous imbibition the length scale of invasion scales as $L \propto \sigma^{1/2}$ (Lucas, 1918; Washburn, 1921), and around the onset of viscous fingering where finger length $L \approx \lambda$, λ then consequently also scales as $\sigma^{1/2}$, but a full investigation is beyond the scope of this work.

In essence, CCS is clearly a drainage process, which probably makes the work by (Stokes et al., 1986) less applicable; however, it is important to clarify, and this is one of the motivations for this work. Additionally, the formulations for the long-wavelength instability λ (Daripa and Pasa, 2008; King and Dunayevsky, 1989; Yortsos and Hickernell, 1989) involve integral equations that are not that practical which is perhaps the reason why there is no common reference for their use in CCS. The aim of this work is to provide, in form of graphs and tables, practical estimates for λ for conditions relevant for CCS, based on a more intuitive reasoning regarding the long-wavelength instability.

Numerical simulations by (Berg and Ott, 2012) computing stable and unstable displacement scenarios relevant for CCS found that the finger wavelength λ scales with interfacial tension σ as $\lambda \propto \sigma^1$ (see also Figure 27A) while the commonly used description for immiscible fingering from linear stability analysis predicts $\lambda \propto \sigma^{1/2}$ (Homsy, 1987).

5.2.2 Long Wavelength Fingering: Mixing in the Capillary Dispersion Zone

In immiscible displacement in porous media, viscous fingers of wavelength λ were observed at a length scale where the shock front was sharp i.e. the width of the capillary dispersion zone Δx was small compared to the scale of observation which was of the order of the wavelength λ (Berg and Ott, 2012) which is also shown in Figure 29C. That suggests that the relevant mechanism counteracting fingering in immiscible displacement in porous media is a mixing process, both longitudinal and transversal, rather than merely a transversal capillary restoring force (Berg and Ott, 2012).
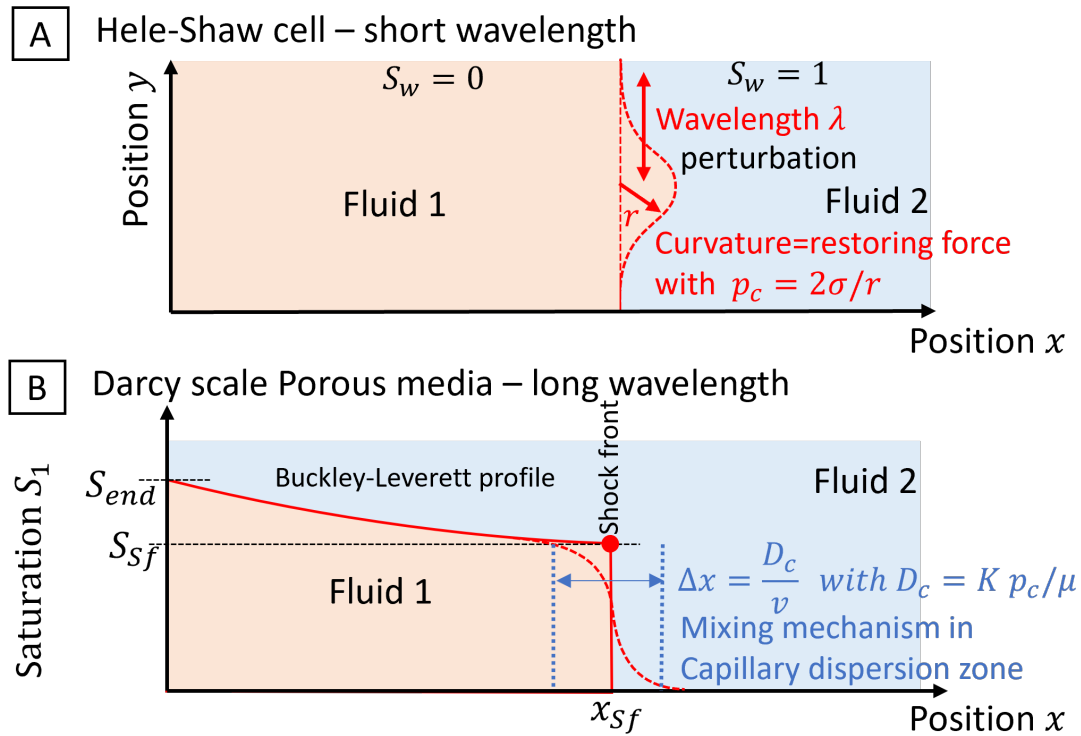
Figure 28: In a Hele-Shaw cell with a well-defined interface between displacing fluid 1 and displaced fluid 2, the capillary pressure caused by the curved interface with interfacial tension σ is the restoring force counteracting the viscous instability (A). In a porous medium, next to this short-wavelength instability, the more critical instability is the long-wavelength instability (King and Dunayevsky, 1989; Yortsos and Hickernell, 1989)*, where the counteracting mechanism is the mixing process in the capillary dispersion zone Δx (B)* (Berg and Ott, 2012)*.*

Considering that the capillary dispersion mechanism counteracts the viscous fingering, in porous media there might actually be a closer analogy with miscible fingering (Tan and Homsy, 1992) which was also the starting point for (Yortsos and Hickernell, 1989). In miscible viscous fingering, the fastest growing mode has the wave number $k_m = (2\sqrt{5} - 4)R/4$ (Tan and Homsy, 1992) where R is the logarithmic viscosity ratio $R = \ln \mu_2/\mu_1$ (originating from the exponential blending rule for viscosity in miscible displacement (Berg et al., 2010)). The scaled wavelength of the fastest growing mode for miscible fingering is:

$$\lambda_m = D/v\lambda_m^*$$ (23)

with $\lambda_m^* = 2\pi/k_m$ or (Tan and Homsy, 1992). Here D is the hydrodynamic dispersion coefficient that in miscible displacement describes the mixing process in the porous medium. Experimentally reasonable agreement has been observed with this picture for miscible viscous fingering (Berg et al., 2010).

Since for immiscible fingering the scaling of finger wavelength λ with the width of the capillary dispersion zone Δx (Berg and Ott, 2012), suggesting a mixing process as counteracting mechanism, we use the capillary dispersion coefficient:

$$D_c = \frac{K\overline{p_c}}{\mu_1} \tag{24}$$

instead of the hydrodynamic dispersion. This approximation is based on the observation that the macroscopic capillary number $Ca = \mu_1 vL/\overline{p_c}K$ (Hilfer and Øren, 1996) shows an onset of the instability at $Ca \approx 1$ (Berg and Ott, 2012). We can re-write Ca as the ratio of the length scale of observation L and the length scale of the smear-out of the shock front Δx as $Ca = L/\Delta x$.

$$\Delta x = \frac{K\overline{p_c}}{\mu_1 v} \tag{25}$$

Then, equation (25) is an estimate of the width of the capillary dispersion zone which can be understood as an order of magnitude estimate for capillary dispersivity $\Delta x = D_c/v$ meaning that $D_c = K\overline{p_c}/\mu$ (Berg and Ott, 2012). This is a very common concept in the fractional flow description of immiscible displacement with capillarity (Daripa and Pasa, 2008; Novy et al., 1989; Toledo et al., 1994). Here $\overline{p_c}$ is a characteristic value of the capillary pressure (Hilfer and Øren, 1996) which is proportional to interfacial tension $\overline{p_c} \propto \sigma$.

This approach is justified by the observation in Figure 29C that the width of the capillary dispersion zone Δx around the shock front obtained from 1D simulations is very closely related to the finger wavelength λ i.e. has the same linear scaling with intefacial tension σ. The estimate from equation (25) agrees in terms of scaling with σ but there is a quantitative mismatch with Δx from the 1D simulations which is most likely caused by μ_1 not being a good estimate for viscosity in the capillary dispersion zone where for the CO_2-brine system there is a large viscosity gradient.

While a full rigorous treatment is presented in (King and Dunayevsky, 1989; Yortsos and Hickernell, 1989), here we show that the simple intuitive argument and combining equation (23) with the capillary dispersion coefficient from equation (24) leading to:

$$\lambda(\sigma) = \frac{(2\sqrt{5} - 4)K\ln \mu_2/\mu_1}{4\pi v \mu_1 r} \sigma \propto \sigma^1 \tag{26}$$

produces a linear scaling of λ with σ (Figure 27A), and permeability K (Figure 27B). As Figure 27A already suggests the scaling with viscosity in equation (26) is not correct which is also not expected. The factor $\ln \mu_2/\mu_1$ in equation (26) is only applicable for miscible displacement where viscosity blending occurs at molecular scale and the factor is a result of an exponential

blending rule (Berg et al., 2010) which is not applicable to immiscible displacement in porous media where blending occurs at Darcy scale through fractional flow. Also the comparison of Δx estimate from equation (25) with the Δx estimated from the 1D saturation profiles in Figure 29 suggests that there is an issue with using viscosity μ_1 as viscosity estimate for the viscosity in the capillary dispersion where there is a large viscosity gradient.

Figure 27C suggests a linear relationship with $(\mu_2/\mu_1)^{-1}$ but with different slopes depending on whether μ_1 or μ_2 are kept fixed. We find an almost linear trend (with zero offset) using $\mu_2/K_2 - \mu_1/K_1$ but realize that a simple algebraic form may not be accurate since the viscosity scaling needs to be consistent with the criteria for the onset of instability which is given by an integral over the whole shock front profile (Maas et al., 2022).
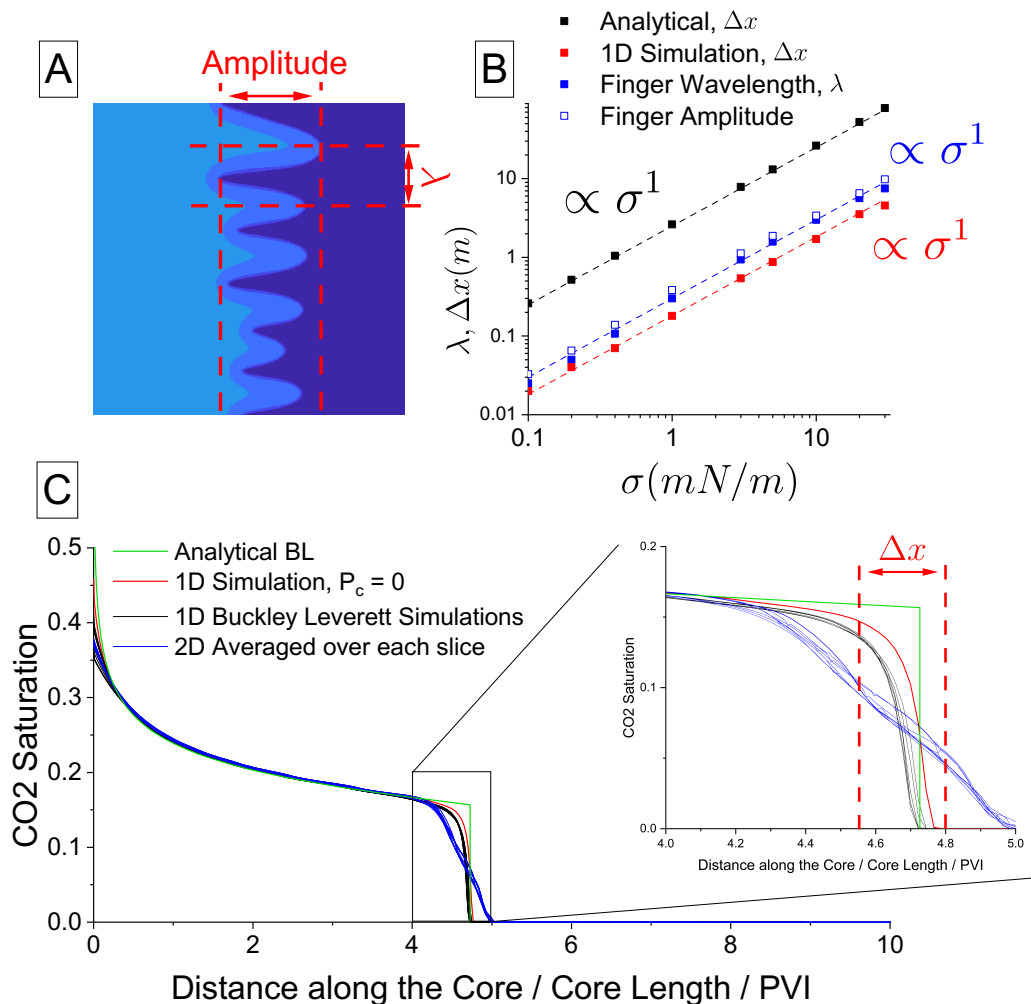
Figure 29: The finger wavelength λ (A) and the width of the capillary dispersion zone Δx around the shock front from 1D simulations (i.e. without fingering) scale linearly with interfacial tension σ (C). At the onset of fingering the finger amplitude is approximately the same as the wavelength λ. There is almost a quantitative match between Δx obtained from the 1D saturation profiles and the finger wavelength λ and amplitude which supporting the underlying mechanism of mixing in the capillary dispersion zone.

The estimate of Δx from equation (25) shows the same linear scaling as λ but is about a factor 10 larger than the width around the 1D shock front which is likely caused by the large viscosity gradient within the capillary dispersion zone which is not accounted for in equation (25).

5.3   Conclusions on Viscous Stability Analysis

Viscous fingering is a complex subject in which the type of fingering (immiscible, miscible, short- vs. long-wavelength), wetting conditions and other factors govern scaling relationships for the finger wavelength λ that lead to variations in λ by several orders of magnitude. To assess the potential impact of viscous fingering on CO_2 sequestration it is difficult to understand which formulation is applicable.

Darcy-scale numerical simulations (Figure 26) suggest that the finger wavelength scales linearly with interfacial tension and permeability, which is consistent with the long-wavelength instability studied by linear stability analysis (King and Dunayevsky, 1989; Yortsos and Hickernell, 1989).

While linear stability analysis is mathematically more rigorous (Daripa and Pasa, 2008; King and Dunayevsky, 1989; Riaz and Tchelepi, 2004; Yortsos and Hickernell, 1989), it unfortunately does not provide a simple analytical expression for the finger wavelength.

Therefore, here, we provide a simple, intuitive argument that - within its own limitations - provides the correct scaling of the finger wavelength with interfacial tension and permeability. Observations of earlier work (Berg and Ott, 2012) suggesting that the finger wavelength is linked to the length of the capillary dispersion zone supports the proposition that a mixing process, as opposed to a mere transversal capillary restoring force, acts as the counteracting mechanism to fingering, which was validated against numerical simulations (Figure 29).

Using miscible fingering as a starting point but with capillary dispersion as the mixing mechanism produces a linear scaling of wavelength with interfacial tension and permeability as observed numerically, which is consistent with linear stability analysis (King and Dunayevsky, 1989; Yortsos and Hickernell, 1989). However, the scaling with viscosity was not correct, which is also not expected from such an oversimplified approach.

Having validated the numerical simulations against the scaling relationships in interfacial tension and permeability and confirmed the capillary-dispersion mixing mechanism, there is now confidence in the validity of the finger wavelength obtained from numerical simulations.

Therefore, the finger wavelength relevant for a number of CCS relevant pressure and temperature conditions (and associated fluid viscosity and interfacial tension) listed in Table 2 predicts finger wavelengths of tens to a hundred meters instead of the centimeter scale or less.

Table 2: Finger wavelength for a number of pressure (P) and temperature (T) conditions potentially relevant for CCS.

P (MPa)	T (°K)	μ_{brine} (cp)	μ_{CO_2} (cp)	σ (mN/m)	λ (m)
30	374.3	0.280	0.0536	25	145.7
15	343.3	0.402	0.0375	30	125.3
9	333.6	0.463	0.0214	37.5	84.7
6	312.8	0.658	0.0178	40	27.7

The findings may have implications for the implementation of CCS projects at the field scale where numerical modeling is used as a primary tool for design and uncertainty assessment (Benham et al., 2021a, 2021b; Hesse, 2008). Viscous-unstable displacement in the presence of gravity (Berg and Ott, 2012; Riaz and Tchelepi, 2006) at this length scale may offer explanations for the discrepancy between plume migration modeling forecasts and actual observations at the field scale, such as in the Sleipner project (Williams et al., 2018). Findings in the literature, such as alignment with the top seal structure (Cowton et al., 2018), are in line with observations of unstable gravity tongues (Berg and Ott, 2012). The consistency with capillary-controlled migration modeling, even at tens of meters (Cavanagh and Hazeldine, 2014), is in line with laboratory-scale CCS experiments where the heterogeneity scale was smaller than the finger wavelength (Berg et al., 2013; Zhang et al., 2011), emphasizing the importance of the finger wavelength. Explicitly capturing the effects of viscous instability requires a grid resolution finer than the finger wavelength. The quantitative estimate provided in Figure 27 and Table 2 can serve as a practical starting point.

Chapter 6

Summary and Conclusions

This thesis presents a comprehensive examination of CO_2-brine displacement dynamics in porous media through integrated experimental and numerical approaches. By combining traditional core analysis measurements with advanced methodologies, the research demonstrates the complex interplay between multiphase flow parameters and processes influencing CO_2 plume migration. The findings bridge the gap between lab-derived data and field-scale applications, enhancing predictive capabilities for carbon capture and storage operations.

As first step the work tackles the inherent uncertainties in quantifying key parameters (relative permeability and capillary pressure) governing immiscible fluid flow in rock volumes that can be considered homogeneous. A sophisticated stochastic workflow for special core analysis (SCAL) data interpretation is introduced, simultaneously matching steady-state and centrifuge measurements using flexible point-by-point saturation functions. Rigorous uncertainty quantification reveals probability distributions and correlations, overcoming limitations of conventional power-law representations. This comprehensive SCAL interpretation and uncertainty analysis provides more objective fluid flow characterization vital for stochastic reservoir modeling. The resulting methodology and the simulator developed can be considered the most advanced and have been made available to the public.

Taking a step further from SCAL methods with the assumption of homogeneity to larger volume heterogenous rock samples, the study reveals significant deviations between SCAL interpretation and larger-volume experiments, underscoring traditional techniques' inability to adequately account for sub-core heterogeneity. By incorporating 3D porosity and saturation distributions from X-ray CT imaging into history matching of unsteady-state core floods, a rigorous upscaling procedure is demonstrated to capture heterogeneity impacts on the Darcy

scale. The resulting relative permeability shows the discrepancy, emphasizing the need of upscaling workflows in complex carbonates.

CO_2-brine displacement is potentially unstable and leads to viscous fingering. If the wavelength of the fingers is of the same order of magnitude as, for example, the lamination of the rock formation, this can massively impair the sweep efficiency. In order to understand the interaction of formation heterogeneity and displacement instability, it was necessary to evaluate the scaling behavior of the finger wavelength. The findings align with theoretical predictions for long-wavelength fingering but contrast sharply with classical notions based on pore-scale capillary restoration. A conceptual model based on mixing in the capillary dispersion zone intuitively reconciles viscous fingering in miscible and immiscible displacement. By determining instability length scales ranging from tens to hundred meters under realistic sequestration conditions, the research challenges assumptions of core-scale viscous effects, indicating greater capillary controls at Darcy scales.

The integrated research methodology spanning across length scales provides pivotal insights into factors governing CO_2 migration while advancing scientific understanding of CO_2-brine interactions. The findings advocate for robust upscaling concepts and modeling considerations to improve reservoir forecasting capabilities. By enhancing predictive accuracy, this thesis contributes to optimized carbon capture and storage strategies, promoting sustainable energy solutions to mitigate climate change.

The work bridges the gap between lab and field scales but also reveals remaining knowledge gaps. Additional heterogeneous lithologies could be investigated with the SCAL workflow to expand applicability. Secondary drainage and imbibition scenarios present further complexities to explore. The upscaling framework could be extended to larger cores and additional fluid systems to enhance generalization. Refining viscous fingering theories by incorporating gravity, heterogeneity, and pore-scale effects would provide a more comprehensive perspective. Validating the concepts against field projects and elucidating the impact on trapping mechanisms could enhance adoption into industry practices. Addressing these aspects through integrated experimental and numerical approaches will continue to advance the predictive capabilities for carbon geological sequestration.

References

Abidoye, L.K., Khudaida, K.J., Das, D.B., 2015. Geological Carbon Sequestration in the Context of Two-Phase Flow in Porous Media: A Review. Critical Reivews in Environmental Science and Technology 45, 1105--1147.

Ahmed, T., 2018. Reservoir engineering handbook. Gulf professional publishing.

Aminu, M.D., Nabavi, S.A., Rochelle, C.A., Manovic, V., 2017. A review of developments in carbon dioxide storage. Appl Energy 208, 1389–1419. https://doi.org/10.1016/j.apenergy.2017.09.015

Amrollahinasab, O., 2024. immiscible-fingerwavelength-simulation Github Repository [WWW Document]. URL https://github.com/omidreza-amrollahi/immiscible-fingerwavelength-simulation (accessed 2.5.24).

Amrollahinasab, O., 2024. ad-scal-heterogeneous Github Repository [WWW Document]. URL https://github.com/omidreza-amrollahi/ad-scal-heterogeneous (accessed 2.5.24).

Amrollahinasab, O., Azizmohammadi, S., 2022. ad-scal Github Repository [WWW Document]. URL https://github.com/SiroosAzizmohammadi/ad-scal (accessed 10.26.23).

Amrollahinasab, Omidreza, Azizmohammadi, S., Ott, H., 2023. Simultaneous interpretation of SCAL data with different degrees of freedom and uncertainty analysis. Comput Geotech 105074. https://doi.org/10.1016/j.compgeo.2022.105074

Amrollahinasab, O., Azizmohammadi, S., Ott, H., 2022. Simultaneous Interpretation and Uncertainty Analysis of SCAL Data from Complex Rocks. Proceedings of International Symposium of the Society of Core Analysts (SCA 2022), Austin, United States.

Amrollahinasab, O., Jammernegg, B., Azizmohammadi, S., Ott, H., 2024a. Stochastic Interpretation of CO2-Brine Primary Displacement in Heterogeneous Carbonate Rocks. Submitted to Journal.

Amrollahinasab, Omidreza, Jammernegg, B., Azizmohammadi, S., Ott, H., 2023. Stochastic Interpretation of CO2-Brine Primary Displacement in Heterogeneous Carbonate Rocks. International Symposium of the Society of Core Analysts (SCA 2023), Abu Dhabi, UAE.

Amrollahinasab, O., Ott, H., Berg, S., 2024b. The Wavelength of Viscous-Unstable Displacement in CO2 Sequestration. Submitted to Journal.

Bachu, S., 2008. CO2 storage in geological media: Role, means, status and barriers to deployment. Prog Energy Combust Sci 34, 254–273. https://doi.org/10.1016/j.pecs.2007.10.001

Bachu, S., Adams, J.J., 2003. Sequestration of CO2 in geological media in response to climate change: capacity of deep saline aquifers to sequester CO2 in solution. Energy Convers Manag 44, 3151–3175. https://doi.org/10.1016/S0196-8904(03)00101-8

Bakharev, F., Campoli, L., Enin, A., Matveenko, S., Petrova, Y., Tikhomirov, S., Yakovlev, A., 2020. Numerical investigation of viscous fingering phenomenon for raw field data. Transp Porous Media 132, 443–464.

Benham, G.P., Bickle, M.J., Neufeld, J.A., 2021a. Upscaling multiphase viscous-to-capillary transitions in heterogeneous porous media. J. Fluid Mech. 911, A59.

Benham, G.P., Bickle, M.J., Neufeld, J.A., 2021b. Two-phase gravity currents in layered porous media. J. Fluid Mech. 922, A7.

Benson, S.M., Cole, D.R., 2008. CO2 Sequestration in Deep Sedimentary Formations. Elements 4, 325–331. https://doi.org/10.2113/gselements.4.5.325

Berg, S., Oedai, S., Landman, A.J., Brussee, N., Boele, M., Valdez, R., Van Gelder, K., 2010. Miscible displacement of oils by carbon disulfide in porous media: Experiments and analysis. Physics of Fluids 22.

Berg, S., Oedai, S., Ott, H., 2013. Displacement and mass transfer between saturated and unsaturated CO2–brine systems in sandstone. International Journal of Greenhouse Gas Control 12, 478–492. https://doi.org/10.1016/j.ijggc.2011.04.005

Berg, S., Ott, H., 2012. Stability of CO2–brine immiscible displacement. International Journal of Greenhouse Gas Control 11, 188–203.

Berg, S., Unsal, E., Dijk, H., 2021a. Non-uniqueness and uncertainty quantification of relative permeability measurements by inverse modelling. Comput Geotech 132, 103964. https://doi.org/10.1016/j.compgeo.2020.103964

Berg, S., Unsal, E., Dijk, H., 2021b. Sensitivity and Uncertainty Analysis for Parameterization of Multiphase Flow Models. Transp Porous Media 140, 27–57. https://doi.org/10.1007/s11242-021-01576-4

Blunt, M.J., Barker, J.W., Rubin, B., Mansfield, M., Culverwell, I.D., Christie, M.A., 1994. Predictive theory for viscous fingering in compositional displacement. SPE Reservoir Engineering 9, 73–80.

Bonto, M., Welch, M.J., Lüthje, M., Andersen, S.I., Veshareh, M.J., Amour, F., Afrough, A., Mokhtari, R., Hajiabadi, M.R., Alizadeh, M.R., others, 2021. Challenges and enablers for large-scale CO_2 storage in chalk formations. Earth Sci Rev 222, 103826.

Boot-Handford, M.E., Abanades, J.C., Anthony, E.J., Blunt, M.J., Brandani, S., Mac Dowell, N., Fernández, J.R., Ferrari, M.-C., Gross, R., Hallett, J.P., Haszeldine, R.S., Heptonstall, P., Lyngfelt, A., Makuch, Z., Mangano, E., Porter, R.T.J., Pourkashanian, M., Rochelle, G.T., Shah, N., Yao, J.G., Fennell, P.S., 2014. Carbon capture and storage update. Energy Environ. Sci. 7, 130–189. https://doi.org/10.1039/C3EE42350F

BP, 2020. Statistical Review of World Energy 2019.

Buckley, S.E., Leverett, M.C., 1942. Mechanism of Fluid Displacement in Sands. Transactions of the AIME 146, 107–116. https://doi.org/10.2118/942107-G

Budinis, S., Krevor, S., Mac Dowell, N., Brandon, N., Hawkes, A., 2018. An assessment of CCS costs, barriers and potential. Energy Strategy Reviews 22, 61–81. https://doi.org/10.1016/j.esr.2018.08.003

Bui, M. et al., 2018. Carbon capture and storage (CCS): the way forward. Energy Environ. Sci. 11, 1062. https://doi.org/10.1039/c7ee02342a

Burmester, G., Jones, A., Jurcic, H., Amrollahinasab, O., Arnold, P., Ott, H., 2023. Predictions of Relative Permeability and Fractional Flow on Log Scale – Pilot Projects Results, in: 84th EAGE Annual Conference & Exhibition. European Association of Geoscientists & Engineers, pp. 1–5. https://doi.org/10.3997/2214-4609.202310097

Burmester, G., Zekiri, F., Jurcic, H., Arnold, P., Ott, H., 2022. Integration and Upscaling of Multi-Phase Fluid Flow Properties in Clastic Reservoirs, in: 83rd EAGE Annual Conference & Exhibition. European Association of Geoscientists & Engineers, pp. 1–5. https://doi.org/10.3997/2214-4609.202210939

Calvin, K., Dasgupta, D., Krinner, G., Mukherji, A., Thorne, P.W., Trisos, C., Romero, J., Aldunce, P., Barrett, K., Blanco, G., Cheung, W.W.L., Connors, S., Denton, F., Diongue-Niang, A., Dodman, D., Garschagen, M., Geden, O., Hayward, B., Jones, C., Jotzo, F., Krug, T., Lasco, R., Lee, Y.-Y., Masson-Delmotte, V., Meinshausen, M., Mintenbeck, K., Mokssit, A., Otto, F.E.L., Pathak, M., Pirani, A., Poloczanska, E., Pörtner, H.-O., Revi, A., Roberts, D.C., Roy, J., Ruane, A.C., Skea, J., Shukla, P.R., Slade, R., Slangen, A., Sokona, Y., Sörensson, A.A., Tignor, M., van Vuuren, D., Wei, Y.-M., Winkler, H., Zhai, P., Zommers, Z., Hourcade, J.-C., Johnson, F.X., Pachauri, S., Simpson, N.P., Singh, C., Thomas, A., Totin, E., Alegría, A., Armour, K., Bednar-Friedl, B., Blok, K., Cissé, G., Dentener, F., Eriksen, S., Fischer, E., Garner, G., Guivarch, C., Haasnoot, M., Hansen, G., Hauser, M., Hawkins, E., Hermans, T., Kopp, R., Leprince-Ringuet, N., Lewis, J., Ley, D., Ludden, C., Niamir, L., Nicholls, Z., Some, S., Szopa, S., Trewin, B., van der Wijst, K.-I., Winter, G., Witting, M., Birt, A., Ha, M., 2023. IPCC, 2023: Climate Change 2023: Synthesis Report. Contribution of Working Groups I, II and III to the Sixth Assessment Report of the Intergovernmental Panel on Climate Change [Core Writing Team, H. Lee and J. Romero (eds.)]. IPCC, Geneva, Switzerland. https://doi.org/10.59327/IPCC/AR6-9789291691647

Cao, S.C., Dai, S., Jung, J., 2016. Supercritical CO_2 and brine displacement in geological carbon sequestration: Micromodel and pore network simulation studies. International Journal of Greenhouse Gas Control 44, 104–114.

Cavanagh, A.J., Hazeldine, R.S., 2014. The Sleipner storage site: Capillary flow modeling of a layered CO2 plume requires fractured shale barriers within the Utsira Formation. In. J. Greenhouse Gas Control 21, 101–112.

Celia, M.A., Nordbotten, J.M., 2009. Practical Modeling Approaches for Geological Storage of Carbon Dioxide. Groundwater 47, 627–638. https://doi.org/10.1111/j.1745-6584.2009.00590.x

Chang, J., Yortsos, Y.C., 1992. Effect of Capillary Heterogeneity on Buckley-Leverett Displacement. SPE Reservoir Engineering 7, 285–293. https://doi.org/10.2118/18798-PA

Chuoke, R.L., van Meurs, P., van der Poel, C., 1959. The instability of slow, immiscible, viscous liquid-liquid displacements in permeable media. Trans. AIME 216, 188–194.

Cinar, Y., Riaz, A., 2014. Carbon dioxidesequestrationinsalineformations:Part2—Review of multiphase flowmodeling. J Pet Sci Eng 124, 381–398.

Corey, A.T., 1954. The interrelation between gas and oil relative permeabilities. Producers monthly 38–41.

Cowton, L.R., Neufeld, J.A., White, N.J., Bickle, M.J., Williams, G.A., White, J.C., Chadwick, R.A., 2018. Benchmarking of vertically-integrated CO_2 flow simulations at the Sleipner Field, North Sea. Earth Planet Sci Lett 491, 121–133.

Dake, L.P., 1983. Fundamentals of reservoir engineering. Elsevier.

Dake, L.P., 1978. Fundamentals of reservoir engineering. Elsevier, Amsterdam.

Daripa, P., Pasa, G., 2008. On capillary slowdown of viscous fingering in immiscible displacement in porous media. Transp Porous Media 75, 1–16.

Davis, S.J., Lewis, N.S., Shaner, M., Aggarwal, S., Arent, D., Azevedo, I.L., Benson, S.M., Bradley, T., Brouwer, J., Chiang, Y.-M., Clack, C.T.M., Cohen, A., Doig, S., Edmonds, J., Fennell, P., Field, C.B., Hannegan, B., Hodge, B.-M., Hoffert, M.I., Ingersoll, E., Jaramillo, P., Lackner, K.S., Mach, K.J., Mastrandrea, M., Ogden, J., Peterson, P.F., Sanchez, D.L., Sperling, D., Stagner, J., Trancik, J.E., Yang, C.-J., Caldeira, K., 2018. Net-zero emissions energy systems. Science (1979) 360. https://doi.org/10.1126/science.aas9793

Davison, J., 2007. Performance and costs of power plants with capture and storage of CO2. Energy 32, 1163–1176. https://doi.org/10.1016/j.energy.2006.07.039

Dietz, D., 1953. A theoretical approach to the problem of encroaching and by-passing edge water. Proc. Kon. Ned. Akad. Wetenschap. B56, 83–92.

Dooley, J.J., Davidson, C.L., Dahowski, R.T., 2009. An Assessment of the Commercial Availability of Carbon Dioxide Capture and Storage Technologies as of June 2009. Richland, WA (United States). https://doi.org/10.2172/967229

Doughty, C., Oldenburg, C.M., 2020. CO2 plume evolution in a depleted natural gas reservoir: Modeling of conformance uncertainty reduction over time. International Journal of Greenhouse Gas Control 97, 103026. https://doi.org/10.1016/j.ijggc.2020.103026

Egermann, P., Lenormand, R., 2005. A New Methodology to Evaluate the Impact of Localized Heterogeneity on Petrophysical Parameters (kr, Pc Applied to Carbonate Rocks. Petrophysics - The SPWLA Journal of Formation Evaluation and Reservoir Description 46.

Energy Institute, 2023. Statistical Review of World Energy.

Engelberts, W.F., Klinkenberg, L.J., 1951. Laboratory Experiments on the Displacement of Oil by Water from Packs of Granular Materials, in: Proc. 3rd World Petr. Congr., The Hague. p. 544.

EPA, 2021. Inventory of U.S. Greenhouse Gas Emissions and Sinks.

Figueroa, J.D., Fout, T., Plasynski, S., McIlvried, H., Srivastava, R.D., 2008. Advances in CO2 capture technology—The U.S. Department of Energy's Carbon Sequestration Program. International Journal of Greenhouse Gas Control 2, 9–20. https://doi.org/10.1016/S1750-5836(07)00094-1

Flemisch, B., Nordbotten, J.M., Fernø, M., Juanes, R., Class, H., Delshad, M., Doster, F., Ennis-King, J., Franc, J., Geiger, S., Gläser, D., Green, C., Gunning, J., Hjibeygi, H., Jackson, S.J., Jammoul, M., Karra, S., Li, J., Mathäi, S., Miller, T., Shao, Q., Spurin, C., Stauffer, P., Tchelepi, H., Tian, X., Viswanathan, H., Voskov, D., Wang, Y., Wapperom, M., Wheeler, M.F., Wilkins, A., Youssef, A.A., Zhang, Z., 2022. The FluidFlower International Benchmark Study: Process, Modeling Results, and Comparison to Experimental Data. ArXiv 2302.10986.

Garcia, J.E., Pruess, K., 2003. Flow Instabilities During Injection of CO_2 into Saline Aquifers, in: PROCEEDINGS TOUGH Symposium, Lawrence Berkeley National Laboratory, Berkeley, California, May 12-14.

Geels, F.W., McMeekin, A., Mylan, J., Southerton, D., 2015. A critical appraisal of Sustainable Consumption and Production research: The reformist, revolutionary and reconfiguration positions. Global Environmental Change 34, 1–12. https://doi.org/10.1016/j.gloenvcha.2015.04.013

Georgiadis, A., Berg, S., Makurat, A., Maitland, G., Ott, H., 2013. Pore-scale micro-computed-tomography imaging: Nonwetting-phase cluster-size distribution during drainage and imbibition. Phys Rev E 88, 033002. https://doi.org/10.1103/PhysRevE.88.033002

Georgiadis, A., Maitland, G., Trusler, J.P.M., Bismarck, A., 2010. Interfacial Tension Measurements of the (H2O + CO2) System at Elevated Pressures and Temperatures. J Chem Eng Data 55, 4168–4175. https://doi.org/10.1021/je100198g

Global CCS Institute, 2022. The Global Status of CCS 2022.

Hagoort, J., 1980. Oil Recovery by Gravity Drainage. Society of Petroleum Engineers Journal 20, 139–150. https://doi.org/10.2118/7424-PA

Hagoort, J., 1974. Displacement stability of water drives in water-wet connate-water-bearing reservoirs. SPE J. 14, 63–74.

Hassler, G.L., Brunner, E., 1945. Measurement of Capillary Pressures in Small Core Samples. Transactions of the AIME 160, 114–123. https://doi.org/10.2118/945114-G

Hele-Shaw, H.S., 1897. Experiments on the nature of the surface resistance in pipes and on ships. Trans. Inst. Naval Archit. 39, 145–156.

Herzog, H.J., 2011. Scaling up carbon dioxide capture and storage: From megatons to gigatons. Energy Econ 33, 597–604. https://doi.org/10.1016/j.eneco.2010.11.004

Hesse, M.A., 2008. Mathematical modeling and multiscale simulation of carbon dioxide storage in saline aquifers. Stanford University.

Hilfer, R., Øren, P.E., 1996. Dimensional analysis of pore scale and field scale immiscible displacement. Transp Porous Media 22, 53–72.

Hill, S., 1952. Channeling in packed columns. Chem. Eng. Sc. 1, 247–253.

Holloway, S., 2005. Underground sequestration of carbon dioxide—a viable greenhouse gas mitigation option. Energy 30, 2318–2333. https://doi.org/10.1016/j.energy.2003.10.023

Homsy, G.M., 1987. Viscous fingering in porous media. Ann. Rev. Fluid Mech. 19, 271–311.

Hosseini, S.A., Lashgari, H., Choi, J.W., Nicot, J.-P., Lu, J., Hovorka, S.D., 2013. Static and dynamic reservoir modeling for geological CO2 sequestration at Cranfield, Mississippi, U.S.A. International Journal of Greenhouse Gas Control 18, 449–462. https://doi.org/10.1016/j.ijggc.2012.11.009

Hosseinzadeh Hejazi, S.A., Shah, S., Pini, R., 2019. Dynamic measurements of drainage capillary pressure curves in carbonate rocks. Chem Eng Sci 200, 268–284. https://doi.org/10.1016/j.ces.2019.02.002

Huang, D.D., Honarpour, M.M., 1998. Capillary end effects in coreflood calculations. J Pet Sci Eng 19, 103–117. https://doi.org/10.1016/S0920-4105(97)00040-5

IEA, 2022. World energy outlook 2022.

IEA, 2021. World Energy Outlook 2021.

IPCC, 2022. Climate Change 2022: Impacts, Adaptation and Vulnerability.

IPCC, 2018. Global Warming of 1.5 °C. An IPCC Special Report.

IPCC, 2005. Carbon Dioxide Capture and Storage.

IRENA, 2021. Renewable Energy Statistics 2021.

Jackson, S.J., Agada, S., Reynolds, C.A., Krevor, S., 2018. Characterizing Drainage Multiphase Flow in Heterogeneous Sandstones. Water Resour Res 54, 3139–3161. https://doi.org/10.1029/2017WR022282

Jackson, S.J., Krevor, S., 2020a. Small-Scale Capillary Heterogeneity Linked to Rapid Plume Migration During CO2 Storage. Geophys Res Lett 47. https://doi.org/10.1029/2020GL088616

Jackson, S.J., Krevor, S., 2020b. Small-Scale Capillary Heterogeneity Linked to Rapid Plume Migration During CO Storage. Geophys Res Lett 47. https://doi.org/10.1029/2020GL088616

Jacobson, M.Z., Delucchi, M.A., Cameron, M.A., Frew, B.A., 2015. Low-cost solution to the grid reliability problem with 100% penetration of intermittent wind, water, and solar for all purposes. Proceedings of the National Academy of Sciences 112, 15060–15065. https://doi.org/10.1073/pnas.1510028112

Jenkins, S., Millar, R.J., Leach, N., Allen, M.R., 2018. Framing Climate Goals in Terms of Cumulative CO2-Forcing-Equivalent Emissions. Geophys Res Lett 45, 2795–2804. https://doi.org/10.1002/2017GL076173

Jevons, W.S., 1857. On the cirrus form of cloud. Phil. Mag. J. Sc., 4th Series 14, 22–35.

Johnson, E.F., Bossler, D.P., Bossler, V.O.N., 1959. Calculation of Relative Permeability from Displacement Experiments. Transactions of the AIME 216, 370–372. https://doi.org/10.2118/1023-G

Juanes, R., Blunt, M.J., 2006. Analytical Solutions to Multiphase First-Contact Miscible Models with Viscous Fingering. Transp Porous Media 64, 339–373.

Juanes, R., MacMinn, C.W., Szulczewski, M.L., 2010. The Footprint of the CO2 Plume during Carbon Dioxide Storage in Saline Aquifers: Storage Efficiency for Capillary Trapping at the Basin Scale. Transp Porous Media 82, 19–30. https://doi.org/10.1007/s11242-009-9420-3

Juanes, R., Spiteri, E.J., Orr, F.M., Blunt, M.J., 2006. Impact of relative permeability hysteresis on geological CO2 storage. Water Resour Res 42. https://doi.org/10.1029/2005WR004806

Kampitsis, A.E., Kostorz, W.J., Muggeridge, A.H., Jackson, M.D., 2021. The life span and dynamics of immiscible viscous fingering in rectilinear displacements. Phys. Fluids 33, 96608.

Kaszuba, J.P., Janecky, D.R., 2009. Geochemical impacts of sequestering carbon dioxide in brine formations. pp. 239–247. https://doi.org/10.1029/2006GM000353

King, M.J., Dunayevsky, V.A., 1989. Why Waterflood Works: A Linearized Stability Analysis. Society of Petroleum Engineers SPE 19648, 187–200.

Kong, X., Delshad, M., Wheeler, M.F., 2015. History Matching Heterogeneous Coreflood of CO2/Brine by Use of Compositional Reservoir Simulator and Geostatistical Approach. SPE Journal 20, 267–276. https://doi.org/10.2118/163625-PA

Krause, M., Krevor, S., Benson, S.M., 2013. A Procedure for the Accurate Determination of Sub-Core Scale Permeability Distributions with Error Quantification. Transp Porous Media 98, 565–588. https://doi.org/10.1007/s11242-013-0161-y

Krause, M., Perrin, J.-C..-C., Benson, S.M.. M., 2011. Modeling Permeability Distributions in a Sandstone Core for History Matching Coreflood Experiments. SPE Journal 16, 768–777. https://doi.org/10.2118/126340-PA

Krause, M.H., Benson, S.M., 2015. Accurate determination of characteristic relative permeability curves. Adv Water Resour 83, 376–388. https://doi.org/10.1016/j.advwatres.2015.07.009

Krevor, S., Blunt, M.J., Benson, S.M., Pentland, C.H., Reynolds, C., Al-Menhali, A., Niu, B., 2015. Capillary trapping for geologic carbon dioxide storage – From pore scale physics to field scale implications. International Journal of Greenhouse Gas Control 40, 221–237. https://doi.org/10.1016/j.ijggc.2015.04.006

Krishnamurthy, P.G., DiCarlo, D., Meckel, T., 2022. Geologic Heterogeneity Controls on Trapping and Migration of CO2. Geophys Res Lett 49. https://doi.org/10.1029/2022GL099104

Krogstad, S., Lie, K., Møyner, O., Nilsen, H.M., Raynaud, X., Skaflestad, B., 2015. MRST-AD–an open-source framework for rapid prototyping and evaluation of reservoir simulation problems, in: SPE Reservoir Simulation Conference? SPE, p. D022S002R004.

Kumbhare, S., Shahmoradi, A., 2020. MatDRAM: A pure-MATLAB Delayed-Rejection Adaptive Metropolis-Hastings Markov Chain Monte Carlo Sampler. arXiv preprint arXiv:2010.04190.

Kuo, C.-W., Benson, S.M., 2015. Numerical and analytical study of effects of small scale heterogeneity on CO2/brine multiphase flow system in horizontal corefloods. Adv Water Resour 79, 1–17. https://doi.org/10.1016/j.advwatres.2015.01.012

Kuo, C.-W., Perrin, J.-C., Benson, S.M., 2011. Simulation studies of effect of flow rate and small scale heterogeneity on multiphase flow of CO2 and brine. Energy Procedia 4, 4516–4523. https://doi.org/10.1016/j.egypro.2011.02.408

Kurotori, T., Pini, R., 2021. A general capillary equilibrium model to describe drainage experiments in heterogeneous laboratory rock cores. Adv Water Resour 152, 103938. https://doi.org/10.1016/j.advwatres.2021.103938

Lake, L.W., Johns, R., Rossen, B., Pope, G.A., 2014. Fundamentals of enhanced oil recovery. Society of Petroleum Engineers Richardson, TX.

Lanza, F., Sinha, S., Hansen, A., Rosso, A., Talon, L., 2023. Transition from viscous fingers to foam during drainage in heterogeneous porous media. arXiv preprint arXiv:2307.13451.

Lenormand, R., Lorentzen, K., Maas, J.G., Ruth, D., 2017. Comparison of four numerical simulators for SCAL experiments. Petrophysics 58, 48–56.

Lenormand, R., Touboul, E., Zarcone, C., 1988. Numerical models and experiments on immiscible displacements in porous media. J Fluid Mech 189, 165–187.

Leverett, M.C., 1941. Capillary Behavior in Porous Solids. Transactions of the AIME 142, 152–169. https://doi.org/10.2118/941152-G

Lewis, D.J., 1949. The instability of liquid surfaces when accelerated in a direction perpendicular to their planes. II. Proc. R. Soc. Lond. A 202, 81–96.

Lie, K.-A., 2019. An introduction to reservoir simulation using MATLAB/GNU Octave: User guide for the MATLAB Reservoir Simulation Toolbox (MRST). Cambridge University Press.

Liu, Y., Lv, P., Liu, Y., Jiang, L., Tetsuya, S., Song, Y., Wu, B., Liu, S., 2016. CO_2/water two-phase flow in a two-dimensional micromodel of heterogeneous pores and throats. RSC Adv. 6, 73897--73905.

Loeve, D., Wilschut, F., Hanea, R.H., Maas, J.G., Van Hooff, P.M.E., van den Hoek, P.J., Douma, S.G., Van Doren, J.F.M., 2011. Simultaneous determination of relative permeability and capillary pressure curves by assisted history matching several SCAL experiments, in: Society of Core Analysis Conference Paper SCA2011-35. pp. 1–12.

Lomeland, F., Ebeltoft, E., Thomas, W.H., 2005. A new versatile relative permeability correlation, in: International Symposium of the Society of Core Analysts, Toronto, Canada.

Lu, J., Kordi, M., Hovorka, S.D., Meckel, T.A., Christopher, C.A., 2013. Reservoir characterization and complications for trapping mechanisms at Cranfield CO2 injection site. International Journal of Greenhouse Gas Control 18, 361–374. https://doi.org/10.1016/j.ijggc.2012.10.007

Lucas, R., 1918. Ü"ber das Zeitgesetz des Kapillaren Aufstiegs von Flü"ssigkeiten. Kolloid Z. 23, 15–22.

Maas, J.G., Flemisch, B., Hebing, A., 2011. Open source simulator DuMux available for SCAL data interpretation, in: SCA. p. 2011.

Maas, J.G., Schulte, A.M., 1997. Computer simulation of Special Core Analysis (SCAL) flow experiments shared on the Internet, in: SCA-9719 Presented at the SCA 1997 Conference, Calgary, Canada. p. 92.

Maas, J.G., Springer, N., Hebing, A., 2019. Defining a sample heterogeneity cut-off value to obtain representative Special Core Analysis (SCAL) measurements, in: International Symposium of the Society of Core Analysts Held in Pau, France. pp. 26–30.

Maas, J.G., Springer, N., Hebing, A., Berg, S., 2022. Displacement stability revisited – A new criterion for the onset of viscous fingering., in: International Symposium of the Society of Core Analysts Held in Austin, Texas, USA, 19–22 September.

Maas, J.G., Springer, N., Hebing, A., Snippe, J., Berg, S., 2023. A General Criterion for Viscous Fingering in Porous Media. J Fluid Mech under review.

Matsuura, T., Stoll, W.M., van Batenburg, D.W., van Wunnik, J.N.M., Boerrigter, P.M., 2013. Modelling of ASP Flooding Using X-ray CT Core Flooding Experiments, in: IOR 2015 - 18th European Symposium on Improved Oil Recovery, Apr 2015, Cp-445-00057. p. cp-445-00057.

McPhee, C., Reed, J., Zubizarreta, I., 2015a. Best Practice in Coring and Core Analysis. pp. 1–15. https://doi.org/10.1016/B978-0-444-63533-4.00001-9

McPhee, C., Reed, J., Zubizarreta, I., 2015b. Core analysis: a best practice guide. Elsevier.

Metz, Bert, Davidson, O., De Coninck, H., Loos, M., Meyer, L., others, 2005. Intergovernmental Panel on Climate Change (IPCC) special report on carbon dioxide capture and storage. Cambridge, United Kingdom and New York, NY.

Metz, B, Davidson, O., de Coninck, H.C., Loos, M., Meyer, L.A. (Eds.), 2005. IPCC—Intergovernmental Panel on Climate Change, in: Special Report on Carbon Dioxide Capture and Storage. Cambridge University Press, Cambridge, UK and New York, NY, USA.

Michael, K., Golab, A., Shulakova, V., Ennis-King, J., Allinson, G., Sharma, S., Aiken, T., 2010. Geological storage of CO2 in saline aquifers—A review of the experience from existing storage operations. International Journal of Greenhouse Gas Control 4, 659–667. https://doi.org/10.1016/j.ijggc.2009.12.011

Mostaghimi, P., Kamali, F., Jackson, M.D., Muggeridge, A.H., Pain, C.C., 2016. Adaptive mesh optimization for simulation of immiscible viscous fingering. SPE Journal 21, 2250–2259.

Ni, H., Boon, M., Garing, C., Benson, S.M., 2019. Predicting CO2 residual trapping ability based on experimental petrophysical properties for different sandstone types. International Journal of Greenhouse Gas Control 86, 158–176. https://doi.org/10.1016/j.ijggc.2019.04.024

Nicolaeides, C., Jha, B., Cueto-Felgueroso, L., Juanes, R., 2015. Impact of viscous fingering and permeability heterogeneity on fluid mixing in porous media. Water Resour Res 51, 2634–2647. https://doi.org/10.1002/2014WR015811

Nijjer, J.S., Hewitt, D.R., Neufeld, J.A., 2018. The dynamics of miscible viscous fingering from onset to shutdown. J Fluid Mech 837, 520–545. https://doi.org/10.1017/jfm.2017.829

Novy, R.A., Toledo, P.G., Davis, H.T., Scriven, L.E., 1989. Capillary Dispersion in Porous Media at Low Wetting Phase Saturation. Chem Eng Sci 44, 1785–1798.

Onoja, M.U., Shariatipour, S.M., 2019. Assessing the impact of relative permeability and capillary heterogeneity on Darcy flow modelling of CO2 storage in Utsira Formation. Greenhouse Gases: Science and Technology 9, 1221–1246. https://doi.org/10.1002/ghg.1932

Ott, H., 2023. Carbon Capture and Storage (CCS). CCCA Fact Sheet #43.

Ott, H., 2015. CO2-brine primary displacement in saline aquifers: experiments, simulations and concepts. Habilitationsschrift, RWTH Aachen.

Ott, H., de Kloe, K., van Bakel, M., Vos, F., van Pelt, A., Legerstee, P., Bauer, A., Eide, K., van der Linden, A., Berg, S., Makurat, A., 2012. Core-flood experiment for transport of reactive fluids in rocks. Review of Scientific Instruments 83, 084501. https://doi.org/10.1063/1.4746997

Ott, H., Pentland, C.H., Oedai, S., 2015. CO 2 –brine displacement in heterogeneous carbonates. International Journal of Greenhouse Gas Control 33, 135–144. https://doi.org/10.1016/j.ijggc.2014.12.004

Pearson, K., 1895. VII. Note on regression and inheritance in the case of two parents. Proceedings of the Royal Society of London 58, 240–242. https://doi.org/10.1098/rspl.1895.0041

Pini, R., Benson, S.M., 2013a. Simultaneous determination of capillary pressure and relative permeability curves from core-flooding experiments with various fluid pairs. Water Resour Res 49, 3516–3530. https://doi.org/10.1002/wrcr.20274

Pini, R., Benson, S.M., 2013b. Characterization and scaling of mesoscale heterogeneities in sandstones. Geophys Res Lett 40, 3903–3908. https://doi.org/10.1002/grl.50756

Pini, R., Krevor, S.C.M., Benson, S.M., 2012. Capillary pressure and heterogeneity for the CO2/water system in sandstone rocks at reservoir conditions. Adv Water Resour 38, 48–59. https://doi.org/10.1016/j.advwatres.2011.12.007

Prores, n.d. Sendra.

R. H. Brooks and A. T. Corey, 1964. Hydraulic Properties of Porous Media and Their Relation to Drainage Design. Transactions of the ASAE 7, 0026–0028. https://doi.org/10.13031/2013.40684

Rayleigh, Lord, 1883. Investigation of the character of equilibrium of an incompressible heavy fluid of variable density. Proc. Lond. Math. Soc. 14, 170–177.

Renard, Ph., de Marsily, G., 1997. Calculating equivalent permeability: a review. Adv Water Resour 20, 253–278. https://doi.org/10.1016/S0309-1708(96)00050-4

Reynolds, C.A., Blunt, M.J., Krevor, S., 2018. Multiphase Flow Characteristics of Heterogeneous Rocks From CO2 Storage Reservoirs in the United Kingdom. Water Resour Res 54, 729–745. https://doi.org/10.1002/2017WR021651

Reynolds, C.A., Krevor, S., 2015. Characterizing flow behavior for gas injection: Relative permeability of CO2-brine and N2-water in heterogeneous rocks. Water Resour Res 51, 9464–9489. https://doi.org/10.1002/2015WR018046

Riaz, A., Tchelepi, H.A., 2006. Numerical simulation of immiscible two-phase flow in porous media. Phys. Fluids 18, 14104.

Riaz, A., Tchelepi, H.A., 2004. Linear stability analysis of immiscible two-phase flow in porous media with capillary dispersion and density variation. Phys. Fluids 16, 4727–4737.

Ringrose, P.S., Sorbie, K.S., Corbett, P.W.M., Jensen, J.L., 1993. Immiscible flow behaviour in laminated and cross-bedded sandstones. J Pet Sci Eng 9, 103–124. https://doi.org/10.1016/0920-4105(93)90071-L

Rochelle, G.T., 2009. Amine Scrubbing for CO2 Capture. Science (1979) 325, 1652–1654. https://doi.org/10.1126/science.1176731

Rücker, M., Georgiadis, A., Armstrong, R.T., Ott, H., Brussee, N., van der Linde, H., Simon, L., Enzmann, F., Kersten, M., Berg, S., 2021. The Origin of Non-thermal Fluctuations in Multiphase Flow in Porous Media. Frontiers in Water 3. https://doi.org/10.3389/frwa.2021.671399

Ruspini, L.C., Øren, P.E., Berg, S., Masalmeh, S., Bultreys, T., Taberner, C., Sorop, T., Marcelis, F., Appel, M., Freeman, J., Wilson, O.B., 2021. Multiscale Digital Rock

Analysis for Complex Rocks. Transp Porous Media 139, 301–325. https://doi.org/10.1007/s11242-021-01667-2

Rutqvist, J., 2012. The Geomechanics of CO2 Storage in Deep Sedimentary Formations. Geotechnical and Geological Engineering 30, 525–551. https://doi.org/10.1007/s10706-011-9491-0

Saffmann, P.G., Taylor, G., 1958. The penetration of a fluid into a porous medium or Hele-Shaw cell containing a more viscous liquid. Proc. R. Soc. Lond. A B56, 312–329.

Salmo, I.C., Sorbie, K.S., Skauge, A., Alzaabi, M.A., 2022. Immiscible Viscous Fingering: Modelling Unstable Water–Oil Displacement Experiments in Porous Media. Transp Porous Media 145, 291–322.

Salmo, I.C., Zamani, N., Skauge, T., Sorbie, K., Skauge, A., 2020. Use of dynamic pore network modeling to improve our understanding of experimental observations in viscous oil displacement by polymers. SPE J.

Schmid, K.S., Geiger, S., 2012. Universal scaling of spontaneous imbibition for water-wet systems. Water Resour Res 48, WR03507.

Shahmoradi, A., Bagheri, F., 2020. Paradram: A cross-language toolbox for parallel high-performance delayed-rejection adaptive metropolis markov chain monte carlo simulations. arXiv preprint arXiv:2008.09589.

Shell Inernational Limited, 2023. The Energy Security Scenarios.

Shell scenarios, 2023. The Energy Security Scenarios.

Sintef, 2023. MRST Download Page [WWW Document]. URL https://www.sintef.no/projectweb/mrst/download/ (accessed 10.26.23).

Skjaeveland, S.M., Siqveland, L.M., Kjosavik, A., Thomas, W.L.H., Virnovsky, G.A., 2000. Capillary Pressure Correlation for Mixed-Wet Reservoirs. SPE Reservoir Evaluation & Engineering 3, 60–67. https://doi.org/10.2118/60900-PA

Smil, V., 2018. Energy and civilization: a history. MIT press.

Smith, J.E., Zhang, Z.F., 2001. Determining effective interfacial tension and predicting finger spacing for DNAPL penetration into water-saturated porous media. J Contam Hydrol 48, 167–183.

Sorbie, K.S., Al Ghafri, A.Y., Skauge, A., Mackay, E.J., 2020. On the modelling of immiscible viscous fingering in two-phase flow in porous media. Transp Porous Media 135, 331–359.

Span, R., Wagner, W., 1996. A New Equation of State for Carbon Dioxide Covering the Fluid Region from the Triple-Point Temperature to 1100 K at Pressures up to 800 MPa. J Phys Chem Ref Data 25, 1509–1596. https://doi.org/10.1063/1.555991

Stokes, J.P., Weitz, D.A., Gollub, J.P., Dougherty, A., Robbins, M.O., Chaikin, P.M., Lindsay, H.M., 1986. Interfacial stability of immiscible displacement in a porous medium. Phys Rev Lett 57, 1718.

Tan, C.-T., Homsy, G.M., 1992. Viscous fingering with permeability heterogeneity. Physics of Fluids A: Fluid Dynamics 4, 1099–1101. https://doi.org/10.1063/1.858227

Taylor, G., 1949. The instability of liquid surfaces when accelerated in a direction perpendicular to their planes. I. Proc. R. Soc. Lond. A 201, 192–196.

Tchelepi, H.A., Orr, F.M., Rakotomalala, N., Salin, D., Woumeni, R., 1993. Dispersion, permeability heterogeneity, and viscous fingering: Acoustic experimental observations and particle-tracking simulations. Physics of Fluids A: Fluid Dynamics 5, 1558–1574. https://doi.org/10.1063/1.858833

Toledo, P.G., Novy, R.A., Davis, H.T., Scriven, L.E., 1994. Capillary Pressure, Water Relative Permeability, Electrical Conductivity and Capillary Dispersion Coefficient of Fractal Porous Media at Low Wetting Phase Saturations. SPE Advanced Technology Series 2, 136–141.

Trevisan, L., Pini, R., Cihan, A., Birkholzer, J.T., Zhou, Q., González-Nicolás, A., Illangasekare, T.H., 2017. Imaging and quantification of spreading and trapping of carbon dioxide in saline aquifers using meter-scale laboratory experiments. Water Resour Res 53, 485–502. https://doi.org/10.1002/2016WR019749

UNFCCC, 2015. Paris Agreement.

United Nations, 2023. United Nations Website [WWW Document]. Retrieved from https://www.un.org/en/.

Wang, Y., Zhang, C., Wei, N., Oostrom, M., Wietsma, T.W., Li, X., Bonneville, A., 2013. Experimental study of Crossover from Capillary to Viscous Fingering for Supercritical CO_2-Water Displacement in a Homogeneous Pore Network. Environ Sci Technol 47, 212–218.

Washburn, E.W., 1921. The Dynamics of Capillary Flow. Physical Review 17, 273.

Wellington, S.L., Vinegar, H.J., 1987. X-ray computerized tomography 39:8. https://doi.org/10.2118/16983-PA

Wenck, N., Jackson, S.J., Manoorkar, S., Muggeridge, A., Krevor, S., 2021. Simulating Core Floods in Heterogeneous Sandstone and Carbonate Rocks. Water Resour Res 57. https://doi.org/10.1029/2021WR030581

Wildenschild, D., Sheppard, A.P., 2013. X-ray imaging and analysis techniques for quantifying pore-scale structure and processes in subsurface porous medium systems. Adv Water Resour 51, 217–246. https://doi.org/10.1016/j.advwatres.2012.07.018

Williams, G.A., Chadwick, R.A., Vosper, H., 2018. Some thoughts on Darcy-type flow simulation for modelling underground CO_2 storage, based on the Sleipner CO_2 storage operation. International Journal of Greenhouse Gas Control 68, 164–175.

World Energy Council, 2019. World Energy Scenarios.

Yergin, D., 2012. The quest: Energy, security, and the remaking of the modern world. Penguin.

Yortsos, Y.C., Hickernell, F.J., 1989. Linear stability of immiscible displacement in porous media. SIAM J Appl Math 49, 730–748.

Yortsos, Y.C., Hunag, A.B., 1986. Linear-Stability Analaysis of Immiscible Displacement: Part 1 - Simple Basic Flow Profiles. SPE Reservoir Engineering 1, 378–390.

ZER, 2011. The cost of subsurface storage of CO2.

Zhang, C., Oostrom, M., Grate, J.W., Wietsma, T.W., Warner, M.G., 2011. Liquid CO2 Displacement of Water in a Dual-Permeability Pore Network Micromodel. Environ Sci Technol 45, 7581–7588. https://doi.org/10.1021/es201858r

Zhang, D., Zhang, R., Chen, S., Soll, W.E., 2000. Pore scale study of flow in porous media: Scale dependency, REV, and statistical REV. Geophys Res Lett 27, 1195–1198. https://doi.org/10.1029/1999GL011101

Zhao, B., MacMinn, C.W., Juanes, R., 2016. Wettability control on multiphase flow in patterned microfluidics. PNAS 113, 10251--10256.

Appendix A

Appendix A: Parameters of the SCAL Benchmarks

This appendix provides the input parameters used in the benchmarking simulations discussed in Chapter 2. These benchmarks helped verify the accuracy of the SCAL interpreter module developed in this work. The parameters correspond to the synthetic data sets published by (Lenormand et al., 2017) and (Loeve et al., 2011).

1. Forward Simulation Benchmarks

Table 2 list the relative permeability and capillary pressure input parameters that were used to generate the synthetic data for verifying the forward simulations. Case 1 refers to primary imbibition while Case 5 represents primary drainage. The simulated pressure differential and average water saturation data were then compared to results from the SCORES simulator as shown in Figure 11 in chapter 3.

Table 3: Properties of samples and fluids used for the verification simulations (Lenormand et al., 2017).

		case 1	case 2	case 3	case 4	case 5
Type of experiment		SS + bumps	SS + bumps	USS	USS	centrifuge
Type of displacement		imbibition	imbibition	imbibition	imbibition	primary drainage
Disposition		horizontal	horizontal	horizontal	horizontal	

Length	cm	8	8	8	8	10
Diameter	cm	4	4	4	4	4
Base permeability	mD	100	100	100	100	100
Porosity	frac	0.25	0.25	0.25	0.25	0.25
Water viscosity	cP	1	1	1	1	1
Water density	g/cm3	1	1	1	1	1
Oil viscosity	cP	5	5	5	1	5
Oil density	g/cm3	0.8	0.8	0.8	0.8	0.8
Initial S_w	frac	0.2	0.2	0.2	0.2	1
Final S_w	frac	0.8	0.8	0.8	0.8	0.3
$k_{rw\,max}$	frac	0.5	0.5	0.5	0.5	1
$k_{ro\,max}$	frac	0.5	0.5	0.5	0.5	1
Corey exponent water		3	3	3	3	3
Corey exponent oil		3	3	3	3	2
P_c curve		Pc smooth	Pc sharp	Pc smooth	Pc = 0	Pc centrifuge

2. History Match Benchmarks

Table 4 to Table 6 provide the relative permeability and capillary pressure parameters used to generate the synthetic unsteady-state and centrifuge data for history matching. The interpreted parameters are shown in Figure 12 of Chapter 3.

Table 4: Core and fluid properties for the synthetic history match cases (Loeve et al., 2011)

Property	Value

Core length (cm)	6.0
Core cross-sect. area (cm^2)	11.4
Absolute permeability (mD)	500
Porosity (-)	0.3
Oil density (kg/m^3)	730
Water density (kg/m^3)	1000
Oil viscosity (cP)	1.0
Water viscosity (cP)	1.0
Initial water saturation	0.29

Table 5: Values of the parameters used to describe the relative permeability and capillary pressure curves for the synthetic history match cases (Loeve et al., 2011)

Parameter	"Truth"Value	Parameter Range		Initial guess	History match results
Relative permeability		Min	Max		
Connate water saturation – S_{wc} (-)	0.15	0.05	0.25	0.084	0.137291
Residual oil saturation – S_{or} (-)	0.20	0.05	0.25	0.1780	0.199262
Water rel. perm. at Sor – kwor (-)	0.50	0.10	0.70	0.2039	0.510343
Oil rel. perm. at S_{wc} – k_{owc} (-)	0.50	0.10	0.70	0.4018	0.551668
Corey exponent oil – no (-)	5	2.00	6.00	5.026	5.044836
Corey exponent water – nw (-)	3	2.00	6.00	2.8525	3.065446
Capillary pressure – param. 2					
Water amplitude – cwi (bar)	0.319	0.001	0.600	0.04	0.270554

Oil amplitude – coi (bar)	-0.012	-0.60	-0.001	-0.038	-0.01829
Water domain saturation – Swd (-)	0.400	0.30	0.42	0.4	0.42
Oil domain saturation – Sod (-)	0.650	0.60	0.68	0.61	0.677606
Linear domain offset bi (bar)	0.0853	-0.15	+0.15	-0.073	0.074187
Linear domain slope ri (bar/-)	-0.2408	-0.5	-0.01	-0.49	-0.224

Table 6: Experimental design of centrifuge experiment (Loeve et al., 2011)

Time	Centrifugal accelerations
hour	$\frac{m}{s^2}$
0	-741
4	-1480
8	-2220
14	-4000
38	-6000
62	-8000
86	-10000
110	Time of the last measurement

Appendix B

Appendix B: SCAL Interpretation Tool Interface User Manual
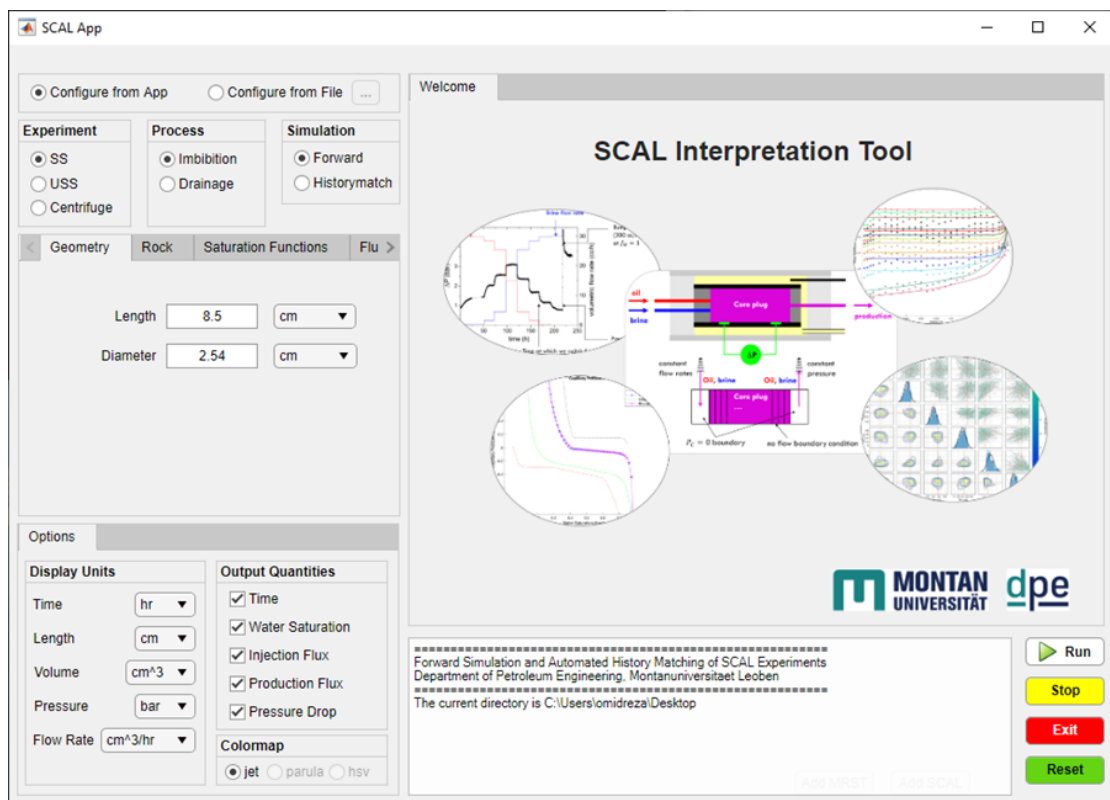
Figure 30: Main interface of the SCAL simulation tool developed at MUL

6.1 App Configuration

To start configuring the app and your simulations there are two options to start from. The simulation can be either configured from the app interface or from a configuration text file.

To configure the app from the app interface, choose "Configure from App" as below:
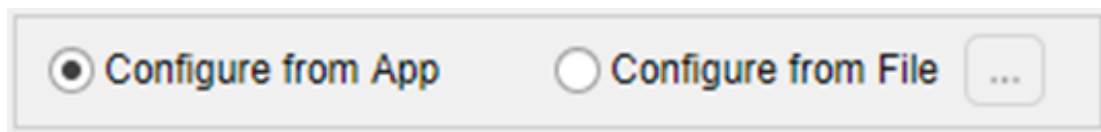
Figure 31: Ratio buttons to configure the app either from the interface or from a settings file

To configure the app from the configuration file, choose "Configure from File" and then using the button with three dots, choose the path of the configuration file. This file should have a *.txt format.

The configuration file needs to have a predefined format. Please check the provided template to see how the format needs to be. Missing elements or using wrong keywords for this configuration file can cause errors for the app.

6.1.1 Configuring from the app

First, there is the option to choose the type of the experiment, process, and then the simulation type. They can be chosen using the menu shown below:

Figure 32: Simulation options available in the simulator interface

6.2   Forward Simulations

There are several tabs under this menu for the user to input the required parameters for the forward simulation. It is recommended to fill in the input parameters in the sequence of the input tabs.

6.2.1 Geometry, Rock and Fluid

The first tab is Geometry and after that is the Rock tab. Here the dimensions and the rock properties of the core can be input. The corresponding units can also be selected from the drop-down list in front of each text box.

The fluid tab is placed after the saturation functions tab and has a similar structure to the geometry and rock tabs.

Figure 33: Input panels for rock and fluid parameters

6.2.2 Saturations Functions

Next there is the "Saturation Functions" tab to input the relative permeability and capillary pressure as a function of water saturation. These parameters can either be input as a table or inform of the provided correlations.

To input a table, first create a *.txt file according to the provided templates and then choose this file using the button with three dots. The input table can be checked and modified, using the "Show" button.

To input a correlation, select the "Correlation" radio button and the input window for the correlation parameters will pop up. Fill in the correct parameters and click the "Done" button. The input relative permeability or capillary pressure can be plotted using the "Plot Kr" and "Plot Pc" buttons. An example of a relative permeability plot is shown below:
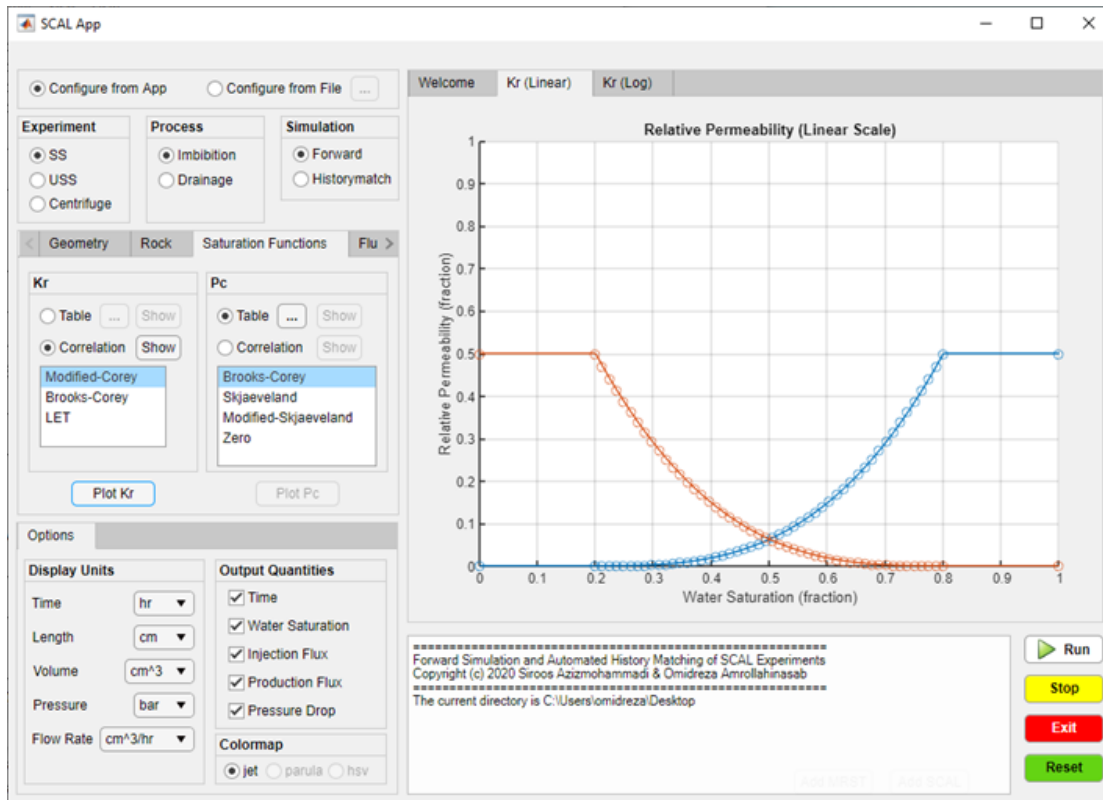
Figure 34: Saturation function input and plotting functions of the simulator

6.2.3 Simulation Setup

Here the number of the grid cells to run the simulations and the time steps can be identified. Please note that they both influence the accuracy of the results and can make your computational cost to go higher. However, the computational cost of choosing a small time-step is usually bigger than having many cells. The recommended range for the number of the cells is between 20 to 500 and for the time step it is from 30 seconds to 1 hour.

There is an option called "Gauge Off" and it can be activated by choosing the check box. when this value is deactivated or it is set to zero, the calculated pressure is the pressure difference at both ends of the core. In case one wants to calculate the pressure difference at a certain distance from each end of the core, this distance can be defined by the gauge off value.

To capture the capillary pressure end effect, there is an option provided called "Boundary Cells" and it is by default activated. Based on the number in the text box in front of it, there are cells created at each end of the core, with zero capillary pressure and linear relative permeability to simulate the capillary end effects. The initial water saturations for these boundary cells are recommended to be set to zero for an imbibition simulation and one for a drainage simulation.

Figure 35: Input panel to choose the number of the grid cells and the time steps of the simulator

6.2.4 Schedule

Here the flooding schedule for steady state and unsteady state, or the centrifuge rpm schedule can be input using a *.txt with the correct format from the templates. In case that a centrifuge is chosen from the experiment radio button group, centrifuge startup and centrifuge center distance options are activated. Please note that the Ambient pressure here means the pressure at the outlet of the core.

Figure 36: Input panel for the schedule or injection/production settings of the simulator

6.2.5 Observations

In the observations tab, the experimental measurements can be input using the correct *.txt file format from the templates. These observations will be plotted along with the simulation results after the simulation is done.

Regarding the saturation profile, there needs to be an excel file provided. In this excel file the first row is the location along the core in meters and the first column is the recording time in seconds. (please check the template)
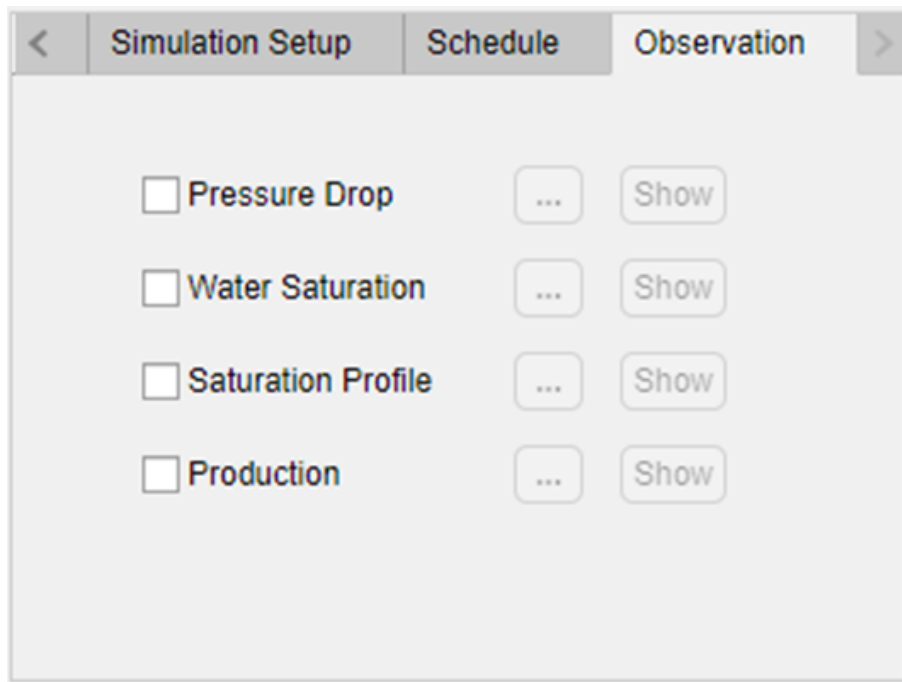
Figure 37: Input panel for the experimental data for comparison and history matching modules

6.2.6 Options

In this tab the units in which the plots will be shown can be input. Also, the quantities which the user would like to have as an output can be chosen from here.

Figure 38: Different plotting options in terms of output quantities and output units

6.3   History matching

To run a history match simulation, first fill in the input parameters as explained for the forward simulation. For the relative permeability and capillary pressure, input your best guess which can be the analytical solution of the experimental measurements.

In case the history match option is selected in the simulation pane, the "History Match" tab will open. Here first there is the option to choose which parameter we would like to history match namely, relative permeability or capillary pressure or both. Usually, relative permeability is history matched with a flooding experiment and the capillary pressure with a centrifuge experiment. History matching both parameters at the same time is only recommended in the case that the user is doing simultaneous simulation of a flooding experiment and a centrifuge experiment.

After activating a parameter for history matching by checking the corresponding check box, the method choice panel will be enabled. Here the method or the correlation to run the history matching can be selected. Afterwards the excel file which is complying with the format of the provided templates can be input using the "Import initial points and boundaries" button. Please note that each method and each combination of methods has a separate template therefore case must be taken in choosing the right template. After importing the excel sheet it can be viewed using the "Show the imported table" button.

Using the check box called "Random multistarting points" there comes the option to initialize the history matching using several random points within the boundaries. This comes useful

when the history matching gets stuck in local minimums but usually it does not happen if the initial point is set to the analytical solution. The number of these random points to start from can be entered in the text box in front of it.

"Use parallel computing" check box is for running the history matching simulation on parallel on the CPU cores for faster simulations.

"Scale the problem" check box is used for scaling the input parameters which leads to a more efficient history matching simulation.

"Optimality tolerance" is the minimum difference between the objective function values before the optimization problem finds its solution.

"Max function evaluations" is the maximum number of the times that the optimization algorithm runs the forward simulations (in case of simultaneous history matching, each evaluation consists of two forwards simulations).

"Step tolerance" is the minimum step that the optimization algorithm will take before finding the minimum of the objective function.

To run a simultaneous history matching of a flooding and a centrifuge experiment, activating the check box and select the centrifuge configuration file using the button under the corresponding check box. Please note that to run such a simulation, the history matching part of the configuration file for the centrifuge experiment needs to be the same as the flooding experiment.

After the history matching is done, the results are saved in numbers in the input excel template, and they can be plotted using the "Plot resulting Kr & Pc" button. The observations can be compared using the "Compare history match results with data" button".

Figure 39: Input panel for history matching simulations

6.3.1 Message Box and Control Buttons

At the bottom right of the app there is a message box which shows what the app is currently doing and provided a report of the steps taken. After the input parameters for the simulation is set, the simulation can be run using the "Run" button and stopped using the "Stop" button.

To make a new simulation using new settings it is recommended to first reset the app using the green "Reset" button.

Figure 40: Messaging output log of the simulator

Appendix C

Appendix C: Sensitivity Analysis in 3D Core Simulations

Introduction

The sensitivity analysis was initiated with a foundational base case, inspired by the decane-brine experiment conducted on the lengthy core Estaillades Carbonate. The core dimensions are 15 cm in length and a diameter of 7.5 cm. For the base scenario, the core porosity was determined to be 29.7%, with a permeability value of 260 mD. The utilized fluids comprise brine (viscosity: 0.576 cp; density: 1001.2 kg/m^3) and decane (viscosity: 0.619 cp; density: 707.3 kg/m^3). It is imperative to acknowledge that gravity's influence is not considered in this analysis. The grid size selected was 34x17x17 (or 34x17x17 inclusive of boundary cells at both core ends). The choice in grid sizing was ascertained post examination of the saturation profile images derived from the experimental data.

6.4   Simulations Setup

Both the relative permeability and capillary pressure curve choices were anchored in the successful history match achieved with heterogeneous simulations on Estaillades Carbonate in Figure 23. The Generalized Corey model parameterized the relative permeability, while the Brooks-Corey model was employed for the capillary pressure curve.

Outcomes from the base case, including pressure, production, and saturation profiles, are earmarked for contrasting results with alternative cases. Fluid injection was carried out over a span of 10 hours at a rate of 0.25 ml/minute, simulated across 25-time steps.

6.5   Verification of the 3D Simulations

We sought to authenticate the integrity of our 3D simulation implementation by juxtaposing the results with those from the 1D simulations. Both relative permeability and capillary pressure values remained consistent. Consecutive figures illustrate identical outcomes for both the 1D and 3D cases under analogous conditions. These comparisons validate the reliability of the 3D results. Base case simulation predictions are exhibited for further comparison.
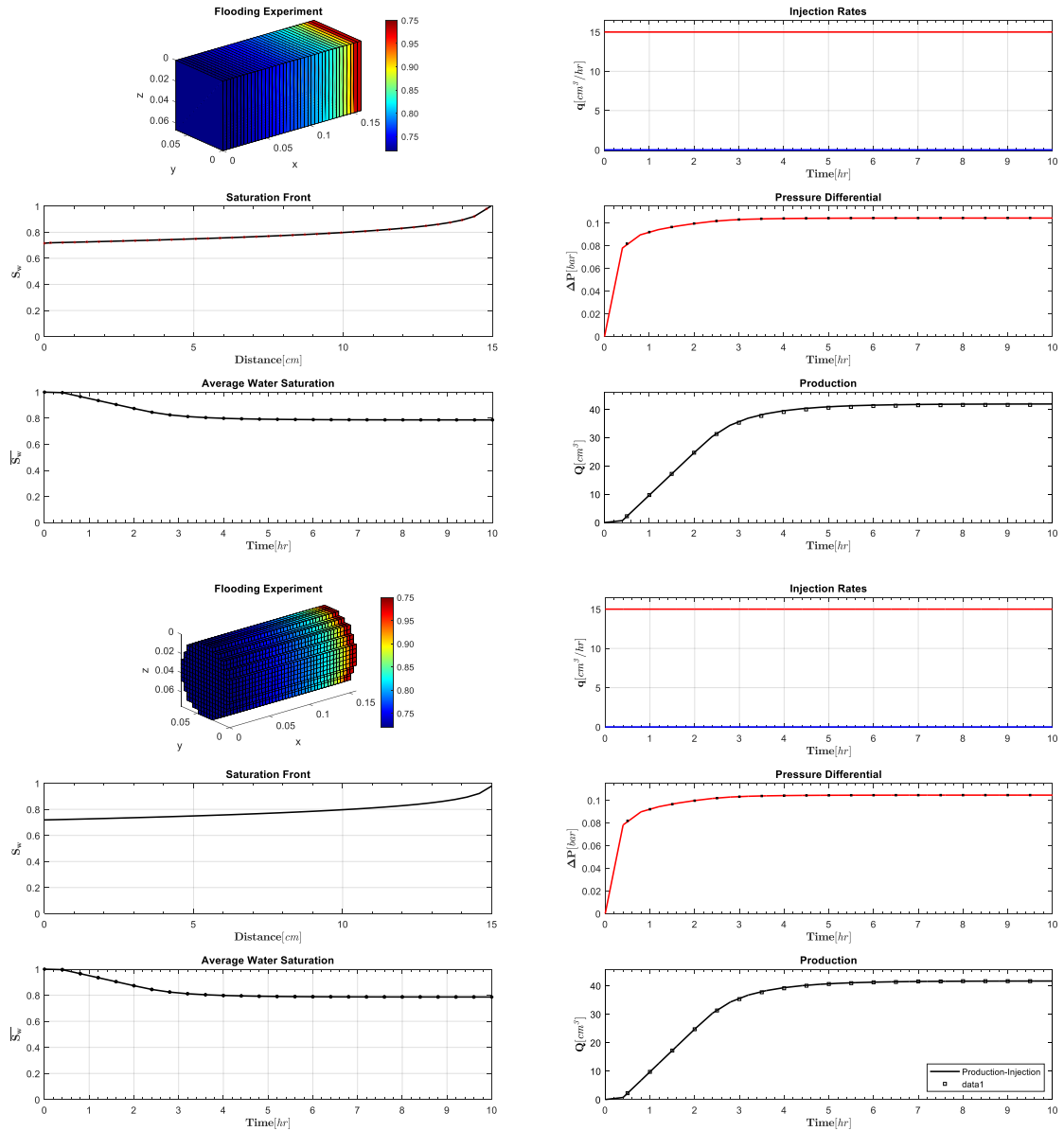
Figure 41: verifying that the 3D and 1D simulations result in the same results using and there are no numerical artifacts in between.

6.6   Sensitivity Analysis to Layering

In this section we aim to investigate the effect of different layering systems in terms of porosity, permeability and capillary scaling on the saturation profile calculated by the simulator to form a better understanding of the 3D heterogeneous simulations done in section 4.2.

1. Base Case: It features uniformly spread porosity and permeability fields with parameters explained in the beginning of the chapter.
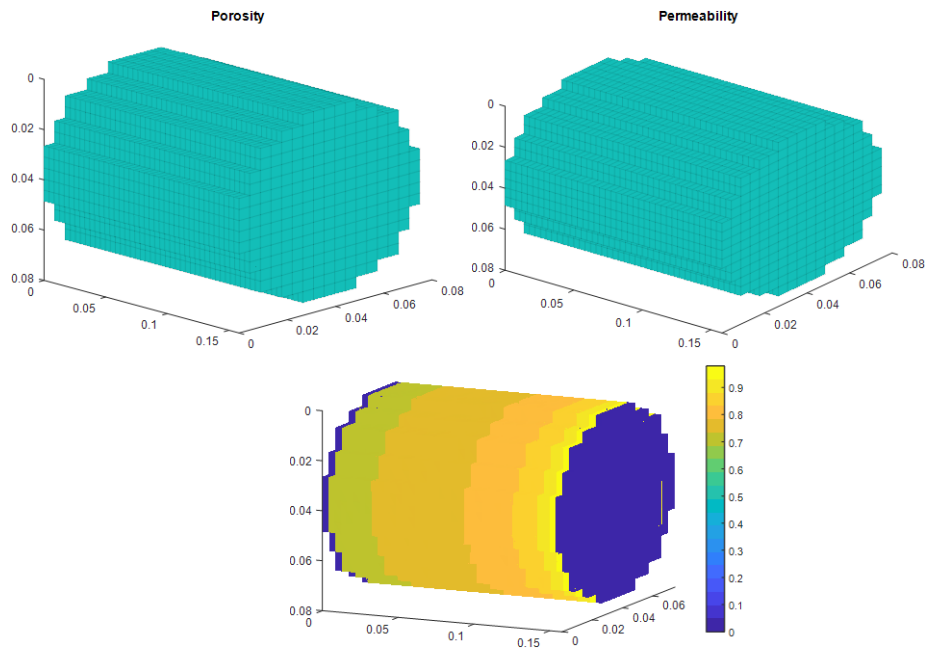
Figure 42: Permeability, Porosity and Saturation profile of the base case

2. Two Layers – Double Permeability: The top layer's permeability is doubled, maintaining a constant porosity. Initial advancement is faster atop the core, but post stabilization, a piston-like displacement is observed. This case displayed diminished production and pressure compared to the base case.
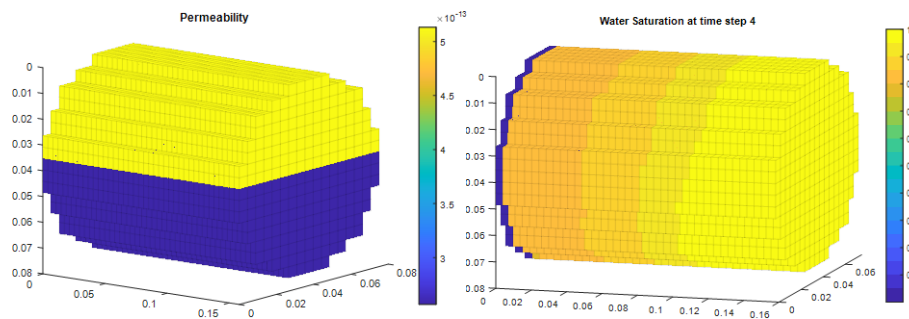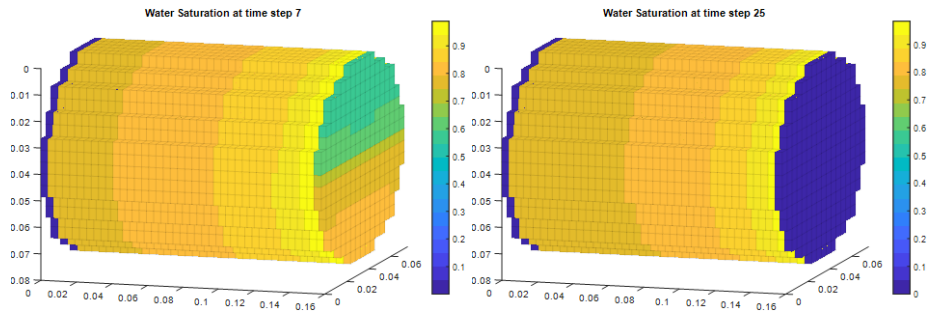
Figure 43: Permeability, Porosity and Saturation profile of the Two Layers – Double Permeability case

3. Two Layers – Double Porosity: Only the top layer's porosity is doubled. The shock front in the less porous layer accelerates prior to breakthrough, indicating contrasting impacts of permeability and porosity on the shock front's velocity.
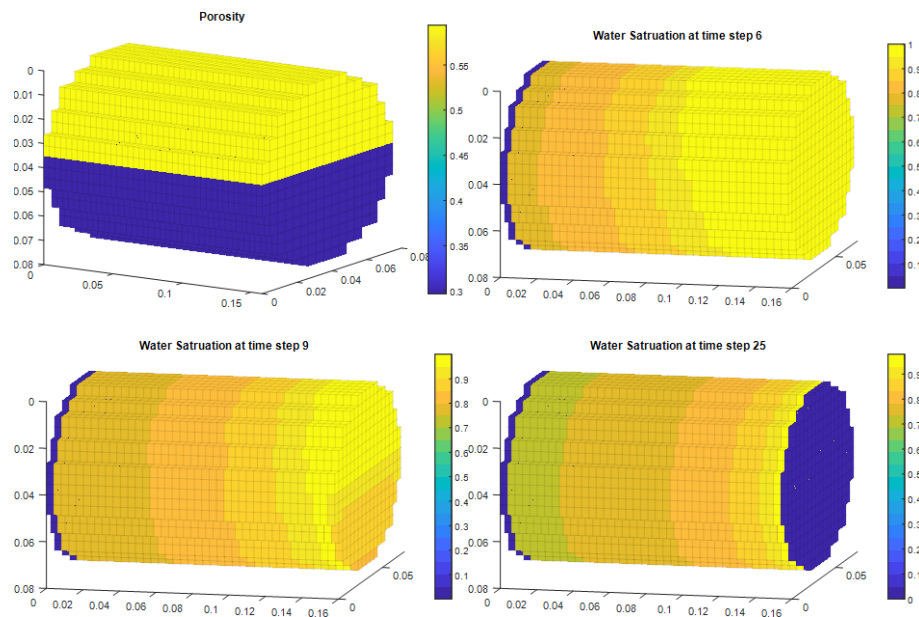
Figure 44: Permeability, Porosity and Saturation profile of the Two Layers – Double Porosity case

4. Two Layers – Double Porosity – Double Permeability: Both porosity and permeability of the top layer are amplified.
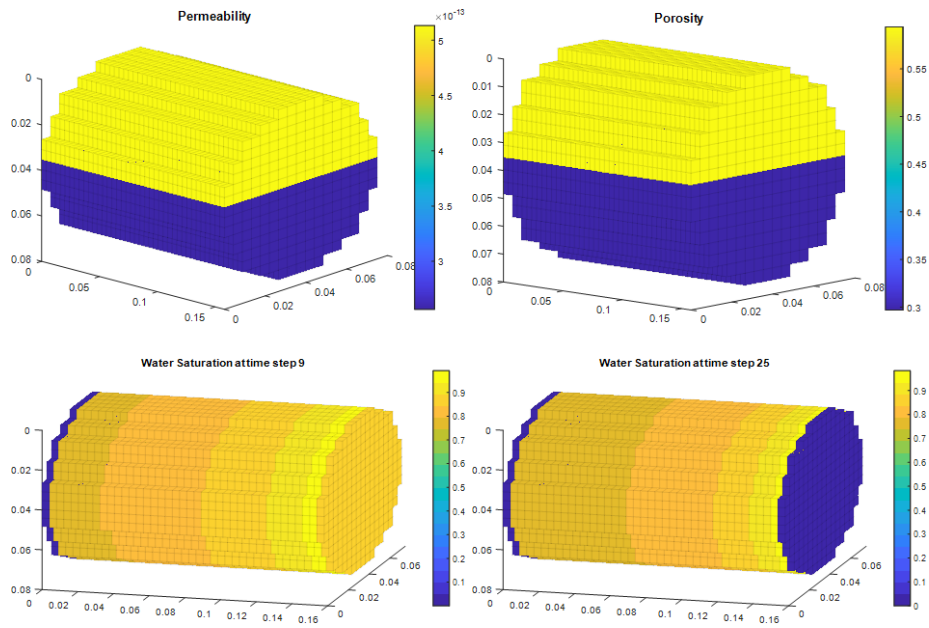
Figure 45: Permeability, Porosity and Saturation profile of the Two Layers – Double Porosity – Double Permeability case

5. Two Layers – Double Porosity – 10 times permeability: Similar to the above, with the top layer permeability enhanced tenfold.
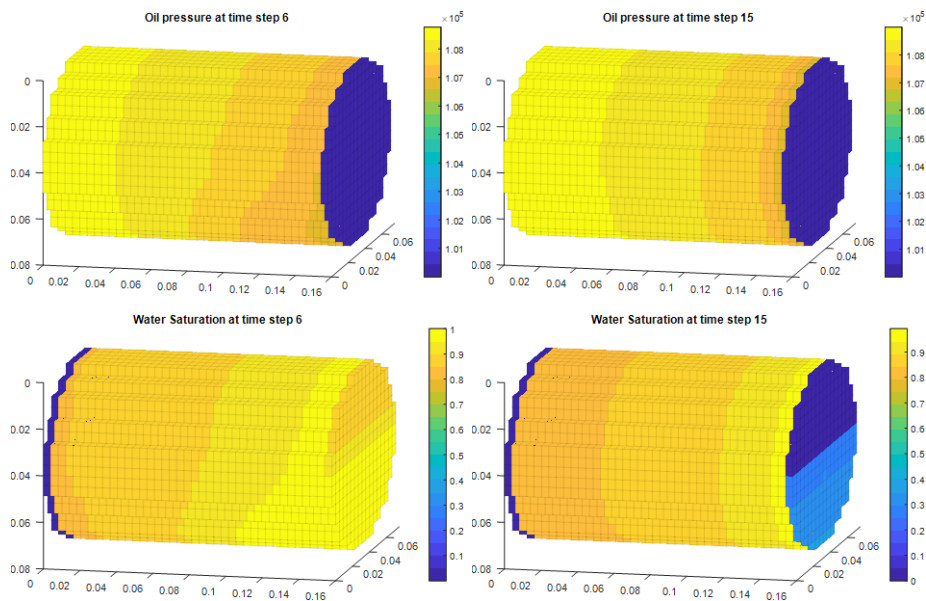
Figure 46: Permeability, Porosity and Saturation profile of the Two Layers – Double Porosity – 10 times permeability case

6. Three Layers – Variation 1: Here we assume a 3 layered system with the porosity of the top layer being double the base porosity and the porosity of the middle layer 3 times the base porosity. As in the 2 layered system, the layer with the lowest porosity has the fastest velocity.
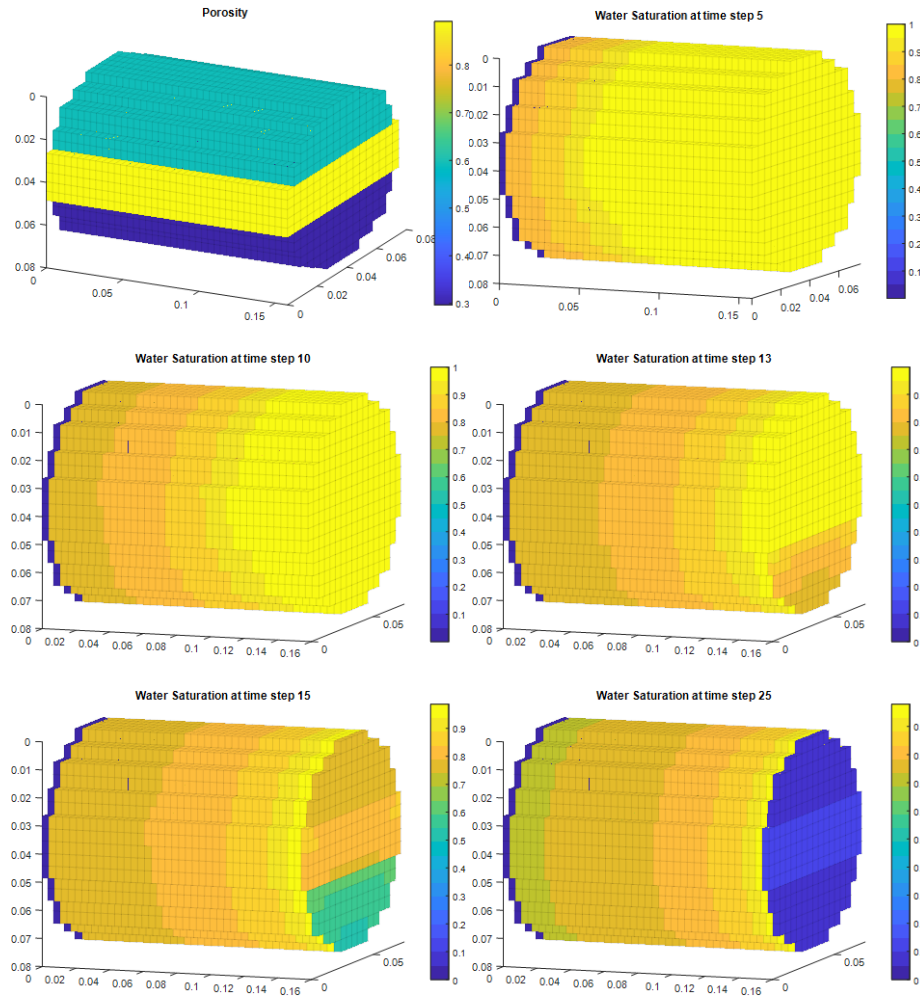
Figure 47: Permeability, Porosity and Saturation profile of the Three Layers – Variation 1 case

7. Three Layers – Variation 2: In this case we apply same multiplications to the porosity and permeability, and a piston like displacement is observed in the predictions.
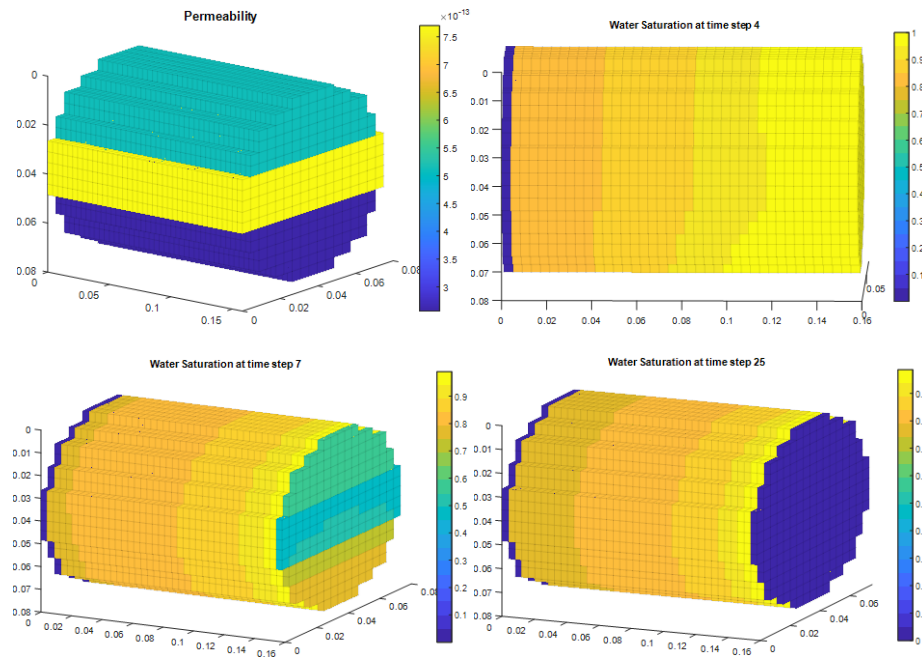
Figure 48: Permeability, Porosity and Saturation profile of the Three Layers – Variation 2 case

8. Three Layers – Variation 3: Here apply same multiplications to the porosity and permeability, and a piston like displacement is observed in the predictions.
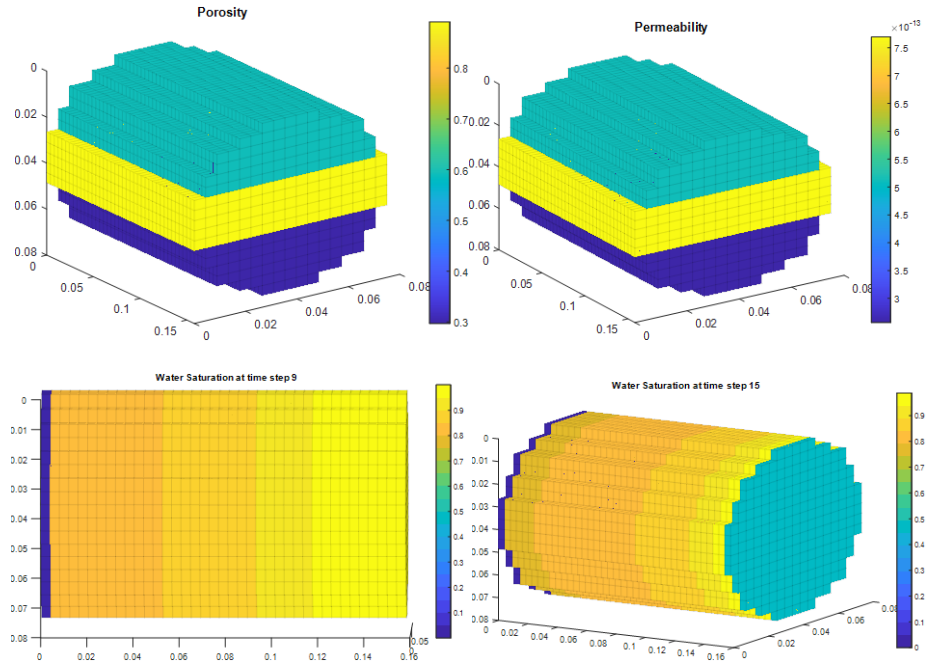
Figure 49: Permeability, Porosity and Saturation profile of the Three Layers – Variation 3 case

9. Three Layers – Capillary Scaling Factors Introduced: On top of previous scenarios, capillary scaling factors are appended, influencing shock front velocities. Here on top of the case before, capillary scaling factors are added. On the top layer we assign a factor of 1.05 to scale the capillary pressure and a factor of 1.1 to the middle layer. Note that in this scaling we divide the scaling by this factor, so a factor of 1.1 means that the capillary pressure in the corresponding layer is less than the base case (look at the Estaillades long core analysis report for the formulation). It is seen that the in the middle layer with the highest capillary scaling factor, the shock front has the highest velocity and this is coming only because of the scaling factor and not from the porosity and permeability as it was investigated in the previous cases.
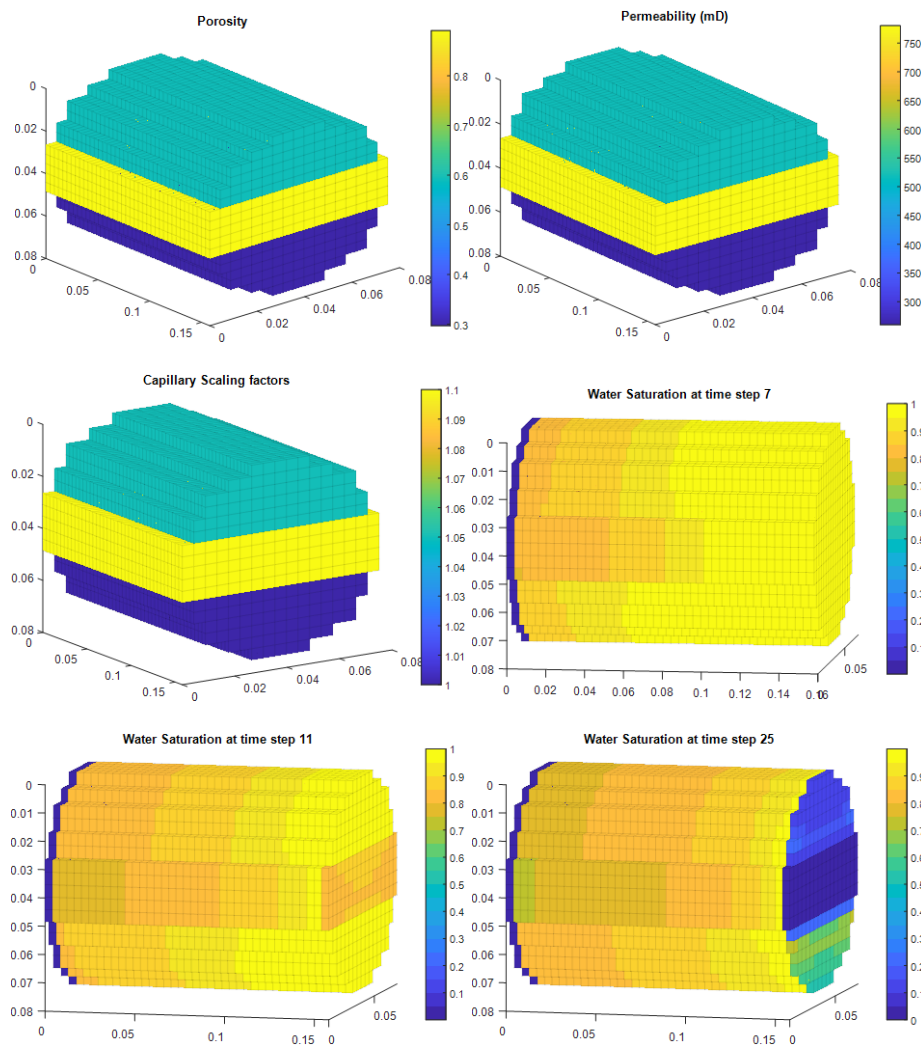
Figure 50: Permeability, Porosity and Saturation profile of the Three Layers – capillary scaling case

Appendix D

Appendix D: Code and Data Availability

The code and data used to conduct the studies presented in different chapters of this thesis are made available as open source within the links below:

1. Chapter 3: https://github.com/omidreza-amrollahi/ad-scal - The link is already public.
2. Chapter 4: https://github.com/omidreza-amrollahi/ad-scal-heterogeneous - This link is going public upon publication of the corresponding journal paper (Amrollahinasab et al., 2024a).
3. Chapter 5: https://github.com/omidreza-amrollahi/immiscible-fingerwavelength-simulation - This link is going public upon publication of the corresponding journal paper (Amrollahinasab et al., 2024b).

List of Publications

1. Amrollahinasab, O., Azizmohammadi, S., & Ott, H. (2022, September). Simultaneous Interpretation and Uncertainty Analysis of SCAL Data from Complex Rocks. Proceedings of International Symposium of the Society of Core Analysts (SCA 2022) – Austin, United States – https://jgmaas.com/SCA/2022/SCA2022-33.pdf

2. Amrollahinasab, O., Azizmohammadi, S., & Ott, H. (2023, January). Simultaneous interpretation of SCAL data with different degrees of freedom and uncertainty analysis. Computers and Geotechnics, 153, 105074. DOI: https://doi.org/10.1016/j.compgeo.2022.105074

3. Burmester, G., Jones, A., Jurcic, H., Amrollahinasab, O., Arnold, P., & Ott, H. (2023, June). Predictions of Relative Permeability and Fractional Flow on Log Scale – Pilot Projects Results. Proceedings of 84th EAGE Annual Conference & Exhibition (Vol. 2023, pp. 1-5). European Association of Geoscientists & Engineers (EAGE). DOI: https://doi.org/10.3997/2214-4609.202310097

4. Amrollahinasab, O., Jammernegg, B., Azizmohammadi, S., & Ott, H. (2023, October). Stochastic Interpretation of CO2-Brine Primary Displacement in Heterogeneous Carbonate Rocks. Proceedings of International Symposium of the Society of Core Analysts (SCA 2023) - United Arab Emirates, Abu Dhabi - https://www.jgmaas.com/SCA/2023/SCA2023-004.pdf

5. Amrollahinasab, O., Jammernegg, B., Azizmohammadi, S., & Ott, H. (2024). Stochastic Interpretation of CO2-Brine Primary Displacement in Heterogeneous Carbonate Rocks. **Submitted to Journal.**

6. Amrollahinasab, O., Ott, H., & Berg, S. (2024). The Wavelength of Viscous-Unstable Displacement in CO_2 Sequestration. **Submitted to Journal.**

Contribution of the author to the appended publications in percentage points:

Publication	Conception and Planning	Simulations	Analysis and Interpretation	Manuscript Preparation
1	75	90	90	80
2	75	90	90	80
3	20	75	20	30
4	90	100	90	80
5	90	100	90	80
6	60	100	75	75

Signature:

List of Figures

List of Tables

Nomenclature

p_C	capillary pressure	[pascal]
$k_{r\alpha}$	relative permeability of phase α	[-]
K	absolute permeability	[m^2]
ϕ	porosity	[-]
S_α	saturation of α	[-]
f_α	fractional flow of α	[-]
$\overrightarrow{v_a}$	darcy phase velocity	[$\frac{m}{s}$]
μ_α	viscosity of phase α	[pascal.second]
p_α	pressure of phase α	[pascal]
g	gravitational constant	[$\frac{m}{s^2}$]
ω	angular velocity	[$\frac{rad}{s}$]
r	distance from center of rotation - radius	[m]
d_i	experimental measured values in HM functions	[-]
y_i	calculated values from simulations in HM functions	[-]
χ^2	chi-squared function	[-]
f_j	capillary pressure scaling factors	[-]

$J(S)$	Leverett-J function	[-]
ΔP	pressure difference	[pascal]
Q	produced fluid volumes	[m^3]
σ	interfacial tension	[mN/m]
Ca	capillary number	[-]
$S_{\alpha c}$	connate (residual) saturation of phase α	[-]
n_α	Corey exponent of phase α	[-]
$K^0{}_{r\alpha}$	relative permeability of phase α at its residual saturation	[-]
λ	finger wavelength	[m]
μ_2/μ_1	viscosity ratio	[-]
D	hydrodynamic dispersion coefficient	[-]
L	length	[m]
P_{dj}	capillary entry pressures	[pascal]

Abbreviations

SCAL	Special Core Analysis
CCS	Carbon Capture and Storage
CCUS	Carbon Capture Utilization and Sequestration
MRST	MATLAB Reservoir Simulation Toolbox
SS	Steady State experiments
USS	Un-Steady State experiments
CF	Centrifuge experiments
EST	Estaillades carbonate
sc	Supercritical state
HU	Hounsfield Units
AD	Automatic Differentiation algorithm
MCMC	Markov Chain Monte Carlo algorithm
DRAM	Delayed Rejection Adaptive Metropolis algorithm
MH	Metropolis Hastings algorithm
REV	Representative Elementary Volume
IFT	Interfacial Tension
MICP	Mercury Injection Capillary Pressure
HM	History Match
MUL	Montanuniversitaet Leoben